DEPARTMENT OF PHYSICS
UNIVERSITY OF JYVÄSKYLÄ
RESEARCH REPORT No. 8/2006

SPECTROSCOPY IN THE TRANSFERMIUM REGION: PROBING ROTATIONAL, NON-YRAST AND ISOMERIC STRUCTURES IN ^{253,254}No

BY
SARAH EECKHAUDT

Academic Dissertation
for the Degree of
Doctor of Philosophy

To be presented, by permission of the
Faculty of Mathematics and Natural Sciences
of the University of Jyväskylä,
for public examination in Auditorium FYS-1 of the
University of Jyväskylä on June 19, 2006
at 12 o'clock noon

Jyväskylä, Finland
June 2006

ISBN 978-951-39-3173-5

URN:ISBN:978-951-39-3173-5

Preface

There are some special persons I would like to thank who all contributed to this work in their own unique way. The last four years would have been very different without them.

First I would like to acknowledge my supervisor Matti Leino for accepting me to work in one of the most beautifully situated laboratories in Europe and for allowing me to attend various international conferences, summerschools and experiments during this time. And I would in particular like to thank him for his concern about my general well-being in this northern place.
Then I owe a very big thank you to Paul Greenlees who was a tremendous help during this thesis. Thank you Paul for guiding me through the world of transfermium nuclei and for the many valuable suggestions and critical comments during the analysis and writing process.

Experiments are not carried out by one person alone. I would therefore like to thank the entire RITU and GAMMA group for sharing their knowledge and experience. A special 'kiitos' goes to all the Finnish students for accepting this Belgian girl in their middle.
For an inspiring atmosphere during the experiments, I would also like to thank the many foreign collaborators.

I am grateful to the referees Christelle Stodel and David Jenkins for their careful reading of the manuscript and to Marjut and Anna-Liisa for all their help with administrative matters.

Of no less importance are the people outside the work environment. Suvi I would like to thank for the nice time sharing a flat and the many evenings out, it made living in Jyväskylä a lot nicer. Also thank you Audrey, Karen, Lenka and Anniina for the enjoyable times we shared in Finland.
A heartfelt thanks goes to my friends and neighbours in Belgium for always making me feel welcome back home. 'Dankjewel' An, Anke, Caroline, Evi, Lies, Pieter, Sophie, Steven, Thomas, Valerie and Wim for proving that friendship is not stopped by borders. And 'dankjewel' mama, papa and Thomas for all your support and for being there for me all those years.
A final thanks goes to Iain for continuously inspiring me and for keeping up the positive spirits in difficult times.

Sarah

Abstract

Spectroscopic studies of the transfermium nuclei ^{254}No and ^{253}No have been carried out at the Accelerator Laboratory of the University of Jyväskylä, Finland, using the gas-filled recoil separator RITU. The use of two very efficient spectrometers, the JUROGAM germanium array at the target position and the multidetector GREAT spectrometer at the focal plane, allowed the powerful recoil-gating and recoil-isomer tagging techniques to be used.

Rotational band structures are present in both nuclei and are built upon the ground state. Evidence for the decay of non-yrast states has been observed for the first time in ^{254}No and is speculated to be due to the decay of a $K = 3$ band head. In ^{253}No a 22(4) μs isomeric state was observed at the focal plane. In addition the level scheme of the α-decay daughter ^{249}Fm could be constructed.

The results presented extend the knowledge of rotational, isomeric and non-yrast structures in transfermium nuclei and provide valuable input to nuclear structure calculations in the heavy element region.

Contents

1 Introduction

The atomic nucleus is a unique microscopic system, a quantum laboratory in which the behaviour of a limited number of strongly interacting fermions can be studied. There are less than 300 stable nuclei which occur in nature. Some 3000 additional unstable nuclei have been produced in nuclear laboratories during the last century. They are unstable against charged-particle decay or spontaneous fission. Several thousand nuclei predicted to lie between the drip lines are still waiting to be studied.
The chart of the nuclides in figure 1.1 shows the stable and unstable isotopes produced so far as a function of proton and neutron number, together with the region of nuclei whose existence is predicted.

The majority of nuclei contain sufficient numbers of nucleons so that macroscopic quantities such as shape, surface and deformation can be defined. However, the number of constituent nucleons is still small enough for a single proton or neutron to alter the behaviour of the system. In other words there is a delicate interplay of single particle and collective degrees of freedom.

Although nuclear structure studies have been carried out for several decades, the nuclear force is still largely unknown and can not be expressed in an analytical form. In the absence of a comprehensive nuclear theory, several models have been developed to describe the properties of nuclei. Some use the microscopic approach where nucleons move in a potential generated by all the nucleons, the most well known example being the shell model. Another group of models are based on the collective approach, describing the nucleus as a liquid drop-like entity.
A concise description of both approaches is given in chapter 2.

Although these models are rather successful for well-studied nuclei close to the line of stability, it is unclear how well they extrapolate to exotic regions where experimental data are scarce or non-existent. To gain further insight, experimental data for these regions are needed to provide a testing ground for various theoretical models.
One of the main regions of interest is situated at the high-mass end of the nuclear chart. Here nuclear structure research is strongly based on heavy-ion accelerators and highly sophisticated spectroscopic techniques. Beyond the last known doubly-magic nucleus ^{208}Pb, all nuclei are unstable against radioactive decay and only a few elements in this 'heavy element' region can still be found naturally.
While the 'heaviest elements' ($Z > 106$) around the next predicted doubly magic nucleus are still out of reach for detailed spectroscopic studies, technological devel-

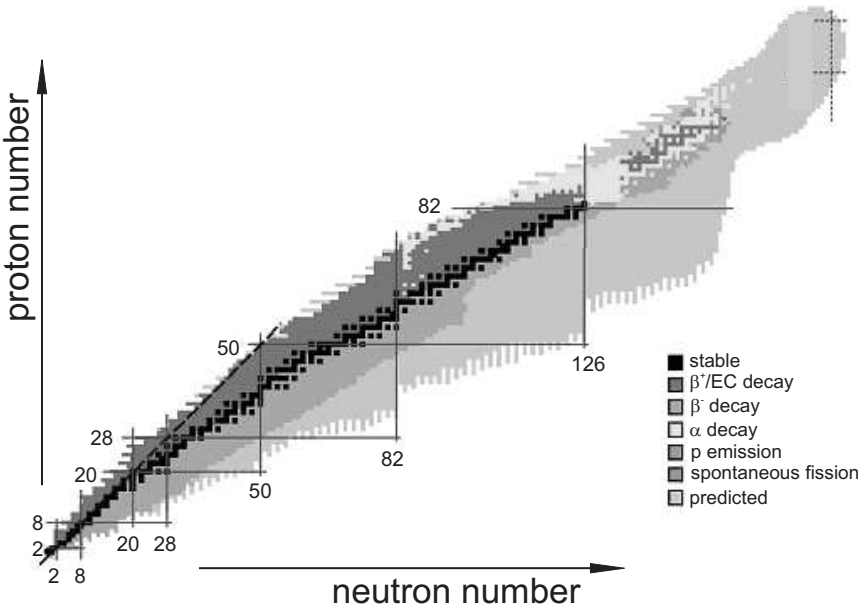

Figure 1.1: The chart of the nuclides including stable nuclei (black squares) and unstable nuclei (grey squares). The solid lines indicate the standard magic numbers.

opments and new techniques have made spectroscopic study close to the heaviest elements possible. In chapter 3 both the progress in detection and data-acquisition systems as well as new spectroscopic and analysis techniques will be discussed.

The region around ^{254}No, containing the so-called 'transfermium nuclei' ($Z = 100 - 106$, so including Fm itself in this work) produced with relatively high cross sections, are the heaviest elements which can be studied in-beam. In chapter 4 motivation for the study of the transfermium nuclei will be given as well as an overview of the previous experimental results. The two nuclei discussed thoroughly are the even-even nucleus ^{254}No and its odd-mass neighbour ^{253}No. Data of recent in-beam and decay spectroscopic studies of ^{253}No and ^{254}No, performed at Jyväskylä, will be presented, discussed and interpreted in chapters 4 and 5.

The here presented new results on ^{254}No are also published in:
S. Eeckhaudt, P.T. Greenlees, N. Amzal, J.E. Bastin, E. Bouchez, P.A. Butler, A. Chatillon, K. Eskola, J. Gerl, T. Grahn, A. Görgen, R.-D. Herzberg, F.P. Hessberger, A. Hürstel, P.J.C. Ikin, G.D. Jones, P. Jones, R. Julin, S. Juutinen, H. Kettunen, T.L. Khoo, W. Korten, P. Kuusiniemi, Y. Le Coz, M. Leino, A.-P. Leppänen, P. Nieminen, J. Pakarinen, J. Perkowski, A. Pritchard, P. Reiter, P. Rahkila, C. Scholey, Ch. Theisen, J. Uusitalo, K. Van de Vel and J. Wilson
Evidence for non-yrast states in ^{254}No
Eur. Phys. J. A **26** (2005) 227.

S. Eeckhaudt, N. Amzal, J.E. Bastin, E. Bouchez, P.A. Butler, A. Chatillon, K. Eskola, J. Gerl, T. Grahn, P.T. Greenlees, A. Görgen, R.-D. Herzberg, F.P. Hessberger, A. Hürstel, P.J.C. Ikin, G.D. Jones, P. Jones, R. Julin, S. Juutinen, H. Kettunen, T.L. Khoo, W. Korten, P. Kuusiniemi, Y. Le Coz, M. Leino, A.-P. Leppänen, P. Nieminen, J. Pakarinen, J. Perkowski, A. Pritchard, P. Reiter, P. Rahkila, C. Scholey, Ch. Theisen, J. Uusitalo, K. Van de Vel and J. Wilson
In-beam gamma-ray spectroscopy of ^{254}No
Eur. Phys. J. A **25**, Supplement 1 (2005) 605.
doi: 10.1140/epjad/i2005-06-015-3

2 Nuclear structure and decay modes

In the first part of this chapter some of the most widely used nuclear models are discussed. This overview is not meant to be exhaustive but will allow the different types of calculations mentioned in forthcoming chapters to be placed against the right background.
In the microscopic approach the nucleus is viewed as a compact collection of individual particles. The behaviour of a few valence particles is described in a central potential created by all the other nucleons.
A more intuitive picture of a nucleus as an incompressible liquid drop lies at the basis of the macroscopic approach. Therein the nucleus can be described by its surface, and all the nucleons collectively determine the rotational and vibrational movements.
Aspects of both approaches are combined in the macroscopic-microscopic model which plays an important role in the region of interest in this work, the heavy elements.
Radioactive nuclear decay can be used to study the structure of the nuclei experimentally. In the second part of this chapter properties of relevant decay modes will be addressed.
This chapter is based upon [Kra88, Cas00, Hey94, Rin04].

2.1 Microscopic approach

The microscopic approach is based on the mean-field concept with a central potential created by all the nucleons. While the spherical shell model is derived from a spherically symmetric potential, introduction of deformation to the potential well leads to a deformed shell model, the Nilsson model. The superposition of rotation is described by the cranked shell model. Those three different microscopic models together with the mean-field concept itself are briefly discussed in this section.

2.1.1 Mean-field approximation

A fully analytical description of a system of A nucleons requires the solution of the Schrödinger equation, $H\Psi(1,..,A) = E\Psi(1,...,A)$. The non-relativistic Hamiltonian

H describes the kinetic energy of the individual nucleons and the interaction between the nucleons, here assumed to be a 2-body interaction V:

$$H = \sum_{i=1}^{A} \frac{p_i^2}{2m_i} + \sum_{i=1}^{A} \sum_{k>i}^{A} V_{ik}. \tag{2.1}$$

Calculating the wave functions results in a complex many-body problem which can be solved exactly for the lightest nuclei only and an approximation is called for.
In the mean-field approximation the nucleus is viewed as a compact collection of particles whose properties are determined by the behaviour of a few valence particles moving in a central potential U created by all the other nucleons. The nucleon-nucleon interaction is replaced by an effective one-body interaction and a residual two-body interaction as a correction factor.
Equation 2.1 can then be written as the sum of a 1-body Hamiltonian H_{mf} and a residual interaction Hamiltonian H_{res}.

$$H = \sum_{i=1}^{A} (\frac{p_i^2}{2m_i} + U_i) + \sum_{i=1}^{A} \sum_{k>i}^{A} (V_{ik} - U_i) \tag{2.2}$$

$$= H_{mf} + H_{res}. \tag{2.3}$$

A proper choice of the average potential U aims to reduce the contribution of the residual interaction. Often the analytically solvable spherical harmonic oscillator potential is used. In order to reproduce the well established shell structure in nuclei, Mayer [May49] and Haxel, Jensen and Suess [Hax49] added an extra spin-orbit term $\sim \mathbf{l} \cdot \mathbf{s}$ representing the coupling between the spin s and orbital angular momentum l. Furthermore an extra $\mathbf{l^2}$ term was included to account for the screening of nucleons at the center of the nucleus from the asymmetric distribution at the boundary. Adding those terms to the spherical harmonic oscillator potential reproduces the correct magic numbers as shown in figure 2.1.
The harmonic oscillator, albeit simple, is not the most realistic central potential. A number of potential wells which are often used are depicted in figure 2.2.

The determination of a more realistic average potential can be approached as a variational problem. The single-particle potential U can be derived in a self-consistent way from effective 2-body nucleon-nucleon interactions such as Skyrme (δ-type) and Gogny forces (finite range) using the Hartree-Fock variational method (HF). There are several parametrisations available for the effective nucleon-nucleon interaction coming from different fits to known experimental data. If pairing correlations have to be taken into account, the Hartree-Fock-Bogoliubov method (HFB) is used.

Relativistic mean-field theory treats the nucleons as relativistic Dirac particles. The nucleons are the source of meson clouds which create the mean field they move in.

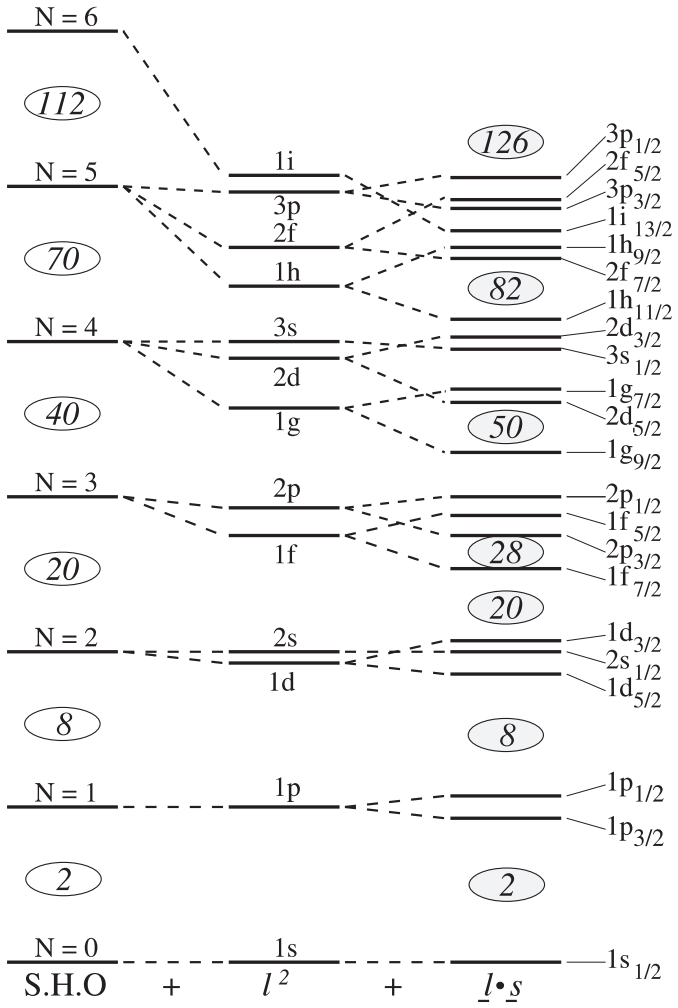

Figure 2.1: Single-particle states for a simple harmonic oscillator potential (SHO) in the mean-field approximation, with the effect of the $\mathbf{l^2}$ term and finally a more realistic shell model potential with both $\mathbf{l^2}$ and spin-orbit $\mathbf{l}\cdot\mathbf{s}$ correction terms, with the standard magic numbers indicated. N labels the oscillator shells while the final shell model states are labeled nl_j where the orbital angular momentum $l = 0, 1, 2, 3, ...$ is denoted with the conventional $s, p, d, f, ...$ notation, n counts the states of same l value and $j = l + s = l \pm \frac{1}{2}$ where s is the spin angular momentum. [Pau00]

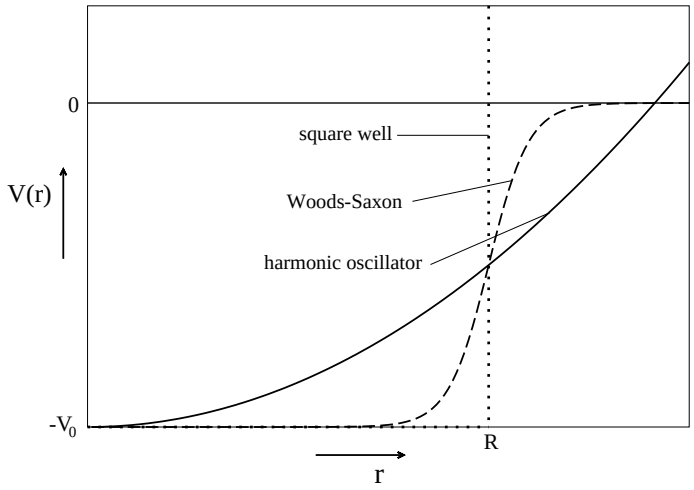

Figure 2.2: The shape of different potential wells.

2.1.2 Spherical shell model

In the independent particle model, the detailed interactions between nucleons are ignored and each particle moves in a state independent of the other particles. The mean-field force is an average smoothed-out interaction with all the other particles. The independent particle model with a spherical potential explains properties of nuclei with one valence particle outside an inert core very well. When more valence nucleons have to be taken into account, the residual interactions (equation 2.3) between the valence particles start to play a role. In the spherical shell model, in addition to the mean field, those residual interactions are taken into account.
In principle, one would need to diagonalise the full Hamiltonian H of equation 2.3. However, for nucleons of the same type, the residual interaction is dominated by the attractive pairing force. Pairing introduces the coupling of two nucleons to spin and parity $I^\pi = 0^+$ and scatters those pairs into different orbitals with a smearing of the Fermi surface as a consequence as illustrated in figure 2.3. Considering the pairs as an inert core, one can reduce the model space to a few valence particles outside the inert core.
A convenient way to treat pairing is the introduction of a new concept: quasi-particles. They are linear combinations of particle and hole wave functions. The single-particle energy ϵ_i becomes a quasi-particle energy e'_i:

$$e'_i = \sqrt{(\epsilon_i - \lambda)^2 + \Delta^2} \tag{2.4}$$

with λ the Fermi energy and Δ the pairing-gap parameter. An obvious manifestation of the pairing interaction is the $I^+ = 0^+$ ground state in all even-even nuclei. In odd-mass nuclei, the state occupied by the odd nucleon can not be used in the scattering of the quasi-particles across the Fermi-gap, giving rise to the so called 'blocking' effect.

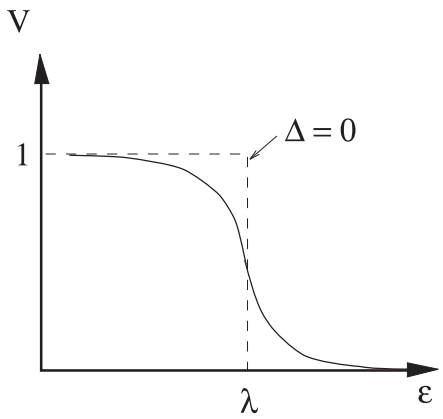

Figure 2.3: The smearing effect of pairing on the Fermi surface. λ is the single-particle energy at the Fermi surface and V indicates the occupation probability of a certain orbital. [Pau00]

In case both valence protons and neutrons are present, the attractive proton-neutron interaction plays a crucial role. This interaction is responsible for the development of deformation with an increasing number of valence nucleons.

2.1.3 Deformed mean field: the Nilsson model

When the number of valence nuclei becomes too large, spherical shell model calculations become complicated and a transition from a spherical to a deformed mean field can be made. The Nilsson model is a single-particle model applicable to nearly all deformed nuclei.

For a deformed axially symmetric nucleus with symmetry axis z (i.e. $x = y \neq z$) the mean-field potential is no longer isotropic, and the single particle Hamiltonian can be written as:

$$H = \frac{\mathbf{p^2}}{2m} + \frac{m(\omega_x^2(x^2+y^2)+\omega_z^2 z^2)}{2} + 2\hbar\omega_0\kappa\mathbf{l}\cdot\mathbf{s} + \mu\kappa\hbar\omega_0\mathbf{l^2}. \tag{2.5}$$

The second term represents the mean field anisotropic harmonic oscillator with $\omega_x^2 = \omega_y^2 = \omega_0^2(1+\frac{2}{3}\epsilon_2)$ and $\omega_z^2 = \omega_0^2(1-\frac{4}{3}\epsilon_2)$ where ϵ_2 is the deformation parameter introduced by Nilsson and is related to the quadrupole deformation parameter $\beta_2 \approx 1.05\epsilon_2$ and ω_0 is the oscillator frequency in a spherical potential. The strength of the $\mathbf{l}\cdot\mathbf{s}$ and $\mathbf{l}^2$ terms is parametrised by κ and μ.

The Nilsson states are typically labeled as follows:

$$\Omega^\pi[Nn_z\Lambda] \tag{2.6}$$

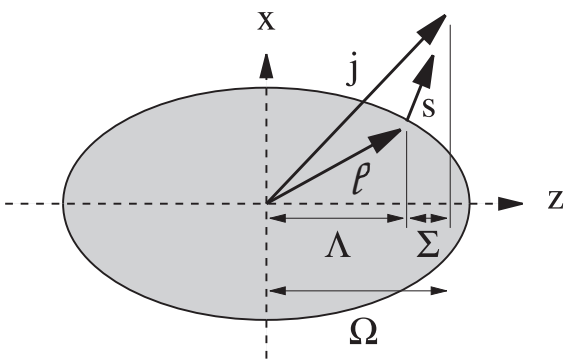

Figure 2.4: Illustration of the quantum numbers used in the Nilsson model. [Pau00]

where the first quantum number, $\Omega = \Sigma + \Lambda$, gives the projection of the total single-particle angular momentum (sum of the spin Σ and orbital Λ angular momentum projection) onto the symmetry axis. The parity is π, N is the principal quantum number of the major shell (see figure 2.1) and n_z the number of nodes in the wave function along the z axis. Some of the quantum numbers used in the Nilsson model are depicted in figure 2.4. For axially symmetric nuclei, K, the projection of the total angular momentum onto the symmetry axis, is often substituted for Ω.

The single-particle states emerging after solving the Hamiltonian in equation 2.5 for the regions $Z \geq 82$ and $N \geq 126$ are depicted in figure 2.5 and 2.6 respectively where single-particle energy is plotted as a function of the deformation parameter ϵ_2 [Fir96]. Each state can hold two nucleons due to the $\pm\Omega$ degeneracy. The ground state and excited states of the deformed nucleus can be easily read off the Nilsson diagrams.

2.1.4 Cranked shell model

In order to describe collective rotation around an axis (x) perpendicular to the symmetry axis (z), the cranked shell model is used. In this model the mean-field concept is extended to include rotation. The dynamical coupling between the single quasi-particle states and the nuclear rotation can be described by the cranking Hamiltonian or Routhian:

$$H^{\omega} = H_{int} - \hbar\omega I_x \tag{2.7}$$

$$\text{with } I_x = (I(I+1) - K^2)^{1/2} \tag{2.8}$$

where H_{int} is the intrinsic single-particle Hamiltonian, ω the rotational frequency and I_x the projection of the total angular momentum onto the rotational x-axis (also called aligned angular momentum). The term $\hbar\omega I_x$ includes the centrifugal and Coriolis forces. The single-particle Hamiltonian can be based on different shapes of the

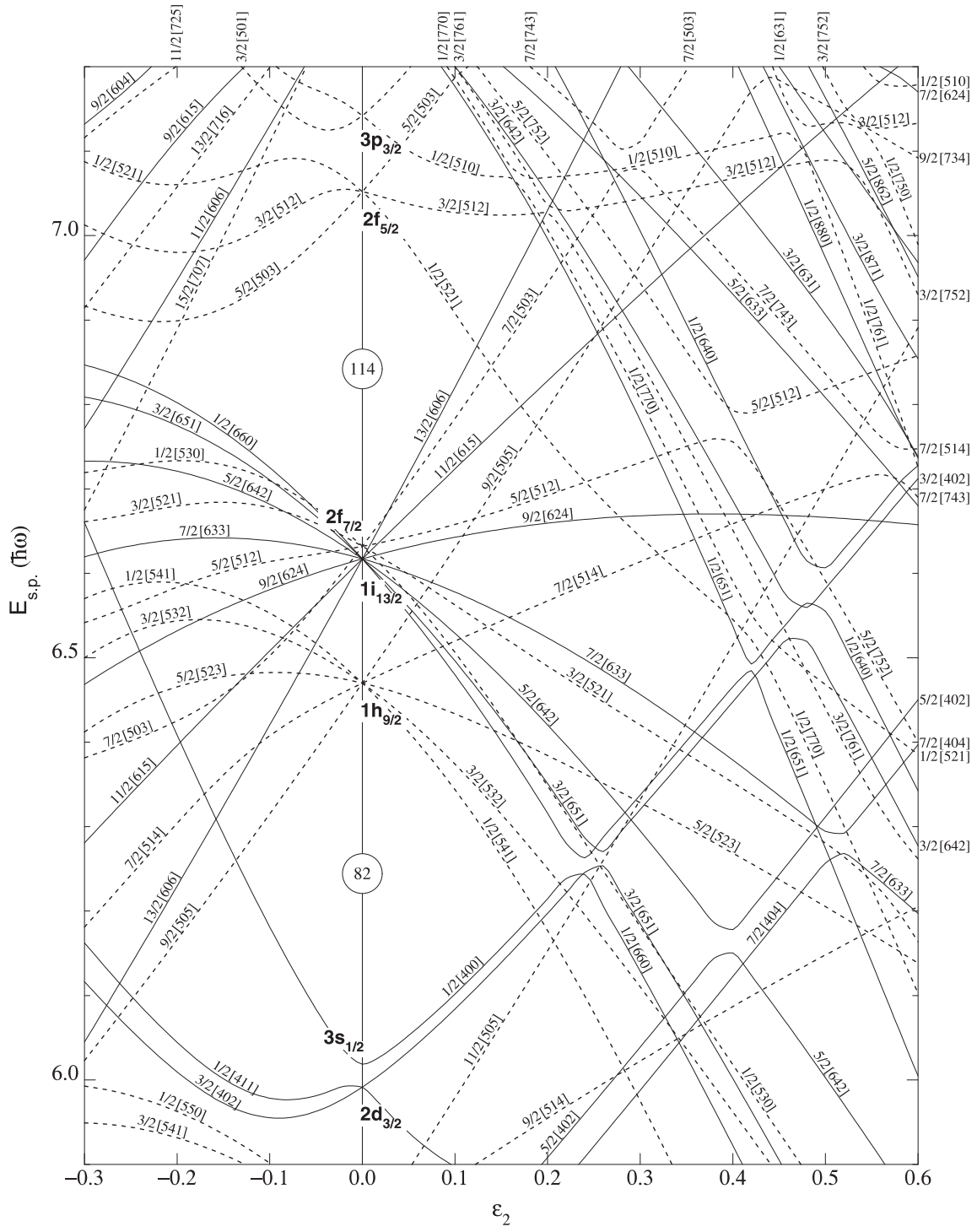

Figure 2.5: The Nilsson states for proton number $Z \geq 82$.

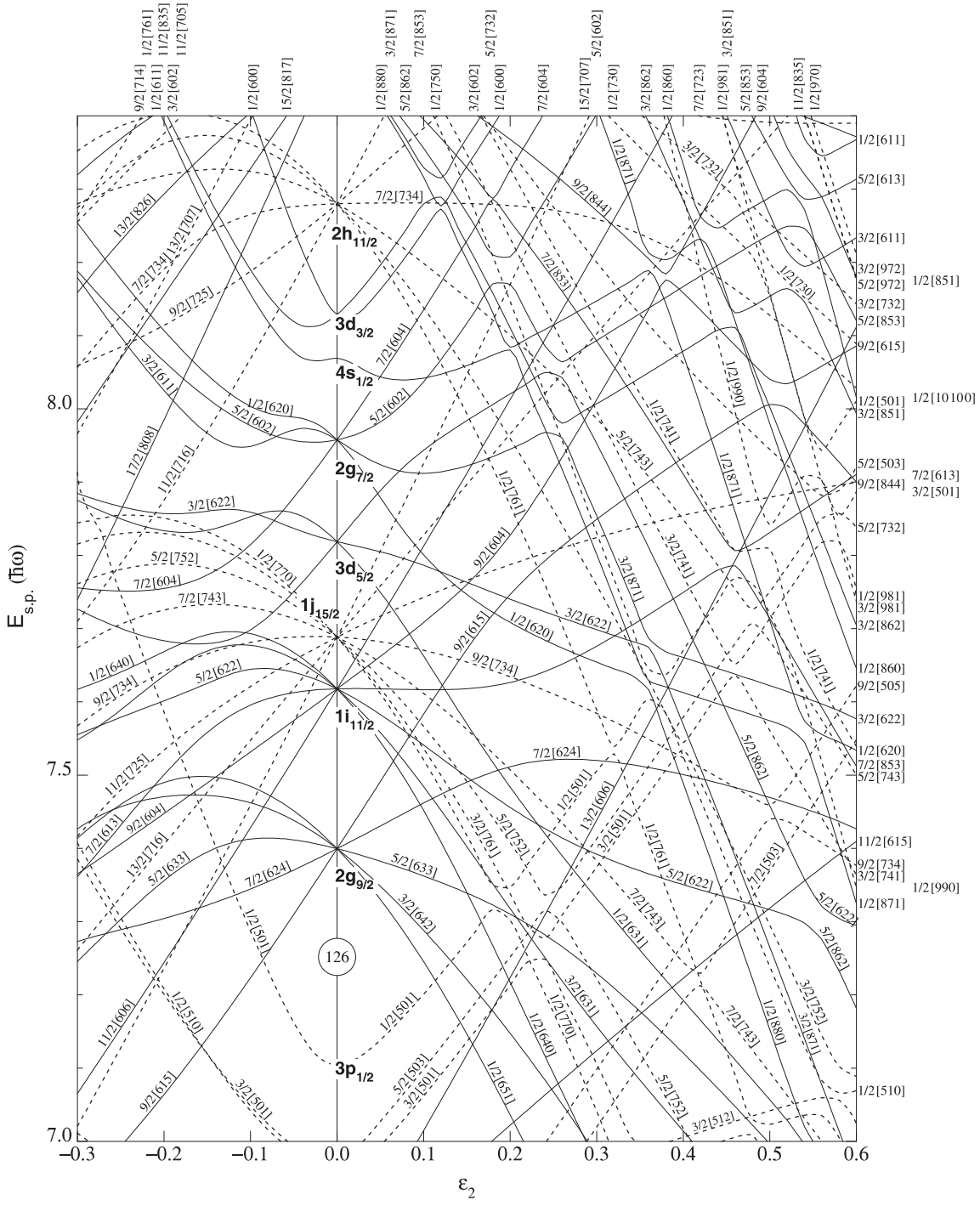

Figure 2.6: The Nilsson states for neutron number $N \geq 126$.

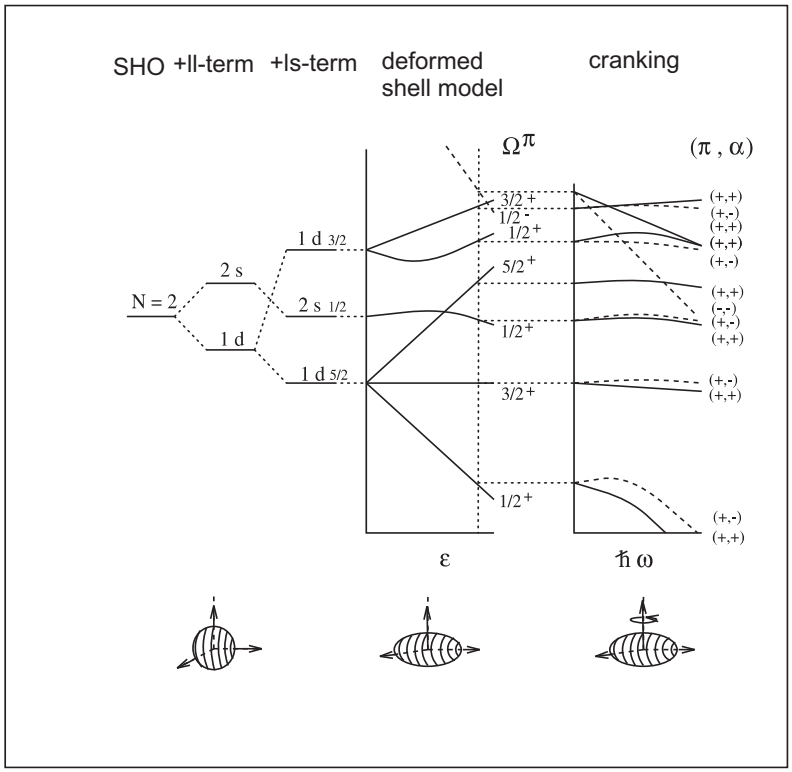

Figure 2.7: The evolution of the single-particle energies in the different microscopic approaches. [Pau00]

potential, as discussed in section 2.1.1.
Due to the addition of the cranking term $\hbar\omega I_x$ to the single-particle Hamiltonian, symmetries are broken. However, rotating twice by π around the x-axis leaves the wave function unchanged for even-mass nuclei and changes the sign for odd-mass nuclei:

$$R_x^2(\pi)\Psi \quad = \quad r^2\Psi = (-1)^A\Psi \tag{2.9}$$

with eigenvalues $r = \pm 1$ for even-mass and $r = \pm i$ for odd-mass nuclei. For convenience, the signature quantum number α is defined as $r = e^{-i\pi\alpha}$. The spin[1] sequences are restricted to $I = \alpha mod 2$. Parity is the only other remaining conserved quantum number and hence Routhians are often labeled with signature α and parity π.

As a summary of this chapter, the evolution from the spherical harmonic oscillator single-particle states via the deformed shell model to the cranked shell model solutions is shown for the $N = 2$ major shell in figure 2.7.

[1] In nuclear spectroscopy, the total angular momentum I is often called 'spin'.

2.2 Macroscopic approach

In the liquid-drop model, the nucleus is seen as an incompressible sphere of nucleons resembling a drop of liquid. While this simple model gives reasonable estimates for bulk properties of the nucleus, it does not take into account quantal behaviour. The more advanced collective model, largely developed by Bohr and Mottelson [Boh75], is based on the concept of a non-spherical shaped nucleus which can undergo macroscopic motions and excitations.
This section gives an overview of vibrational and rotational characteristics of collectively behaving deformed nuclei. Emphasis is put on the rotational motion as this will be of major importance for the analysis performed in this work.

2.2.1 Deformation

When moving far away from the magic shell closures, nuclei can have stable deformation in their ground state. The most common non-spherical shape is a quadrupole shape ($\lambda = 2$) but also octupole ($\lambda = 3$) shapes are observed.
In a laboratory-fixed frame the radius can be expressed as:

$$R(\theta,\phi) \;=\; R_0\left(1+\sum_{\lambda=0}^{\lambda_{max}}\sum_{\mu=-\lambda}^{\lambda}\alpha_{\lambda\mu}Y_{\lambda\mu}(\theta,\phi)\right) \tag{2.10}$$

where R_0 represents the radius of a spherical nucleus with the same volume, $Y_{\lambda\mu}$ are spherical harmonics and $\alpha_{\lambda\mu}$ expansion coefficients. In case of quadrupole deformation, the $\alpha_{\lambda\mu}$ coefficients can be rewritten in the body-fixed frame as $\alpha_{2,0} = \beta_2 cos\gamma$ and $\alpha_{2,2} = \alpha_{2,-2} = \beta_2 sin\gamma$ which introduces the quadrupole deformation parameter β_2 and the parameter γ indicating the deviation from axial symmetry. The rest of the discussion will be restricted to the case of axially symmetric nuclei (i.e. $\gamma = 0$) with a quadrupole deformed ground state. In that case $\beta_2 > 0$ gives prolate (rugby ball like) deformed shapes while $\beta_2 < 0$ stands for oblate (disk like) deformation.

2.2.2 Vibration and rotation

The collective motion of nucleons in an axially deformed nucleus can be classified as vibrational or rotational motion.

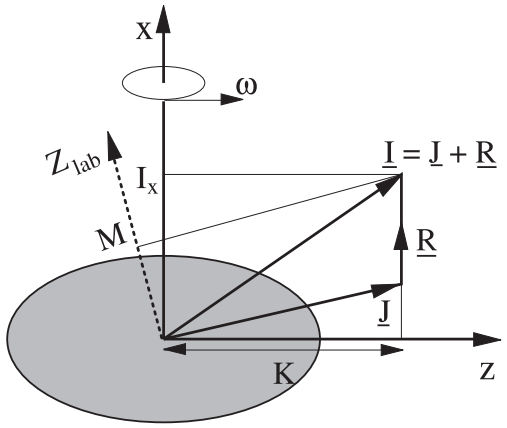

Figure 2.8: Illustration of the rotational quantum numbers. [Pau00]

Vibration

The collective vibrations of a nucleus around its equilibrium shape give rise to a set of low-lying states in deformed nuclei. They can be included in equation 2.10 by making the $\alpha_{\lambda\mu}$ expansion coefficients time dependent.
The lowest mode of vibration is a $\lambda = 2$ quadrupole vibration which can take two forms: β-vibrations ($K^\pi = 0^+$) are shape oscillations along the symmetry axis while γ-vibrations ($K^\pi = 2^+$) give rise to temporal deviations from axial symmetry. The lowest-lying negative-parity excitations are octupole vibrations ($\lambda = 3$) which can have $K^\pi = 0^-, 1^-, 2^-$ or 3^-.

Rotation

A deformed nucleus is an object with spatial orientation and inevitably has rotational degrees of freedom. Rotations can be superimposed on the ground state as well as on intrinsic vibrational or quasi-particle excitations, giving rise to rotational bands built on top of those states.
A state is characterised by the total angular momentum (i.e. spin) **I**=**R**+**J** (where **R** is the angular momentum generated by the rotation of the core and **J** is the sum of the intrinsic angular momenta j of the nucleons, see figure 2.8) and its projection onto the symmetry axis K.

The total excitation energy of each state is a sum of a single-particle contribution and

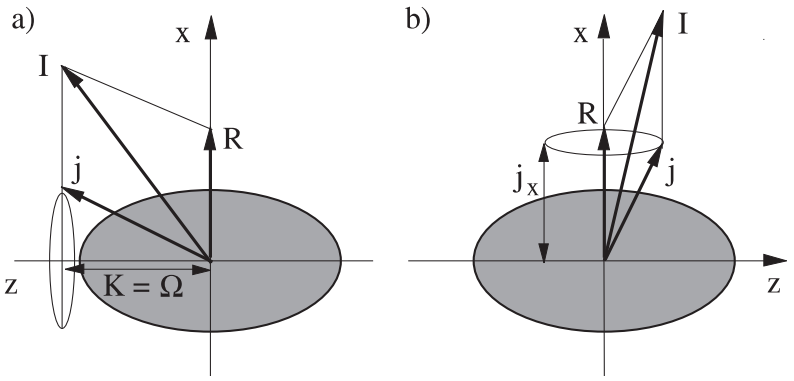

Figure 2.9: Schematic representation of the a) deformation aligned and b) rotation aligned coupling schemes. [Pau00]

the rotational energy E_{rot} derived from the rotational Hamiltonian:

$$\mathbf{H_{rot}} = \frac{\hbar^2}{2\mathcal{J}^{(0)}}\mathbf{R^2} \tag{2.11}$$

$$= \frac{\hbar^2}{2\mathcal{J}^{(0)}}(\mathbf{I^2} + \mathbf{J^2} - \mathbf{2I \cdot J}) \tag{2.12}$$

where the term $\mathbf{I} \cdot \mathbf{J}$ represents the coupling of the degrees of freedom of the valence particle to the rotation, analogous to the classical Coriolis force. $\mathcal{J}^{(0)}$ represents the intrinsic moment of inertia and will be discussed further in this section.

Two extreme cases of the coupling of the valence particle to the core can be defined. In the strong coupling limit, valid when the deformation is large and/or the K value is high, the odd particle couples to the deformed core as shown figure 2.9a. This case is called deformation aligned and $\mathbf{j}$ precesses freely around the symmetry axis. $\mathbf{K}$ is a good quantum number and states with spin $I = K, K+1, K+2, \ldots$ are observed (unless $K = 0$ in which case only even spin values are allowed) with energies given by:

$$E^K_{rot}(I) = \frac{\hbar^2}{2\mathcal{J}^{(0)}}(I(I+1) - K^2). \tag{2.13}$$

For $K = 0$ a single rotational band with $\Delta I = 2$ is seen while for integer $K \neq 0$ two signature partner bands with $\alpha = 0, 1$ and $\Delta I = 2$ transitions with interlinking $\Delta I = 1$ transitions are observed. For half integer K values the two signature partner bands have signature $\alpha = \pm 1/2$.
If the odd particle sits in an orbital with a large j and low Ω, the Coriolis force starts to act, introducing some perturbation to the rotational properties described by equation 2.13, giving instead:

$$E^K_{rot}(I) = \frac{\hbar^2}{2\mathcal{J}^{(0)}}((I - i_0)(I - i_0 + 1) - K^2) \tag{2.14}$$

with i_0 the alignment [Wu92].

In the case of weakly-deformed nuclei or fast rotation the Coriolis coupling may be strong enough to break the coupling between the nucleon and the deformed core, aligning **j** with the rotational axis instead (figure 2.9b).

Equation 2.13 is a simple first order expression and a first possible improvement is the addition of a higher order term in I to better fit the variation in the moment of inertia:

$$E^K_{rot}(I) = A(I(I+1) - K^2) + B(I(I+1) - K^2)^2. \quad (2.15)$$

An alternative approach to improve equation 2.13 was proposed by Harris and expands the energy of the rotational states in terms of the angular velocity ω:

$$E(\omega) = \omega^2(A + B\omega^2 + ...). \quad (2.16)$$

This expansion gives very good results, even with just a two-parameter approximation, to which Harris usually restricted himself.
This method is equivalent to the Variable Moment of Inertia (VMI) model which recognises the frequency dependence of the moment of inertia $\mathcal{J}^{(0)}$.
To show changes in the moment of inertia of equation 2.13, the kinematic moment of inertia ($\mathcal{J}^{(1)}$) and the dynamical moment of inertia ($\mathcal{J}^{(2)}$) are defined in general as:

$$\mathcal{J}^{(1)} = I_x(\tfrac{dE(I)}{dI_x})^{-1}\hbar^2 = \hbar\frac{I_x}{\omega} \quad (2.17)$$

$$\mathcal{J}^{(2)} = (\tfrac{d^2E(I)}{dI_x^2})^{-1}\hbar^2 = \hbar\frac{dI_x}{d\omega} \quad (2.18)$$

where $I_x = \sqrt{I(I+1) - K^2}$ is the aligned angular momentum and the angular frequency ω can be derived from:

$$\hbar\omega = \frac{dE(I)}{dI_x}. \quad (2.19)$$

For a rigid rotor, $\mathcal{J}^{(1)}$ is constant as a function of ω.

For a $\Delta I = 2$, $K = 0$ band these quantities become more transparent and can be directly related to experimental observables. The kinematic moment of inertia can be written as:

$$\mathcal{J}^{(1)}(\omega_2) = \frac{\hbar^2(2I-1)}{E_{\gamma_2}} \quad (2.20)$$

where spin I and E_{γ_2} are defined in figure 2.10 and the rotational frequency can be approximated by $\omega_2 \approx E_{\gamma_2}/2\hbar$.

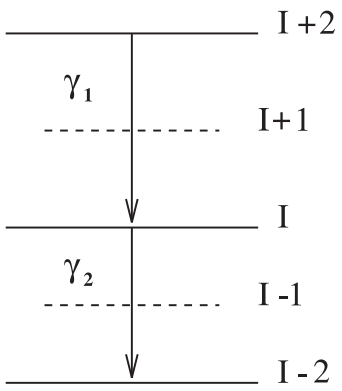

Figure 2.10: Level scheme defining the notations used for spins and transition energies.

The Variable Moment of Inertia model assumes in first order that:

$$\mathcal{J}^{(1)} = \mathcal{J}_0 + \mathcal{J}_1\omega^2 \quad \text{or} \quad \mathcal{J}^{(2)} = \mathcal{J}_0 + 3\mathcal{J}_1\omega^2 \tag{2.21}$$

where $\mathcal{J}_0$ and $\mathcal{J}_1$ are known as the Harris parameters. The VMI method can also be used to find the correct spin assignment for a $K = 0$ rotational band. When the correct spin assumption is made, the Harris parameters can be used to extrapolate the energies of unknown transitions using:

$$I(\omega) = \omega(\mathcal{J}_0 + \mathcal{J}_1\omega^2) + \frac{1}{2}. \tag{2.22}$$

Another experimentally useful quantity is the dynamical moment of inertia

$$\mathcal{J}^{(2)}(\omega_{level}) \quad = \quad \frac{4\hbar^2}{E_{\gamma_1} - E_{\gamma_2}} \tag{2.23}$$

where $\omega_{level} = (E_{\gamma_1} + E_{\gamma_2})/4\hbar$. The dynamical moment of inertia $\mathcal{J}^{(2)}$ is independent of the spin assignment and can be determined based on the experimentally observed γ-ray transition energies.
The term $E_{\gamma_1} - E_{\gamma_2}$ should be constant along a rotational band so when the dynamical moment of inertia $\mathcal{J}^{(2)}$ is plotted against rotational frequency ω, non-linearity is a sign of deviations from an ideal rotor.
As the nucleus rotates, it experiences a centrifugal force that tends to increase the deformation and decrease the rotational spacings. The plot of $\mathcal{J}^{(2)}$ against ω therefore gradually increases, exhibiting slight non-linearity. At some point the rotational energy exceeds the energy to break a pair of nucleons which then align along the axis of rotation. The moment of inertia increases along with a decrease of rotational frequency and a more radical behaviour in the plot known as backbending can be observed after which the gradual increase takes place again until the next pair breaks. Upbending will be observed instead of backbending when the interaction strength is small.

2.3 Macroscopic-microscopic model

The macroscopic-microscopic models are based on the assumption that the total energy of a nucleus can be decomposed in two parts:

$$E = E_{macro} + E_{micro} \tag{2.24}$$

where E_{macro} is the macroscopic energy and E_{micro} represents the shell plus pairing correction.

For the calculation of the macroscopic energy different models can be used, the most common one being the liquid drop model. Over the years extensions to this model have resulted in the finite-range liquid drop model and the droplet model (for an overview see [Mol94]).
To calculate the microscopic part various deformed single-particle potentials can be used such as the deformed Woods-Saxon potential.

Strutinsky shell correction method

Strutinsky developed an algorithm to superimpose the shell strength as a correction to the liquid-drop model energy.
He defines in [Str67] a shell in general as a gap within the inhomogeneous distribution of the single-particle states. From this definition, shells may be expected for any nuclear shape. The non-uniformity in the level spacing creates the required shell-correction energy to an appropriately chosen average, the liquid-drop energy. The total energy can then be written as:

$$E = E_{macro} + E_{sh} \tag{2.25}$$

$$= E_{macro} + \sum_i \epsilon_i - \overline{E}_{SHELL} \tag{2.26}$$

where the sum of individual single-particle energies are subtracted by a smoothed shell energy to obtain the quantum mechanical corrections to the macroscopic model. The ground-state shape is determined by the balance of the shell-correction energy favouring different shapes as function of proton and neutron number and the liquid-drop part, favouring spherical shapes.

This is an extremely successful macroscopic-microscopic method that forms the basis of understanding the relative stability of nuclei with proton number $Z \gtrsim 100$.

2.4 Nuclear decay modes

Radioactive nuclear decay can be used as a probe to reveal nuclear structure information. In this work γ-ray emission was studied at the target and the focal plane of RITU, revealing properties of the excited states. Additionally conversion electrons and α particles were detected at the focal plane in order to characterise ground- and excited states of the implanted nuclei.
Some properties of those decay modes are discussed here.

2.4.1 Electromagnetic decay

When a nucleus decays internally via the electromagnetic interaction from an initial excited state of spin I_i to a final state of spin I_f, a photon of γ radiation with energy $E_\gamma = E_i - E_f$, angular momentum L and parity π_γ can be emitted. This will either be an electric (E) or magnetic (M) transition, depending on the angular momentum and parity selection rules:

$$|I_i - I_f| \leq \quad L \quad \leq |I_i + I_f| \quad (L \neq 0) \tag{2.27}$$

$$\pi_i \pi_\gamma \pi_f \quad = \quad 1 \tag{2.28}$$

$$\text{with } \pi_\gamma^{(EL)} = (-1)^L \quad \text{and} \quad \pi_\gamma^{(ML)} = (-1)^{L+1}$$

where L is known as the multipolarity of the transition. Electromagnetic transitions are not always pure and often a mixture of different multipolarities exists.

The total γ-ray transition probability $T_\gamma^{fi}(\hat{O}_L)$, i.e. the decay rate from an initial state i to a final state f via a transition with multipolarity L and energy E_γ, is expressed as:

$$T_\gamma^{fi}(\hat{O}_L) \quad = \quad \frac{8\pi(L+1)}{\hbar L((2L+1)!!)^2}\left(\frac{E_\gamma}{\hbar c}\right)^{2L+1} B(\hat{O}_L : I_i \rightarrow I_f)[1/s] \tag{2.29}$$

where $B(\hat{O}_L : I_i \rightarrow I_f)$ is the reduced γ-ray transition probability, discussed below.

Theoretical total γ-ray transition probabilities were estimated by Weisskopf for single-particle transitions and by Bohr and Mottelson for collective transitions [Boh75]. These values serve as a comparison for experimentally observed transition probabilities if corrected appropriately for internal conversion. Expressions for the lowest multipolarities are given in table 2.1. The transition probability decreases with increasing multipolarity and for a certain multipolarity, L, electric transitions dominate over magnetic transitions.
The partial γ-ray decay half-life $t_{1/2}^\gamma$ is inversely proportional to the transition rate

T_γ^{fi} and can be calculated as:

$$T_\gamma^{fi}(\hat{O}_L) = \frac{ln2}{t_{1/2}^\gamma} = \lambda_\gamma \tag{2.30}$$

where λ_γ stands for the partial γ-ray decay constant.

Table 2.1: Estimated γ-ray transition probabilities for single-particle (Weisskopf estimates) and collective transitions. Transition probabilities T_γ in s^{-1}, transition energies E_γ in MeV, $B(EL)$ in e^2fm^{2L} and $B(ML)$ in $\mu_N^2 fm^{2L-2}$.

	Weisskopf	Collective
T_γ(E1)	$1.0 \times 10^{14} A^{\frac{2}{3}} E_\gamma^3$	$1.59 \times 10^{15} B(E1) E_\gamma^3$
T_γ(M1)	$5.6 \times 10^{13} E_\gamma^3$	$1.76 \times 10^{13} B(M1) E_\gamma^3$
T_γ(E2)	$7.3 \times 10^{7} A^{\frac{4}{3}} E_\gamma^5$	$1.23 \times 10^{9} B(E2) E_\gamma^5$
T_γ(M2)	$3.5 \times 10^{7} A^{\frac{2}{3}} E_\gamma^5$	$1.36 \times 10^{7} B(M2) E_\gamma^5$
T_γ(E3)	$3.4 \times 10^{1} A^{2} E_\gamma^7$	$5.71 \times 10^{2} B(E3) E_\gamma^7$
T_γ(M3)	$1.6 \times 10^{1} A^{\frac{4}{3}} E_\gamma^7$	$6.31 \times 10^{0} B(M3) E_\gamma^7$

The reduced transition probability $B(\hat{O}_L : I_i \rightarrow I_f)$ can be used to compare the strength of transitions over the entire nuclear chart, independent of the transition energy. In the case of collective $M1$ or $E2$ transitions, the reduced γ-ray transition probability can be expressed (for $K \neq 1/2$) as:

$$B(M1 : I_i \rightarrow I_f) = \frac{3}{4\pi}(g_K - g_R)^2 K^2 | < I_i K 10 | I_f K > |^2 \ [\mu_N^2] \tag{2.31}$$

$$B(E2 : I_i \rightarrow I_f) = \frac{5}{16\pi} Q_0^2 | < I_i K 20 | I_f K > |^2 \ [(eb)^2] \tag{2.32}$$

where Q_0 is the intrinsic quadrupole moment. The rotational gyromagnetic ratio (g-factor) g_R coming from the contribution of a rotating core to the magnetic moment of the nucleus, can be approximated as $g_R \approx Z/A$. In the case $K \neq 0$, the contribution of the valence particle(s) can be described by an additional g-factor g_K, characteristic of a certain configuration.

Frequently structural information can be deduced from the reduced transition rates. In the case of transitions of multipolarity L originating from the same initial state $I_i K_i$ and decaying into different final states $I_{f1} K_f$ and $I_{f2} K_f$ of the same band, the Alaga rules are valid [Ala55]. They rely on the fact that the intrinsic structure of the states $I_{f1} K_f$ and $I_{f2} K_f$ is approximately the same and state that:

$$\frac{B(\hat{O}_L : I_i \rightarrow I_{f1})}{B(\hat{O}_L : I_i \rightarrow I_{f2})} = \frac{< I_i K_i L \Delta K | I_{f1} K_f >^2}{< I_i K_i L \Delta K | I_{f2} K_f >^2}. \tag{2.33}$$

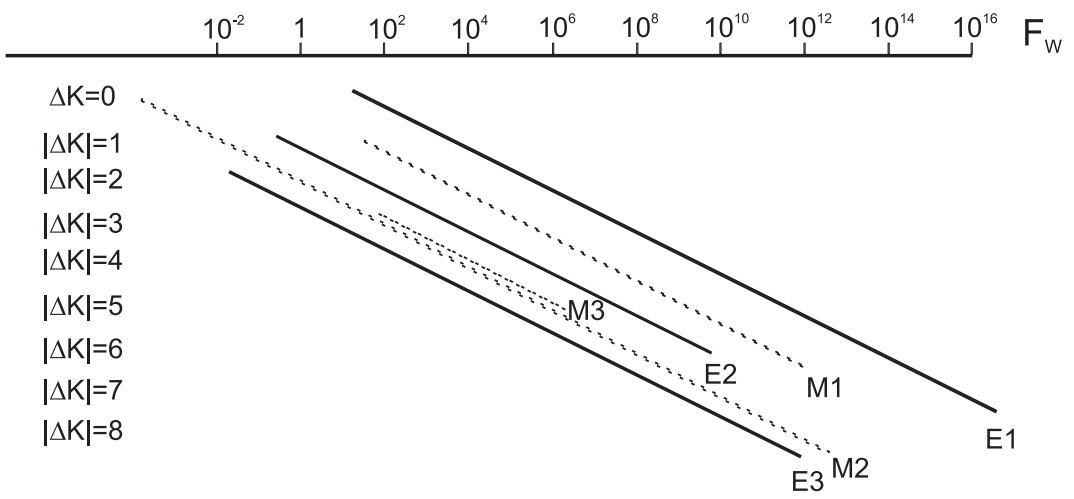

Figure 2.11: Trends of the hindrance factor relative to the Weisskopf estimate F_W drawn through systematic data by K.E.G Löbner in [Lob68] for different multipolarities.

When electromagnetic transitions connect states with different K-values, they can be forbidden with a consequential decrease in the transition probability. The degree of K-forbiddenness ν is defined by:

$$\nu = |\Delta K| - L. \tag{2.34}$$

It is evident from this expression that transitions with high multipolarity reduce the degree of K-forbiddenness and for K-forbidden transitions the slow, higher multipole transitions are able to compete with dipole and quadrupole decays. The hindrance factor F_W is defined by:

$$F_W = \frac{t^{\gamma}_{1/2}}{t^{W}_{1/2}} \tag{2.35}$$

where $t^{\gamma}_{1/2}$ is the partial γ-ray decay half-life and $t^{W}_{1/2}$ the theoretical Weisskopf single-particle estimate.
Systematic study by Löbner of the absolute transition probabilities of K-forbidden (single-particle) γ-ray transitions resulted in ranges of hindrance factors F_W for electric and magnetic γ-ray transitions which can be found in [Lob68]. In figure 2.11 the lines drawn through the experimental ranges in [Lob68] are shown as an illustration. A rough empirical rule was proposed by Rusinov [Rus61]:

$$log F_W = 2(|\Delta K| - L) = 2\nu \tag{2.36}$$

which shows that each additional unit of ΔK corresponds approximately to an additional factor of one hundred in hindrance.

An often used quantity is the hindrance per degree of K-forbiddenness f^ν which is defined by:

$$f^\nu = (F_W)^{1/\nu}. \tag{2.37}$$

A process competing with γ-ray decay is internal conversion where the excitation energy is transferred to one of the electrons of the inner shells of the atoms (e.g. K, L and M shell). The electron is emitted with an energy E_e:

$$E_e = E_{trans} - B_e \tag{2.38}$$

where E_{trans} is the energy of the transition and B_e the binding energy of the electron (see table 2.2). After emission of an inner electron, the vacancy in the electronic shell is filled by an electron and the released energy is carried away by a characteristic X-ray.

Table 2.2: Binding energies B_e of atomic electrons in nobelium for different atomic shells (in keV).

K	L1	L2	L3	M1	M2	M3	M4	M5
149.2	29.2	28.3	21.9	7.7	7.2	5.7	5.0	4.7

The total decay probability λ of a transition is given by the sum of γ-ray (λ_γ) and internal conversion (λ_e) decay probabilities:

$$\lambda = \lambda_\gamma + \lambda_e \equiv \lambda_\gamma(1+\alpha) \tag{2.39}$$

where the total internal conversion coefficient $\alpha = \lambda_e/\lambda_\gamma$ is defined. This coefficient is the sum of all partial conversion coefficients, i.e. $\alpha = \alpha_K + \alpha_{L1} + \alpha_{L2} + \alpha_{L3} + \ldots$. The closer the shell is to the nucleus, the higher the conversion coefficient, provided the binding energy B_e is not larger than the transition energy.
Internal conversion is important for high Z nuclei, low energy transitions and high multipolarity transitions. The conversion coefficient is also larger for magnetic transitions than for electric transitions, a fact that will play a major role in the study of transfermium nuclei. The conversion coefficients used in this work are calculated using the BRICC software [bricc].

The ratio of the conversion electron and γ-ray intensities gives direct experimental access to the conversion coefficient, and by comparing to the theoretical values the multipolarity of the transition can be deduced. When only one kind of radiation is detected experimentally, ratios of partial conversion coefficients can help in determining the multipolarity.

2.4.2 Alpha decay

The majority of transfermium elements in their ground state α decay where the mother nucleus ${}^{A}_{Z}\mathrm{X}_{N}$ emits a ${}^{4}\mathrm{He}^{2+}$ ion (i.e. an α particle) with a discrete energy E_α leaving the daughter nucleus ${}^{A-4}_{Z-2}\mathrm{Y}_{N-2}$. The α particle has spin and parity 0^+, carries away angular momentum l ($|I_i - I_f| < l < I_i + I_f$) and changes parity by $(-1)^l$. The energy E_α is characteristic of a certain isotope and aids in the identification of produced isotopes.

The α-decay process is generally treated as a two-step process, namely the preformation of an α particle inside the nucleus followed by penetration through the Coulomb barrier. The probability for the formation of the α particle is related to the reduced width δ^2 [keV], containing most nuclear information and defined as:

$$\delta^2 = \frac{\lambda h}{P} \tag{2.40}$$

with λ the partial decay constant and P the barrier penetration probability calculated using the Rasmussen formalism [Ras59]. In case the angular momentum carried away by the alpha particle is non-zero, an additional centrifugal barrier reduces the penetration probability.
The α decay can then proceed to the ground state or excited states in the daughter nucleus. To compare the decay strengths to different states, a hindrance factor HF can be defined as:

$$HF = \frac{\delta^2_{gs}}{\delta^2_{exc}} \tag{2.41}$$

where δ^2_{gs} and δ^2_{exc} are the reduced α-decay widths of ground-state to ground-state and ground-state to excited state decays, respectively.
The hindrance factor for transitions between odd-A nuclei HF_{odd} is defined in terms of the ground-state to ground-state transition in the even-even neighbours:

$$HF_{odd} = \frac{\delta^2_{A-1} + \delta^2_{A+1}}{2\delta^2_{decay}}. \tag{2.42}$$

The formation of an α particle involves a pair of neutrons and a pair of protons closely correlated in space and hence is sensitive to the pairing correlations acting amongst the nucleons and the similarity of the wave function of the initial and final states. Therefore transitions in odd-mass nuclei which involve a change of configuration of the odd quasi-particle are hindered and α decays between levels of the same quasi-particle structure are favoured.

2.4.3 Spontaneous fission

In nuclear fission the original nucleus splits into two lighter fragments with a higher binding energy per nucleon than the original nucleus. The fission process is inhibited by the Coulomb barrier and in general extra energy has to be added to the system for fission to occur. For very heavy elements, however, the fission barrier can be relatively low and exists mainly because of shell effects. In those elements, spontaneous fission can occur and is an important competing decay mode.

3 Experimental techniques

The study of transfermium nuclei poses a major challenge due to very low reaction cross sections and strong competition from fission. However, significant progress has been made during the last years due to the development of a new technique for in-beam spectroscopy, the construction of advanced focal plane systems at recoil separators and the increase in beam current coming from ECR ion sources.
Heavy-ion induced fusion-evaporation reactions provide the best way to produce heavy elements and were hence used in this work. The beam was provided by the ECR ion source and the K=130 MeV cyclotron at the Accelerator Laboratory of the University of Jyväskylä (JYFL).
The nuclei of interest were studied using the JUROGAM−RITU−GREAT *setup, providing an efficient collection system. The gas-filled separator* RITU *was designed for heavy ion studies where fast and efficient separation from unwanted products is required. Additionally, the recently installed spectrometers* JUROGAM *at the target position and* GREAT *at the focal plane of* RITU *allowed efficient detection of in-beam γ rays and decay products, respectively.* GREAT *also acted as a stop detector for the separated recoils. The data were collected with the newly designed* TDR *data-acquisition system and analysis was performed with the software package* GRAIN. *The combination of* JUROGAM, RITU, GREAT *and* TDR *allowed the recoil-gating and recoil-decay tagging (*RDT*) technique to be used, and made progress in the study of transfermium nuclei possible.*
This chapter will give a concise overview of the experimental techniques used in the in-beam, decay, and isomer spectroscopic studies in this work.

3.1 Production of heavy elements

Heavy-ion induced fusion-evaporation reactions are very useful in the study of nuclear structure as they can induce high angular momentum and excitation energy with reasonable cross sections. It has been the main method used so far for the study of transactinide elements.
A beam of ^{48}Ca ions is available at JYFL and was used in this work in combination with a ^{207}Pb or ^{208}Pb target to produce the nobelium isotopes ^{253}No and ^{254}No, respectively.

3.1.1 Beam production

The $^{48}Ca^{10+}$ ions were produced in the 14.6 GHz ECRIS (Electron Cyclotron Resonance Ion Source) at JYFL. In an ECR ion source, a plasma is kept in a magnetic trap formed by solenoids and a hexadecapole magnet. The originally neutral atoms are confined long enough to be ionised in step-by-step collisions with electrons, which are kept in motion by the introduction of resonant microwaves.
The highly-charged ions were subsequently injected into the $K = 130$ MeV cyclotron at JYFL. The maximum energy per nucleon which can be reached,

$$E/A = K\frac{q^2}{A^2} \tag{3.1}$$

(with A the mass number and q the charge state of the beam), is quadratically dependent on the charge state q and only linearly on the K-value. Therefore the creation of the highly charged ions in the ion source plays a very important role in production of high energy beams. The delivered beam energy has an accuracy of around 1 %.

3.1.2 Heavy-ion induced fusion-evaporation reactions

In heavy-ion induced fusion-evaporation reactions, beam and target nuclei fuse together into a compound system. The formation of such a compound nucleus requires a minimum energy to overcome the Coulomb barrier between beam and target nuclei. Assuming spherical nuclei, the Coulomb barrier B_c can be written in the simple form:

$$B_c \approx \frac{Z_p Z_t}{A_p^{1/3} + A_t^{1/3}} \ [MeV] \tag{3.2}$$

where p and t indicate the projectile (beam) and target nuclei, respectively. The compound system will have an excitation energy E^* defined by the reaction Q-value and the center of mass energy E_{cm}:

$$E^* = E_{cm} + Q. \tag{3.3}$$

For these heavy nuclei, fission dominates. The compound nuclei which withstand fission cool down through particle decay followed by γ-ray emission. Charged particle decay is suppressed in the region of interest due to the high Coulomb barrier of the high Z compound system and hence the emission of neutrons is favoured. When the energy is below the particle evaporation threshold, the de-excitation continues through γ rays. At first, the level density is very high and so-called statistical γ rays are emitted. These cannot be resolved and form a quasi-continuum background. The de-excitation paths finally end up close to the yrast line which represent the lowest energy state for a given spin. At that point, the γ rays are discrete and observable. They are detected

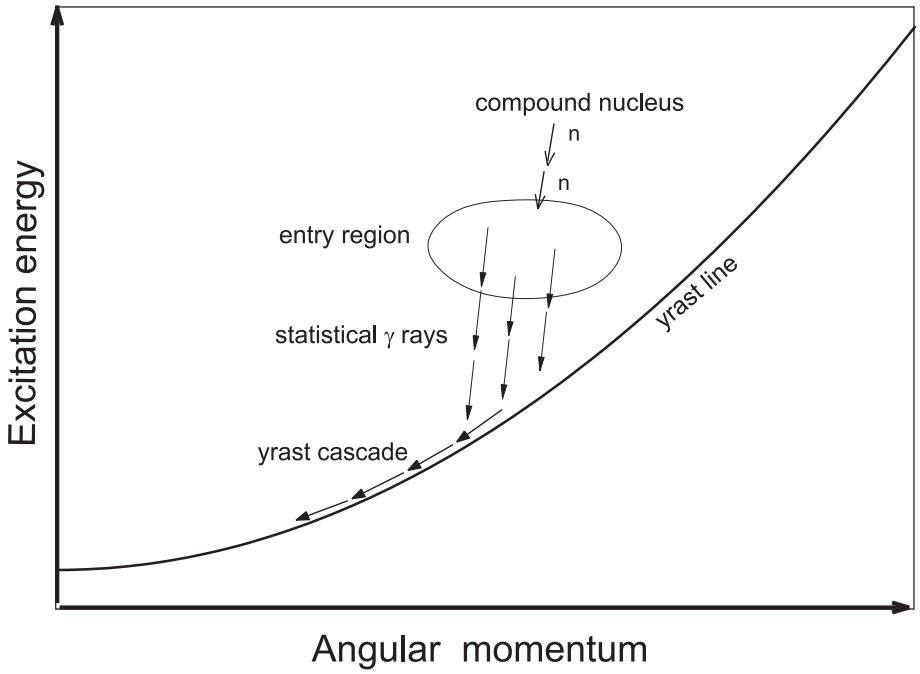

Figure 3.1: Schematic picture of the de-excitation process of the compound nucleus in heavy-ion induced fusion-evaporation reactions.

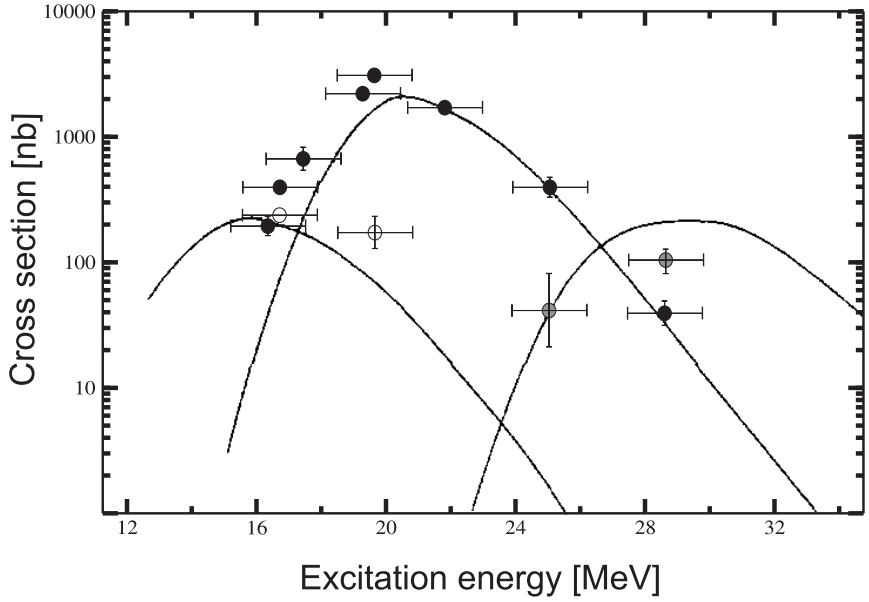

Figure 3.2: Evaporation residue cross section from the 1n (empty circles), 2n (black circles) and 3n (grey circles) evaporation channels from the ^{48}Ca+^{208}Pb reaction. The solid lines show the HIVAP predictions. [Gag89]

in in-beam spectroscopic measurements and can reveal the properties of the nucleus. The entire de-excitation process is pictured schematically in figure 3.1.

Cross-sections for the one, two and three neutron evaporation channels of the ^{48}Ca+^{208}Pb reaction are shown in figure 3.2. The small width of the excitation function indicates the action of two effects which both strongly reduce the cross section. The low energy side of the excitation function is cut by the Coulomb barrier penetrability, the high energy side by the fission which wins over the neutron evaporation and the 3n evaporation channel.
For beam energies around 220 MeV (i.e. $E^* \sim 23$ MeV), the competing reaction channels producing ^{253}No and ^{255}No through 3n and 1n evaporation, respectively, amount to less than 1 % of the total fusion-evaporation cross section.
By using target and projectile nuclei close to magic nuclei, the Q value is highly negative and cold fusion reactions are possible where the excitation energy E^* of the compound nucleus is around 20 MeV at the fusion barrier. The introduction of little excitation energy to the nucleus minimises the number of evaporation steps. As the probability for spontaneous fission goes down by minimising the evaporation steps, the 2n evaporation channel of this reaction has a relatively high cross section of ~ 2 μb. When using a ^{207}Pb target, the optimal cross section producing ^{253}No amounts to approximately 500 nb.
As the excitation function is narrow, the use of thick targets would not increase the yield and the target thicknesses are limited to around 500 μg/cm^2.

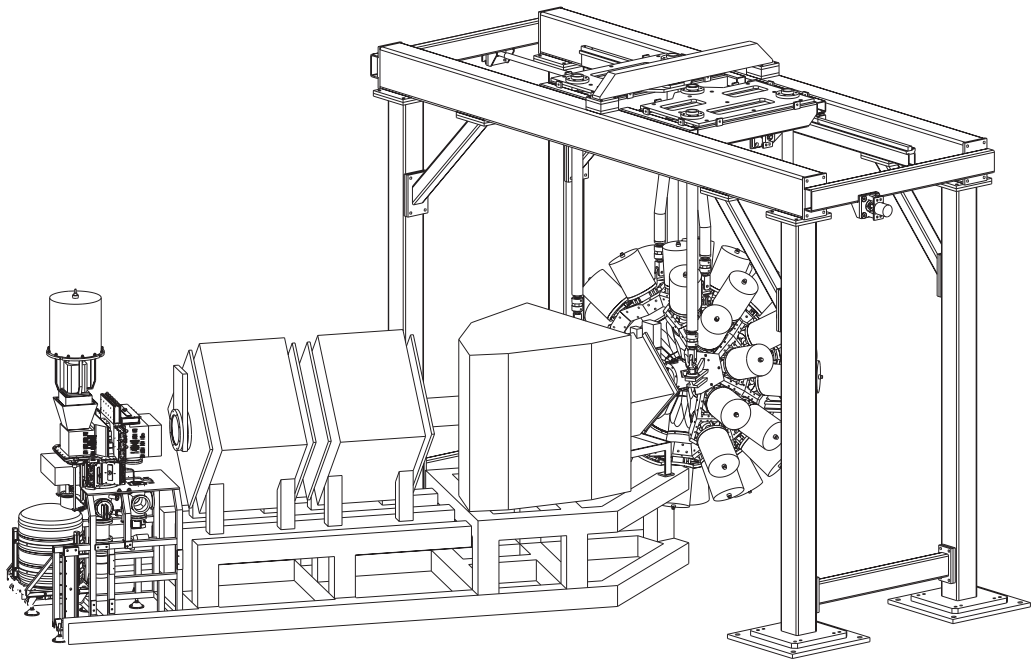

Figure 3.3: Schematic drawing of the setup: GREAT, RITU and JUROGAM. (beam direction: ←)

3.2 Experimental setup

In 2002-2003 two new spectrometers were installed and commissioned in JYFL to be used in conjunction with the gas-filled recoil separator RITU. The target germanium array JUROGAM, comprising 43 germanium detectors, has a higher efficiency than previous γ-ray spectrometers used at JYFL. The GREAT focal plane spectrometer has been designed to measure various types of decay radiation using a combination of germanium, silicon and gas detectors. Both spectrometers and the separator RITU will be described in more detail in this section.

3.2.1 The JUROGAM array of germanium detectors

In modern, multidetector γ-ray arrays one aims for a combination of high efficiency and energy resolution with a low background contribution. The best energy resolution is achieved with HPGe and the combination of several detectors in an array increases the γ-γ coincidence efficiency. The latter is important in high-spin studies where cascades of multiple γ rays are emitted.
In the energy region of interest to nuclear structure studies (100 keV -1.5 MeV), Compton scattering dominates the interaction between the incoming photons and

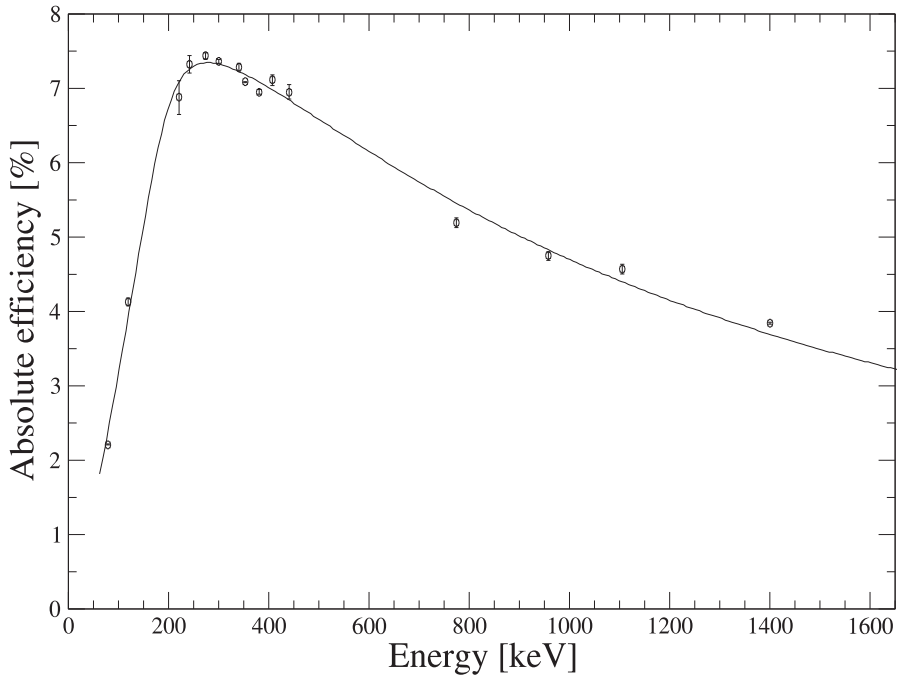

Figure 3.4: The absolute photopeak efficiency of the JUROGAM array.

the detector material, creating background by partial detection of the photon energy which is scattered out of the active detector volume. The addition of BGO Compton suppression shields helps to improve the peak to total ratio by suppressing the background coming from Compton scattered events.

In the JUROGAM array, 43 Eurogam Phase-I high purity germanium detectors with their individual Compton suppression shields are arranged in a honeycomb structure around the target [Nol90, Pak05]. The detectors sit in 6 different rings around the target at 157.6°(5), 133.57°(10), 107.94°(10), 94.16°(5), 85.84°(5) and 72.05°(8) with respect to the beam direction.
Usually 1 mm thick copper degraders are put in front of the germanium detectors to suppress contribution from X-rays from target and fission products, reducing the individual counting rates. The crystals are kept cool with liquid nitrogen and the regular filling of the detector dewars is fully automated.
The Phase-I germanium detectors of JUROGAM have an average FWHM of about 2.8 keV and an absolute total photopeak efficiency of 4.1 % at 1332 keV. To calibrate the detectors, ^{152}Eu and ^{133}Ba sources are placed at the target position. The absolute efficiency curve for the entire array obtained using those two sources is shown in figure 3.4 .
While performing the energy calibration of the detectors, a non-linear response of the ADC's was observed at low energy. To correct for this, a damped sine function was

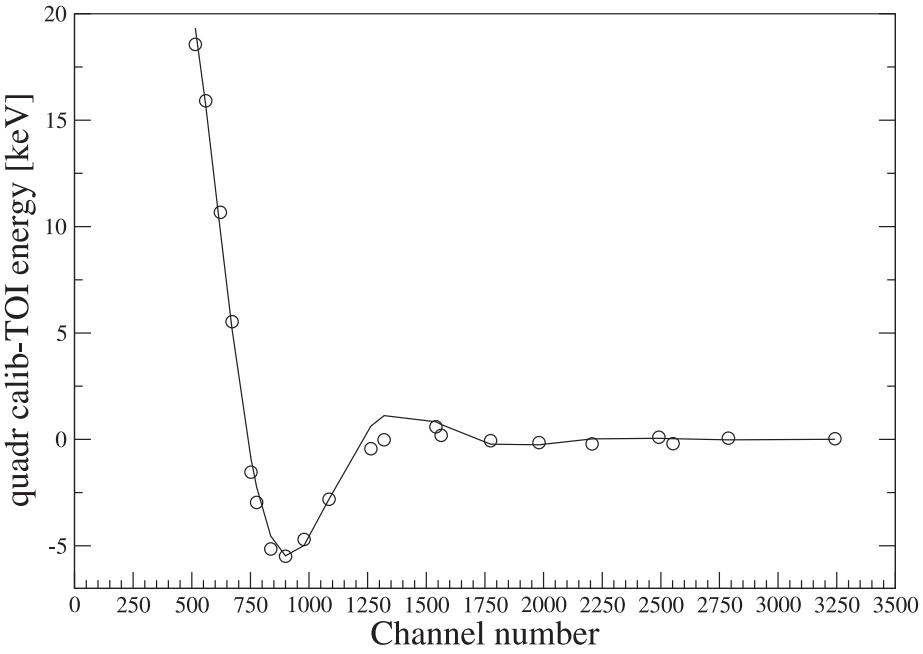

Figure 3.5: The non-linear behaviour of an ADC. Plotted is the difference between the calibrated energy (with quadratic calibration) and the energy as listed in the Table of Isotopes [Fir96] as a function of channel number for different γ-ray transitions of ^{152}Eu and ^{133}Ba. The solid line is a fit with an exponentially damped sinusoidal function. (This data set was generated with a lower amplifier gain in order to obtain more data points in the non-linear region.)

applied along with the quadratic calibration (see figure 3.5) and a good correspondence between channel number and photon energy was found down to 80 keV.

3.2.2 The RITU gas-filled recoil separator

In-flight recoil separators can be used to separate beam and fission products from te nucei of interest created in heavy-ion induced fusion-evaporation reactions. They can be operated in either vacuum mode (such as the FMA at ANL [Dav89]) or gas-filled mode (such as RITU at JYFL [Lei95, Uus96]). Vacuum separators have a good mass resolving power ($m/\Delta m \sim 300$) and allow neighbouring nuclei to be separated whereas gas-filled separators trade some mass resolution for higher transmission efficiency.

The fast and efficient gas-filled recoil separator RITU (Recoil Ion Transport Unit) comprises one magnetic dipole (D) and three quadrupole fields (Q) in a $Q_vDQ_hQ_v$-arrangement. Whilst the Q-fields are used to focus the beam in vertical (v) or horizontal (h) direction, the magnetic dipole is the actual dispersive element. RITU deviates from the standard DQQ configuration in that it has an extra focussing element before

the dipole to better match its angular acceptance.

The dipole chamber of RITU is filled with a constant flow of helium gas to keep impurities to a minimum. The helium gas provides charge-state focussing and hence better recoil transmission is achieved compared to vacuum-mode devices which only allow a few charge states to be collected.
In a heavy-ion induced fusion-evaporation reaction, the fusion-evaporation residues exit the target with a certain spread in energy, direction and charge state. For heavy elements, up to 30 different charge states are possible. As the ions move through the dilute gas of RITU, they undergo charge-exchange collisions and eventually reach an average charge state q_{ave}, approximated by the Thomas-Fermi model to be:

$$q_{ave} \approx (v/v_0)Z^{1/3} \tag{3.4}$$

where Z and v are the proton number and the velocity of the recoiling ion, respectively, and v_0 is the Bohr velocity.

The relationship between the magnetic rigidity $B\rho$ and the average charge state q_{ave} can then be expressed as:

$$B\rho = \frac{mv}{eq_{ave}} = \frac{mv}{((ev/v_0)Z^{1/3})} \approx \frac{0.0227A}{Z^{1/3}} \ [Tm] \tag{3.5}$$

where mv is the momentum of the reaction product. As for the recoils the radius ρ is fixed, equation 3.5 shows that RITU is indeed a mass separator. It also shows that to first order the magnetic rigidity is independent of the initial velocity and charge distribution and in principle 100 % charge transmission can be achieved. This is, however, at the expense of a poor mass resolving power due to the scattering processes with the helium gas. The optimal pressure of the helium gas is found by balancing the interplay between charge focussing and multiple scattering. An image size which nicely covers the focal plane detector is reached for a helium pressure of ~ 0.6 mbar for the reactions used in this work.

Recently, much development has taken place to reduce the level of unwanted products at the focal plane. A differential pumping system has been introduced to separate the gas in RITU from the beam-line vacuum, replacing the window system [Uus06]. A series of collimators and vacuum pumps allow a very fast transition from vacuum in the beam line to a helium pressure of ~ 0.6 mbar in RITU. The target is kept in helium which allows better cooling than in vacuum allowing for higher beam intensities.
In addition, better suppression of the beam particles was achieved with the installation of a larger dipole chamber and a beam dump further away from the optical axis of the dipole magnet. Also the beam stop was given a new shape to reduce the scattering of particles back into the separator [Gre03]. The total transmission of the RITU gas-filled separator amounts to $\sim$ 40 % for the heavy-ion induced fusion-evaporation reactions used in this work [Uus06] (with the dipole field $B = 1.1$ T). This number

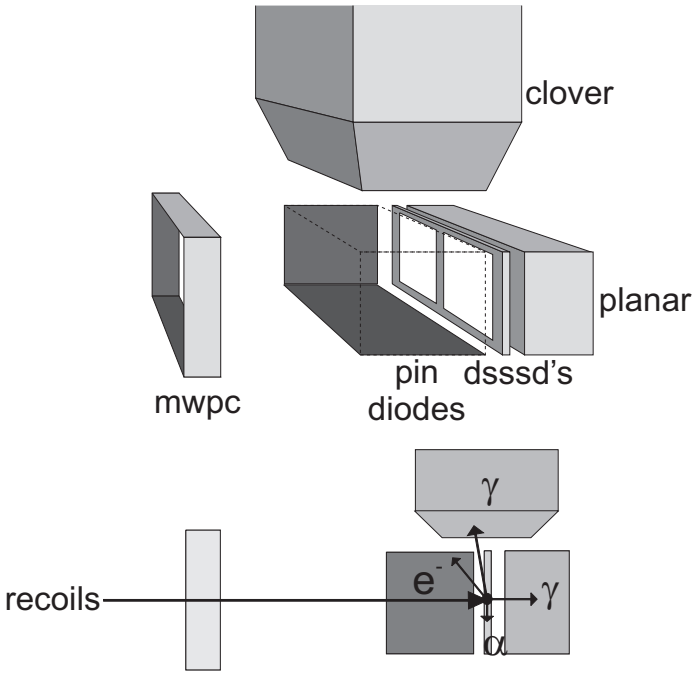

Figure 3.6: The schematic layout of the GREAT focal plane detector system.

takes into account both the angular acceptance of the magnets and an estimated 10 % additional loss due to lateral scattering of the recoils in the helium gas. In comparison, the transmission of the same reactions with the vacuum separator FMA amounts to only ~ 6 % [Uus06].

3.2.3 The GREAT focal plane detector spectrometer

GREAT stands for Gamma Recoil Electron Alpha Tagging which nicely summarises all its functions. The spectrometer was developed in a British collaboration between Daresbury Laboratory and the Universities of Liverpool, Manchester, Surrey, York and Keele [Pag03]. Even though designed as a portable device to be used at different laboratories, it has up to now been in permanent use in Jyväskylä at the focal plane of the RITU gas-filled separator.
GREAT is a highly efficient spectrometer for detecting the decay properties of reaction products at the focal plane of a recoil separator. It also plays an important role in the identification of evaporation residues based on energy and time of flight criteria. Figure 3.6 shows the layout of GREAT, comprising different detector types.

The recoils coming from the RITU separator are transmitted through the **Multi-Wire Proportional Counter** (MWPC) which acts as an active recoil discriminator. The

wires of the anode are 50 μm thick and 1 mm apart and have an aluminium cathode foil in between. Two thin mylar windows contain a volume filled with isobutane gas and also separate the 0.6 mbar pressure in RITU from the vacuum in the GREAT chamber. The recoils are then implanted into one of the **two Double-Sided Silicon Strip Detectors** (DSSSD's). The two 300 μm thick DSSSD detectors each have an area of 60x40 mm^2 with a strip pitch of 1 mm in both the vertical and horizontal direction, rendering a total of 4800 pixels. The high granularity allows for high counting rates and/or long correlation times. The total coverage can be estimated from the distribution of the detected α particles and was deduced to be $\sim$ 81 % for the experiments discussed here. The DSSSD's are normally operated at a bias voltage of +30 V.
As recoils are implanted typically only a few μm deep, about 45 % of the α particles escape the DSSSD detector. To detect those escaping α particles, **28 silicon PIN photodiode detectors** (PIN diodes) are arranged in a box in the backward direction from the DSSSD's, covering a solid angle of $\sim$ 30 %. Their amplifiers can also be tuned to measure conversion electrons. The PIN diodes each have an active area of 28x28 mm^2, a thickness of 500 μm and are operated at +80 V. Together with the DSSSD preamplifiers, they are mounted on a cooling block which is kept at -15 °C.
A **segmented Planar germanium detector** (PLANAR) is placed behind the DSSSD's to measure low-energy γ rays. The 120x60 mm^2 area of the PLANAR consists of 24x12 orthogonal strips with 5 mm pitch on both faces. The 15 mm thick crystal is normally operated at +800 V. The detector's casing is aluminium with a very thin (0.5 mm) Be window in front of the cathode and a thin (1.1 mm) Al window on the anode side. The cathode side is closest to the DSSSD detector and the thin beryllium entrance window allows the detection of low-energy γ rays. High-energy γ rays are detected with a large volume **segmented Clover detector** (CLOVER) placed above the GREAT vacuum chamber. This germanium detector has four individual crystals, each segmented further electrically in four parts, packed together in the same cryostat. A BGO shield is used for Compton suppression.

To calibrate the different detectors, a range of **calibration sources** is available. Two internal sources are placed in the GREAT chamber between the MWPC and the cooling block: a triple α source comprising the isotopes ^{239}Pu, ^{241}Am and ^{244}Cm with α energies in the range of $5-6$ MeV and a ^{133}Ba source for conversion electrons of $45-400$ keV. The sources can be moved in and out of the detectors' focus without breaking the vacuum in the GREAT chamber.
The PLANAR and CLOVER germanium detectors are calibrated using external ^{152}Eu and ^{133}Ba sources.
To calibrate the DSSSD and PIN detectors more accurately, a correction still has to be incorporated for the recoil effect and the absorption of energy in the dead layers of the detector. More precise calibrations can be done internally where known isotopes with a short half-life and decay energies close to the α-decay energy of interest are implanted into the DSSSD's. In this work, the ^{48}Ca+^{170}Er reaction was used, producing Ra and Rn α emitters via various evaporation channels.

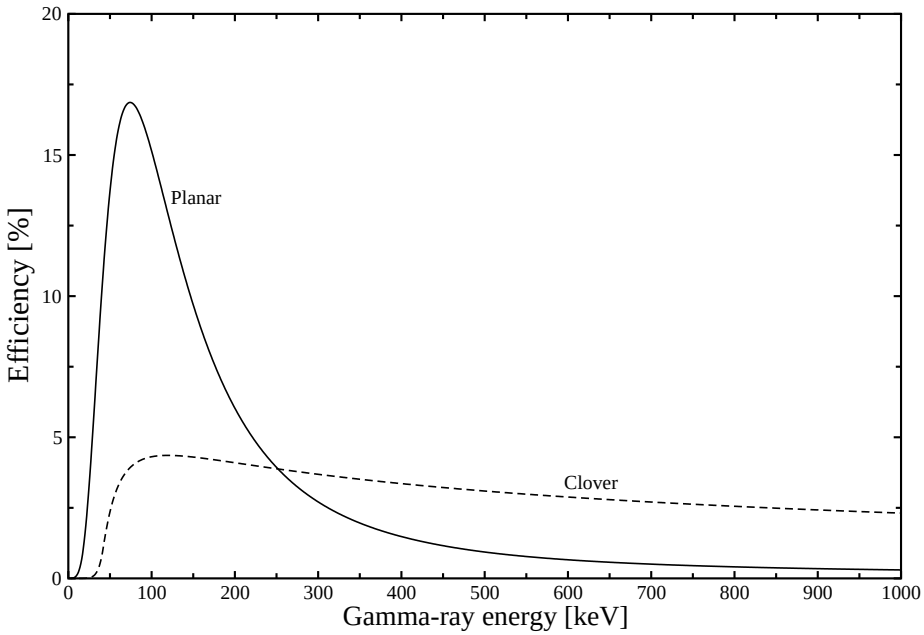

Figure 3.7: The simulated photopeak efficiency curves for the PLANAR (solid curve) and CLOVER (dashed curve) germanium detectors.

The efficiencies of the different detectors of the GREAT spectrometer have been simulated by Andreyev *et al.* [And04] using geant Monte Carlo simulations [geant] and are shown in figures 3.7 and 3.8.

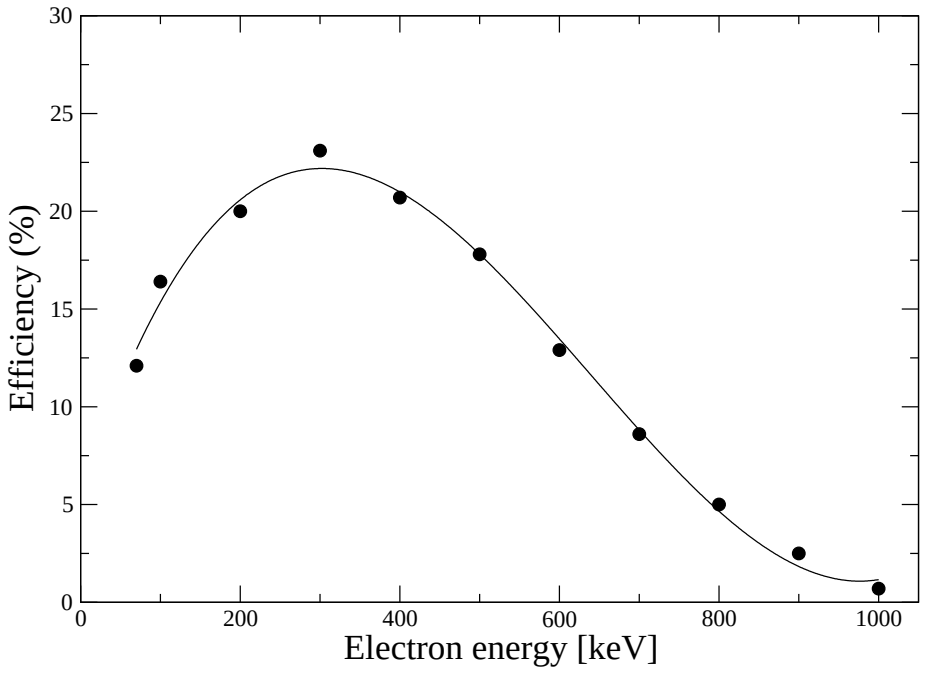

Figure 3.8: The simulated photopeak efficiency values for the PIN detectors. (solid line to guide the eye)

3.3 Data processing

The time and energy signals coming from the JUROGAM and GREAT spectrometers are handled by the triggerless Total Data Readout data-acquisition system. Online and offline analysis of the event structures is performed using the analysis package GRAIN.

3.3.1 Total Data Readout

The Total Data Readout (TDR) system is an integral part of the GREAT project [Laz01]. It is a triggerless data acquisition system, embodying a new approach to data-acquisition techniques. All channels are treated individually and as such the dead time is limited and only comes from the individual signal processing ($\sim$ 14 μs). The only common factor linking all the data channels in the entire system is a 100 MHz (i.e. 10 ns granularity) clock.
The front-end electronics consist of commercial NIM and CAMAC units. The signals are fed into the VXI ADC cards (Analog to Digital Converters) via linear amplifiers, and the ADC's are gated by the corresponding CFD (Constant Fraction Discrimina-

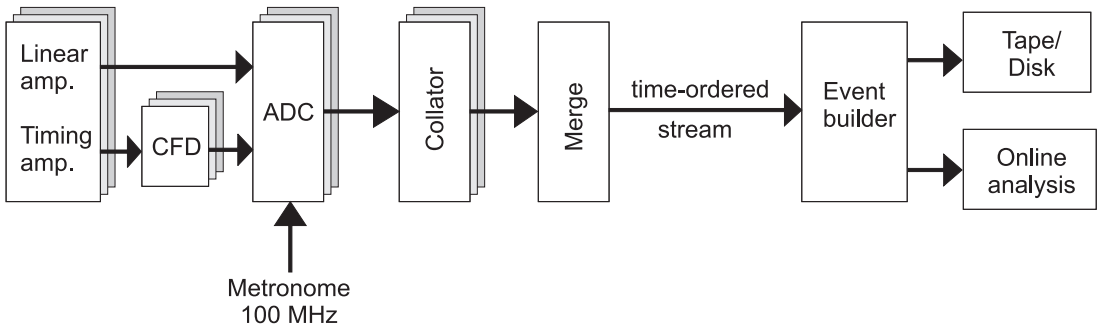

Figure 3.9: Schematic representation of the TDR system.

tor) signals. The 100 MHz clock is distributed from the metronome module to the VXI crates and subsequently distributed over the VXI backplane, providing the common clock for the timestamping of the different signals. Synchronisation is ensured by the metronome module which sends out a sync pulse every 655 μs to all ADC's. The output of the ADC cards is put in a time-ordered stream by collators and those streams are time ordered in the data merge. Here the time synchronisation is verified again and a single time-ordered data stream is sent to the event builder.
In the event builder, pile-up and Compton suppressed events get marked. If desired, the data can be pre-filtered, retaining for example only those events at the target position within a certain time window from a focal plane event. In the ^{254}No experiment no pre-filter was applied. Finally the stream is sent to a data-storage device, either DLT tapes or hard disks, and to the online sorting device. Figure 3.9 shows a schematic overview of the TDR system.

3.3.2 Analysis package: GRAIN

As the TDR is a fully triggerless system where all channels run independently, event reconstruction has to be done in software. This was done in the software analysis package GRAIN [Rah06], written in Java. The choice of 'trigger' is highly flexible and in this work the trigger was chosen to be any signal in the DSSSD, originating both from implantation and decay signals. An event is then reconstructed from a certain delay (a few μs) before the trigger and a chosen event length (12 μs for ^{254}No and 225 μs for ^{253}No). The event length in the ^{253}No experiment was chosen to be longer to allow observation of the isomeric decay of the implanted recoil. Within this trigger length all signals are stored in an event object.
The created events can then be analysed. Raw spectra can be filled, one- and two-dimensional time and energy gates can be applied and different time, energy and coincidence constraints can be set to selectively fill one- and two-dimensional spectra. The spectra shown in the following chapters are obtained in this manner.

3.4 Nuclear spectroscopy at RITU

In-beam γ-ray spectroscopic studies using JUROGAM allow determination of excited structures in nuclei. The rotational properties of transfermium nuclei provide information concerning their deformation and the maximum spin and excitation energy they can sustain. The variation of the moments of inertia with transition energy along a rotational band can be studied systematically. Additionally, for odd-mass nuclei configurations of the band-head states give direct access to information about single-particle configurations, while for even-even nuclei this information is accessible via the study of high-K states.
During in-beam experiments, simultaneous study of the nuclei at the focal plane can be carried out. Alpha-decay spectroscopy can be combined with coincident measurements of γ rays and electrons within the GREAT spectrometer to aid the determination of spin and parity of levels in the daughter nucleus.
Structures built upon isomeric states can be studied prompt in JUROGAM, looking for the transitions feeding the isomer. In GREAT, the transitions out of the isomeric state and its half-life can be observed. Those different spectroscopic techniques are used in this work and schematically depicted in figure 3.10. More detailed information concerning nuclear spectroscopy can be found in [Kan95, Eji89].

3.4.1 In-beam γ-ray spectroscopy and recoil-decay tagging

Electromagnetic transitions with simple selection rules provide a powerful tool to study nuclear structure. In an in-beam experiment the nuclei, created in an excited state using an accelerated beam, de-excite via γ rays and conversion electrons. The intensities and multipolarities of the electromagnetic transitions allow detailed level schemes to be built comprising rotational and vibrational structures.

However, when producing nuclei via heavy-ion induced fusion-evaporation reactions, a huge background is created in the prompt spectra due to the dominant fission channel. To make in-beam spectroscopic studies of heavy elements possible, the recoil-gating and recoil-decay tagging techniques were developed [Sim86, Pau95] where the fusion products of interest are selected on an event-by-event basis, dramatically reducing the background in the prompt γ-ray spectra.

Recoil-gating and recoil-decay tagging

The fusion-evaporation events are discriminated from scattered beam and target-like transfer products implanted into the DSSSD's by setting conditions on the time of

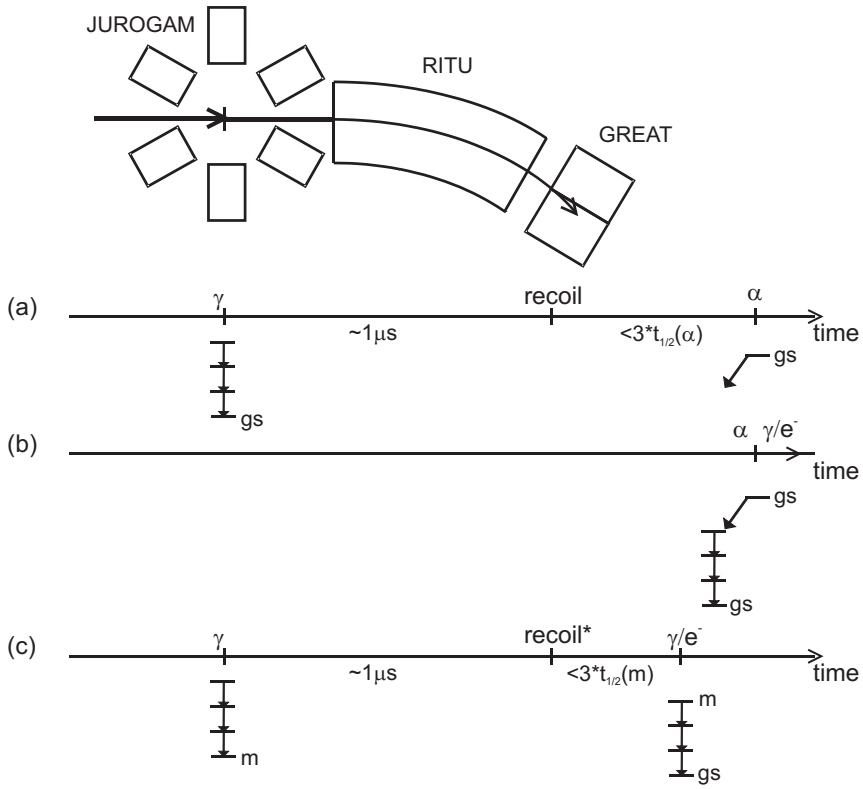

Figure 3.10: Schematic representation of the different spectroscopic techniques used in this work: (a) recoil-gating and recoil-decay tagging, (b) decay spectroscopy and (c) recoil-isomer tagging and isomer decay spectroscopy.

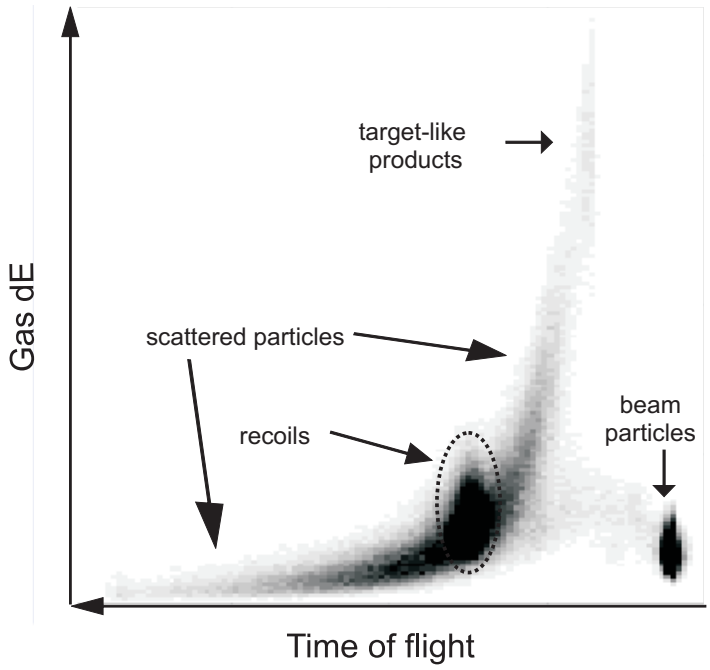

Figure 3.11: The energy loss in the MWPC versus the time of flight between the MWPC and the DSSSD's. The two dimensional gate selecting the recoils is shown and other reaction products are indicated.

flight between the MWPC and DSSSD's and the ΔE signal in the MWPC. An example of a matrix showing the time of flight versus energy loss in the gas detector is shown in figure 3.11. The two dimensional gate, displayed in figure 3.11 selects the recoils of interest. The background present in the gate from scattered beam and transfer products contributes about 40 % to the total number of events in the gate. Selection of the γ rays detected in the target array belonging to the events bounded by the two dimensional gate is known as the recoil-gating technique. The association of prompt γ rays with recoils is done in delayed coincidence, taking into account the flight time of the recoils through the separator (~ 1 μs). The time difference between the recoil implantation and the prompt γ-ray detection is shown in figure 3.12 and a prompt γ-ray selection gate is set on the peak around 1 μs as shown in the figure. The baseline structure is caused by the cyclotron frequency.
To be even more selective, the recoil-decay tagging technique (RDT) can be applied where the recoil is identified via its radioactive decay. Only those recoils passing the two dimensional gate are selected for which the isotopical characteristic α decay is detected in the same pixel of the DSSSD's. The α-decay signals are discriminated from recoil implants by requiring an anti-coincidence with the MWPC. To associate an α decay with a recoil implanted into the same pixel, a correlation time of up to three half-lives is employed. Random correlations between recoils and α particles occur as it is always assumed that the α decay belongs to the recoil which was previously

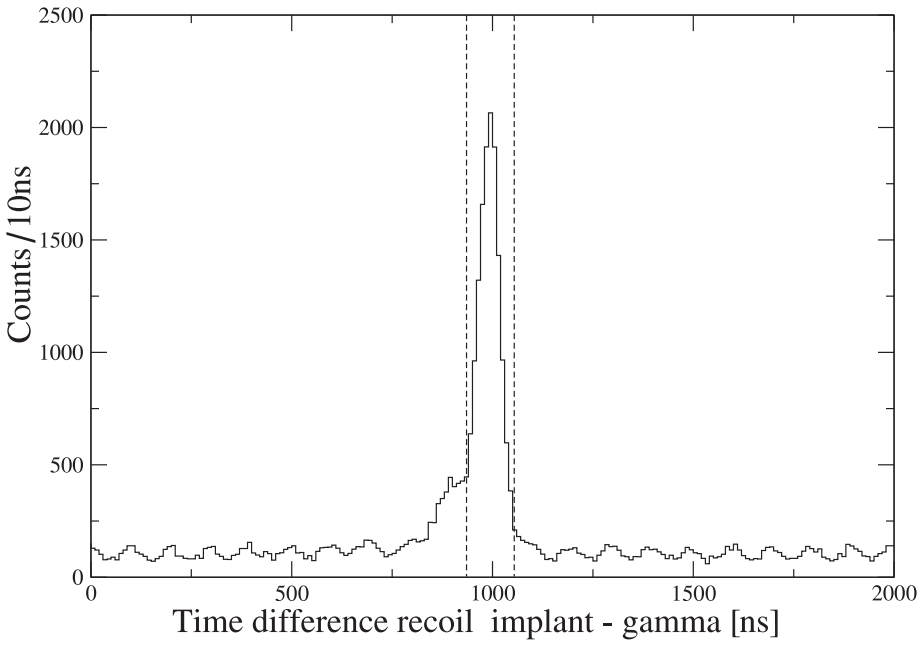

Figure 3.12: Time difference between the recoil implant and the γ-ray detection in JUROGAM. The gate selecting prompt γ rays is indicated with dashed lines.

implanted in the same pixel. These random contributions can be reduced by employing a large pixelation and finding a good balance between the implantation rate in the DSSSD's and the half-life of the nucleus. For studies of transfermium nuclei, the half-lives are rather long (e.g. 55 s for ^{254}No and 1.7 m for ^{253}No), but a very low implantation rate ($\sim$1 Hz) and the high granularity of the DSSSD's are sufficient to minimise random correlations.
Delayed coincidence with a recoiling nucleus identified through its characteristic decay renders a very clean prompt γ-ray spectrum. However, applying the recoil-decay tagging technique decreases the efficiency due to losses connected to the detection of the characteristic α decay.
Therefore, the majority of the analysis presented in following chapters is based on the technique of recoil-gating to extract the prompt γ rays of interest.

3.4.2 Decay spectroscopy

The characteristic energy of an α particle provides a spectroscopic signature of the isotope under study. At the same time nuclear structure information can be derived. As α decays prefer to couple identical structures, assignment of the quasi-particle structure of an unknown level can be made if it is linked to a known structure via an unhindered α decay.

Using the GREAT spectrometer, low and high-energy γ rays and conversion electrons can be detected in coincidence with the α-decay. Multipolarity determination of those electromagnetic transitions aids the spin assignment and the construction of a level scheme in the daughter nucleus.

3.4.3 Isomer decay spectroscopy and recoil-isomer tagging

Isomeric states are characterised by their retarded decay. This slow decay can be caused by the absence of a decay path via low multipolarity transitions. According to the Weisskopf estimates of table 2.1 only low multipolarity transitions are likely to be detected at the target position (e.g. only $E1$, $M1$ and $E2$ for $E_\gamma \sim 250$ keV and $A \sim 250$). In other cases, the recoil is transported in an isomeric state to the focal plane where it decays into the ground-state, provided the lifetime is longer than the ~ 1 μs flight time through RITU. Delayed γ-rays and conversion electrons emitted when the recoil is implanted in an isomeric state are associated to the recoil for up to three isomeric half-lives.
Measurement of the life-time and the multipolarity of the electromagnetic decay out of the isomeric state can provide information on its configuration.

A promising approach in the very heavy element region is to study bands built on multi quasi-particle states. Due to the presence of many high-K single-particle orbitals near the Fermi surface in the transfermium region, several high-K states are expected with rotational bands built on top of them. As they can sometimes only decay by K-forbidden transitions, they may become isomeric.
Determining the configuration of a high-K isomer by its feeding or de-exciting electromagnetic transitions gives information on the single-particle states around the Fermi surface. Since $E_{2qp} > 2\Delta$ the excitation energy of a 2 quasi-particle state provides an immediate upper boundary for the pairing gap Δ.
Jones has suggested a method to detect such high-K isomers with the setup described in section 3.2 using the DSSSD's as an electron calorimeter (see [Jon02]).

Recoil-isomer tagging

Not only the decay out of the isomer but also the transitions feeding into the isomeric state can be observed. To select the transitions built on top of the isomer, those recoils are selected which decay via an isomeric transition at the focal plane. The prompt γ rays observed in JUROGAM and associated with those recoils are then assigned as transitions built on top of the isomeric state.

4 Spectroscopic study of transfermium nuclei: ^{253,254}No

In this chapter the results and data-analysis of two experiments carried out at JYFL are described: the in-beam gamma-ray spectroscopic study of ^{254}No and the in-beam and decay spectroscopic study of ^{253}No. They are part of a series of experiments studying transfermium nuclei in the region around ^{254}No. The motivation for studying these elements in a quest for the next doubly magic nucleus beyond ^{208}Pb is given below. Some properties of ^{254}No and ^{253}No are already known from previous experimental investigations. A variety of theoretical predictions also exist and will be briefly summarised before the new results are presented.

4.1 Motivation

A long-standing challenge in nuclear physics research has been the exploration of nuclei at the limits of existence. One extreme region is that of high mass and charge, the superheavy elements. The mere existence of superheavy elements has been a long-standing fundamental scientific problem. For nuclei with $Z \gtrsim 100$ the liquid-drop barrier vanishes as the Coulomb repulsion overcomes the attractive nuclear interaction. It was found that the relative stability of those nuclei against fission is generated entirely by microscopic shell corrections to the liquid-drop energy.

The high-mass end of the chart of the nuclides is shown in figure 4.1. The heaviest elements synthesised to date which have been confirmed and named are $Z = 110, 111$ and element $Z = 112$ has been observed by three independent experimental groups. The isotopes were identified on the basis of their decay properties using the unambiguous parent-daughter $\alpha - \alpha$ correlation, identifying an unknown species by correlation of its decay properties to those of the known daughter activities.

Several theoretical calculations have been carried out in an attempt to describe the properties of the heaviest nuclei. In the beginning, particularly successful calculations were made based on the macroscopic-microscopic method (see e.g. [Cwi94]). Different potentials were used and the studies were able to reproduce the masses of the heavy elements and they predicted the spontaneous fission half-lives to be long.
Due to increasing computational abilities, it has recently become possible to describe

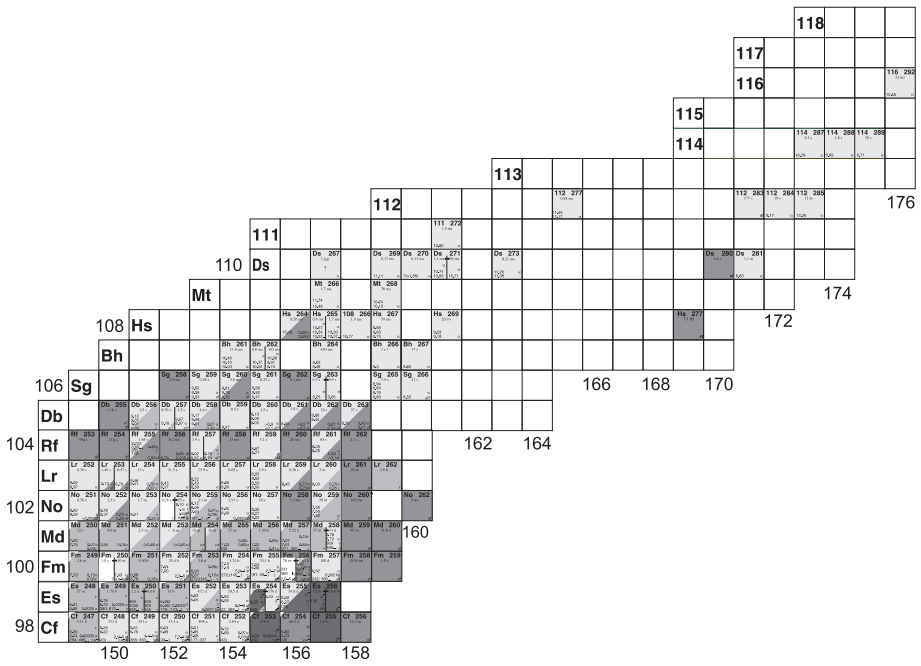

Figure 4.1: High-mass end of the chart of the nuclides including some non-confirmed observations of elements $Z = 114, 116$.

the superheavy nuclei with fully self-consistent calculations based on the Hartree-Fock approximation with Skyrme or Gogny interactions (non-relativistic mean-field models, see e.g. [Ben03] and [Dug01]) or with the relativistic mean-field approximation (e.g. [Afa03]).

Although those calculations can reproduce some of the experimentally available data, the exact location of the next doubly magic nucleus after ^{208}Pb and the predicted island of spherical stability around it is still unknown and has been the subject of much theoretical debate. According to most non-relativistic mean-field models, the next spherical shell closures are expected to be $Z = 124, 126$ and $N = 184$ [Ben99, Ben03a] and predicted to be situated around $Z = 120$, $N = 172$ by relativistic mean-field models [Afa03], depending on which forces and parametrisations are used. Macroscopic-microscopic calculations on the other hand favour $Z = 114$ and $N = 184$ [Cwi94]. Calculations of the shell-correction energy using the Strutinsky shell correction method and the position of some predicted spherical magic shell closures are shown in figure 4.2.

To solve the theoretical discrepancies, more experimental data are needed. Due to the low cross sections (sub-nanobarn), extensive spectroscopic studies of elements with $Z > 106$ are extremely difficult. Important information about the properties of the heaviest nuclei therefore comes indirectly from investigating lighter shell-stabilized

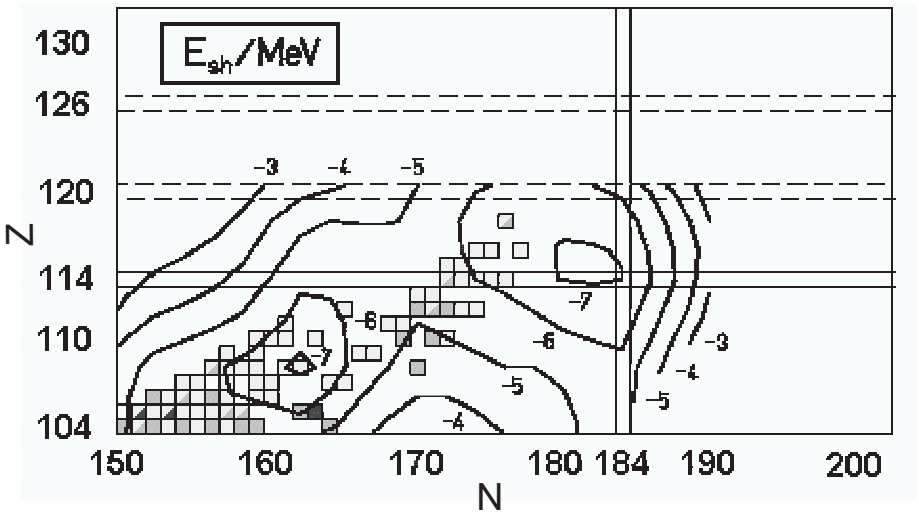

Figure 4.2: Contour map of the ground-state shell-correction energies E_{sh} (see equation 2.26) to the potential energy around the predicted island of stability. The positions of the next magic shell closures are indicated. A second minimum can be observed at the $Z = 108$ and $N = 162$ deformed shell gaps. [Smo95, Hof00]

nuclei around ^{254}No which are accessible for in-beam studies. In a systematic study to get to the superheavy island of stability, both reaction mechanisms and nuclear structure properties of those transfermium nuclei can be investigated. Such studies can test the reliability of predictions made by the various theories trying to describe the heaviest elements and put constraints on the calculations.

The quantum shell-correction energy favours shape deformation for certain numbers of nucleons and indeed many very heavy elements seem to be well deformed. A second region of enhanced stability, this time strongly deformed, is predicted around $N = 162$ and $Z = 108$ [Cwi94] and is visible in figure 4.2. Several calculations also predict deformed shell gaps at $N \sim 152$ and $Z \sim 100$ around ^{254}No [Cwi94, Ben03].
Experimental confirmation of large quadrupole deformation in the very heavy element region has come from γ-ray spectroscopy around ^{254}No. Because of the deformed nature of transfermium nuclei, some of the Nilsson orbitals active at the Fermi surface in nuclei around ^{254}No are derived from down-sloping single-particle levels active around the predicted spherical superheavy island of stability (see figures 2.5 and 2.6). Those single-particle levels can then be extrapolated to zero deformation at higher neutron or proton number and give an idea of the level ordering at sphericity.

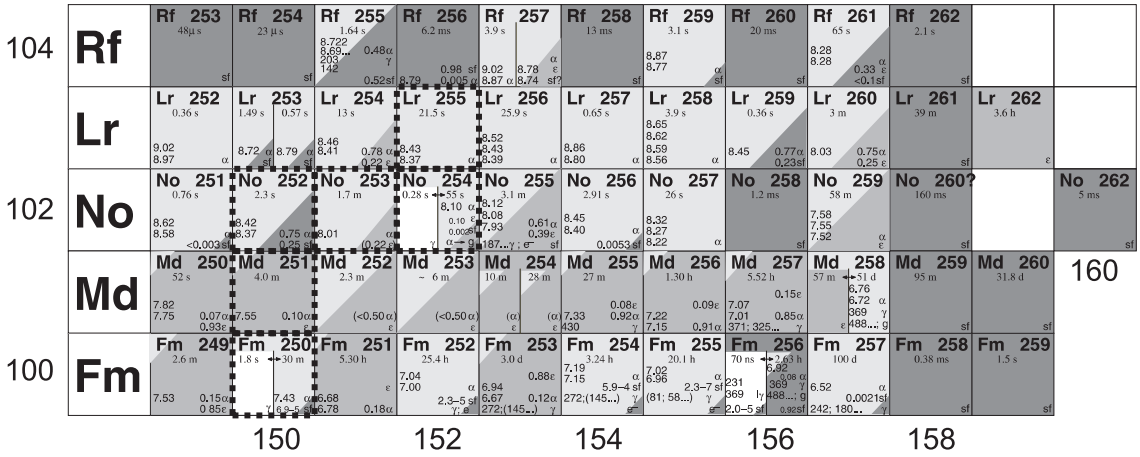

Figure 4.3: Extract of the nuclear chart in the ^{254}No region. The transfermium elements studied in-beam so far are marked with dotted boxes. (Light grey for α-decay, medium grey for EC+β^+ and dark grey for spontaneous fission.)

4.2 Previous theoretical and experimental knowledge

In-beam spectroscopic studies of transfermium elements are very challenging. Fusion-evaporation reactions have relatively low cross sections and a strong competition of fission, requiring a recoil separator with detectors at its focal plane for channel selection. Furthermore many of the transitions are highly converted and information on both γ rays and conversion electrons is necessary to get a full picture of the nucleus under study. But in recent years a lot of progress has been made and several in-beam experiments have been carried out at two separators: FMA at ANL (Argonne) and RITU at JYFL (Jyväskylä). Figure 4.3 gives an overview of the transfermium nuclei studied at those two facilities.
The GAMMASPHERE target array coupled to the FMA (Fragment Mass Analyser) separator consists of 101 germanium detectors with a γ-ray singles photopeak efficiency of 10 % at 1.3 MeV, much higher than that of the present target detector array JUROGAM at JYFL (4.1 %). However, due to the much higher transmission efficiency of RITU ($\sim$ 40 %) compared to the FMA ($\sim$ 6 %) for transfermium recoils, the present setup at JYFL is more efficient for γ-ray singles and both setups are about equal in γ-γ coincidence efficiency. The germanium detector arrays previously used at JYFL were less efficient.

Apart from in-beam measurements, several decay experiments and theoretical studies have already been carried out in the transfermium region around ^{254}No. An overview of the previously known properties of ^{254}No and its odd-mass neighbour ^{253}No are presented in the following sections.

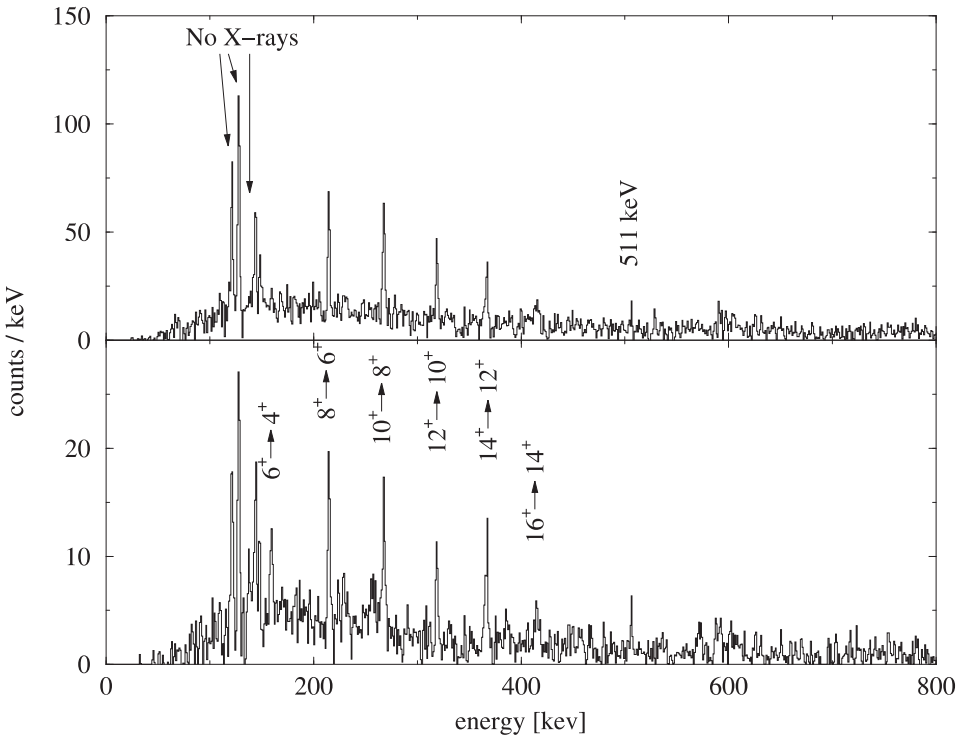

Figure 4.4: Recoil-gated (upper panel) and α-tagged (lower panel) ^{254}No γ-ray singles spectra taken with the SARI array. [Lei99]

4.2.1 The even-even nucleus ^{254}No

The first correct synthesis of element 102 was reported by Ghiorso *et al.* in 1958 [Ghi58]. The ground-state rotational band of ^{254}No was observed several decades later in a pioneering in-beam γ-ray experiment carried out at ANL employing GAMMASPHERE coupled to the FMA [Rei99]. This and all subsequent experiments used the recoil-gating and recoil-decay tagging techniques described in section 3.4.1. In the initial experiment the ground-state band was observed up to a spin of $14\hbar$. A follow-up experiment carried out using the SARI unsuppressed Clover germanium detector array coupled to the gas-filled recoil separator RITU at JYFL confirmed this observation and extended the band to a spin of $16\hbar$ [Lei99]. The recoil-gated and α-tagged γ-ray singles spectra obtained in that experiment are shown in figure 4.4.
These experiments allowed a value for the quadrupole deformation parameter, β_2, of 0.29(2) to be derived from the extrapolated energy of the lowest 2^+ state [Her02a], in good agreement with theory: theoretical predictions range from $\beta_2 = 0.25$ by macroscopic-microscopic models to $\beta_2 \sim 0.3$ by relativistic mean field calculations (see [Her04] and references therein). The ground-state band was extended to a tentative spin of $20\hbar$ in a further experiment carried out at ANL to study the entry

distribution, fission barrier and formation mechanism of ^{254}No [Rei00]. The entry distribution is defined as the phase space available for the last nucleon evaporation (see figure 3.1) and hence gives the initial angular momentum and excitation energy of the ^{254}No recoils. This entry distribution depends on the bombarding energy and for a beam energy of 219 MeV the observed feeding was centered around spin $15\hbar$ with most of the intensity coming in between spin $10\hbar$ and $20\hbar$. It was also deduced that the fission barrier still amounts to at least 5 MeV at spin $20\hbar$. This was confirmed by Hartree-Fock-Bogoliubov calculations with a Gogny force in [Egi00] and with a Skyrme force in [Dug01] and the fission barrier was predicted to persist up to spin values of $\sim 40\hbar$ or even higher. Altogether the results show the robustness of shell-effects against rotation in this region of the nuclear chart.

A two quasi-particle $K^\pi = 8^-$ state has been predicted to lie below 1.5 MeV in ^{254}No by different theoretical calculations [Laz89, Sol91]. A candidate isomeric decay for this configuration was observed in the 1970's by Ghiorso *et al.* with a measured half-life of 280(40) ms [Ghi73]. The decay out of the isomer could not be observed but the $K^\pi = 8^-$ state was assumed to decay into the $I^\pi = 8^+$ level of the ground-state band. Several experiments were carried out over the years at Jyväskylä [But03] and Argonne [Muk05] but none was able to detect the presumed $8^- \rightarrow 8^+$ transition linking the isomer to the ground-state band of ^{254}No.
Indirect evidence for the presence of high-K bands was obtained in an in-beam conversion-electron study carried out at JYFL. The experiment employed the SACRED conversion-electron spectrometer [But96, Kan04] coupled to RITU. Figure 4.5 shows the recoil-gated prompt conversion-electron spectrum of ^{254}No.
A broad distribution of events centered around 100 keV was observed which has a much higher electron multiplicity than the discrete transitions. It was shown to be of nuclear origin and deduced to arise from $M1$ transitions built on high-K multi quasi-particle states [But02]. In figure 4.5 a simulation of this broad distribution is shown when assuming it arises from bands built on such high-K states.
In this in-beam conversion-electron experiment the 4^+ to 2^+ transition could be observed for the first time and a transition energy of 101.1(6) keV was deduced. Unfortunately the 2^+ to 0^+ transition could not be detected as for this transition the electrons can not overcome the high-voltage barrier applied between the target position and the detector to suppress the background of low-energy δ electrons. The $E2$ multipolarity of the lowest observed transitions (up to 10^+ to 8^+) was confirmed [Hum04]. It was furthermore deduced that about 40 % of the population of ^{254}No proceeds through high-K bands, presumably terminating in isomeric states [But02].

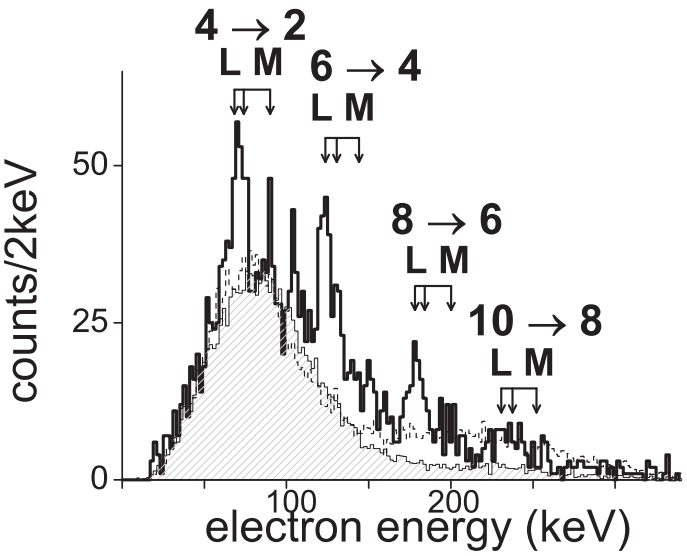

Figure 4.5: Electron data of ^{254}No obtained with SACRED showing the recoil-gated prompt conversion-electron spectrum with marked ground-state band transitions. A simulation of the broad distribution due to the decay of high-K bands is also shown (shaded region). [But02]

4.2.2 The odd-mass nucleus ^{253}No

The lowest lying levels in odd-N nuclei are essentially determined by the odd neutron and should thus be similar for all isotones with even Z. For the $N = 151$ isotonic chain, the ground state is assumed to be $9/2^-$ as predicted by theoretical calculations. The heaviest nucleus with a measured 9/2 ground-state spin in this chain is ^{247}Cm [Abr73]. The calculated lowest lying single-particle levels for some $N = 151$ isotones are shown in figure 4.6 for two different theoretical approaches: Nilsson-Strutinsky macroscopic-microscopic calculations with a Woods-Saxon potential by S. Cwiok *et al.* [Cwi94] and HFB calculations with a Skyrme force by P.-H. Heenen [Hee05]. Even though they both predict $9/2^-$ as the ground state, the order and excitation energies of the low-lying excited states are different.

Experimental information on the structure of odd-mass transfermium nuclei has until recently almost solely come from α-decay studies. The assignment of single-particle levels is then essentially based on the analysis of hindrance factors of the α-decay transitions and systematics. This alone, however, does not firmly pin down the configurations of the states.
Sometimes decay studies of the parent nucleus has allowed construction of an extensive level scheme. In the case of ^{249}Cf, an isotone of ^{253}No, the electron capture decay of its parent ^{249}Es was studied and the three lowest single-particle states in ^{249}Cf were determined to be $9/2^-[734]$ (0 keV), $5/2^+[622]$ (145 keV) and $7/2^+[624]$ (379.5 keV)

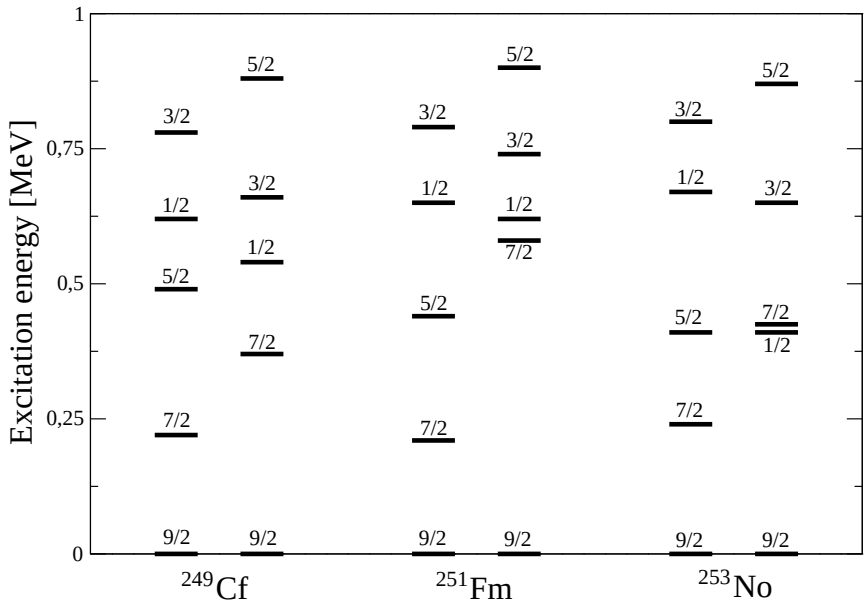

Figure 4.6: Position of the neutron single-particle states $9/2^-[734]$, $7/2^+[624]$, $5/2^+[622]$, $1/2^+[620]$ and $3/2^+[622]$ in some N=151 isotones. The left hand columns are states calculated by Cwiok *et al.* [Cwi94] and the right hand columns states calculated by P.-H. Heenen [Hee05].

respectively [Ahm76a].

Recent technical developments have made it possible to study α-γ coincidences in decay measurements, where the determination of the γ-ray multipolarity aids the assignment of the spin and parity of the states.
Two α-γ decay studies of ^{253}No have been carried out, one at JYFL [Her04] during the commissioning of a GREAT prototype and a confirmation experiment at GSI [Hes04], leading to the identification of three states in the α-decay daughter nucleus ^{249}Fm.

A disadvantage of decay studies is that a heavier nucleus has to be populated, which generally means an even lower cross-section. Also the interpretation may be complicated due to the summing of the electrons and alpha particles in the same detector. However, in-beam studies of odd-mass nuclei are more complicated than those of even-even nuclei because of the fragmentation of the population between different bands and often dominating internal conversion. In well deformed nuclei, the two signature partners of stretched $E2$ transitions are linked by $M1$ transitions which can be strongly converted. Whether the decay goes mainly via stretched $E2$ or $M1$ transitions is determined by the single-particle structure of the band-head, and more specifically the $g_K - g_R$ factor as can be seen from equation 2.31. Only bands built on states with positive g_K values close to $g_R \approx 0.4$ decay mainly via stretched $E2$ transitions. Out of the lowest lying states of the $N = 151$ isotones, only the $7/2^+[624]$ state has a g_K value that favours $E2$ transitions. While in-beam electron spectroscopy is more

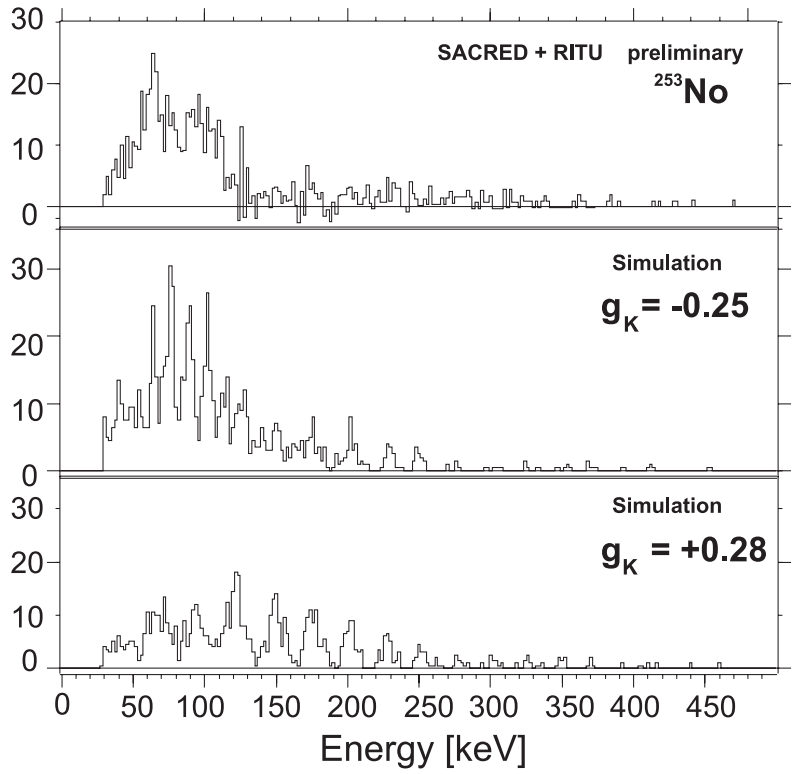

Figure 4.7: Background subtracted conversion-electron spectrum of ^{253}No observed with SACRED in the upper panel. Lowest two panels show results of two simulations with different assumptions for the band-head configuration. [Her02]

sensitive to the highly converted $M1$ transitions, in-beam γ-ray spectroscopy favours the observation of stretched $E2$ bands.

An in-beam conversion-electron study of ^{253}No was performed at JYFL with SACRED coupled to RITU [Her02, Pag03a]. The total singles conversion-electron spectrum (background subtracted) is shown in the upper panel of figure 4.7. To determine the origin of the detected electrons, two simulations were made of bands with different single-particle character, assuming that all the decay intensity goes through one strongly-coupled band. The middle panel with $g_K = -0.25$ corresponds to the simulated electron spectrum of a band built on the $9/2^-[734]$ single-particle state, decaying mainly via $M1$ transitions while the lower panel with $g_K = +0.28$ shows the simulated spectrum in case of a band built on the $7/2^+[624]$ single-particle state, decaying primarily via $E2$ transitions. Comparing the simulated and experimental spectra from figure 4.7, the observed spectrum seems more consistent with the spectrum from a band built on the $9/2^-[734]$ state. Improved experimental data are however needed to make a more reliable judgement.
Recently, a rotational band of ^{253}No was observed in an in-beam γ-ray study at ANL.

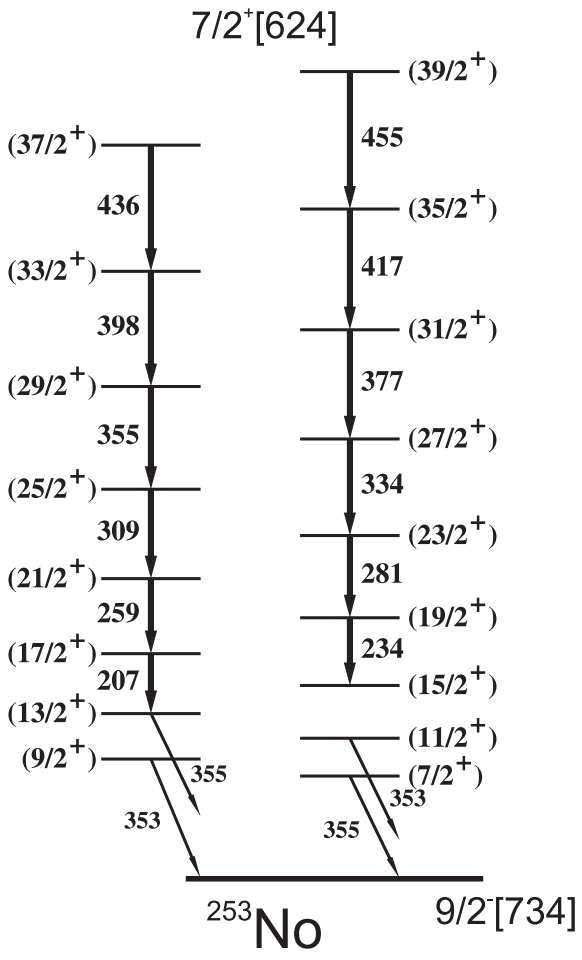

Figure 4.8: Level scheme of ^{253}No as proposed by Reiter *et al.* [Rei05].

Reiter *et al.* [Rei05] assigned the transitions to a band built upon the $7/2^+[624]$ state and placed the band-head at an excitation energy of 355 keV above the $9/2^-$ ground state. The level scheme of ^{253}No proposed by Reiter *et al.* is shown in figure 4.8. The assignment of the band-head configuration was mainly based on the positive g_K value of the state, favouring the decay via stretched $E2$ transitions. Also a decrease in K X-ray intensity, indicative for the presence of converted transitions, for higher γ-ray multiplicity was used to support the assignment. The 355 keV transition is a member of the ground-state band but was assumed to be part of a quintuplet based on the broadened peak shape in the spectrum [Rei05, Kho06].
In the isotone ^{251}Fm, the $7/2^+$ level was placed at $E^* = 354$ keV based on an α-γ coincidence study [Hes06] and although both assignments are tentative, they are in rough agreement with the calculations. The alpha decay of ^{257}Rf to the $7/2^+$ state in ^{253}No is strongly hindered and it will hence be difficult to observe this transition and deduce the energy of the $7/2^+[624]$ single-particle state in this manner.

An isomeric state in ^{253}No was observed in different experiments studying the α decay of ^{257}Rf. In 1973 Bemis *et al.* [Bem73] used the reaction ^{249}Cf(^{12}C,4n)^{257}Rf in an experiment to establish the atomic number of the daughter of an α decay, attributed to ^{257}Rf, by its coincidence with nobelium K X-rays. They found that ten out of thirteen coincident K X-rays were not prompt but originated from an isomeric structure in ^{253}No at an excitation energy of approximately 300 keV with a half-life of 31.3(41) μs. More than two decades later, Hessberger *et al.* [Hes97] used two different reactions to produce ^{257}Rf, namely ^{208}Pb(^{50}Ti,n)^{257}Rf and ^{208}Pb(^{58}Fe,n)^{265}Hs which gives ^{257}Rf as an α-decay granddaughter. In this study the α line of 8779 keV was attributed to the decay into the (isomeric) $5/2^+[622]$ level in ^{253}No. The excitation energy of the $5/2^+$ state was then taken as the difference between that α line and the one attributed to the decay into the ground state of ^{253}No, resulting in an energy of the isomeric state of around 124 keV. As this is below the K-electron binding energy, it is in contradiction with the results found by Bemis *et al.*.
An isomeric state with similar excitation energy ($\sim$ 200 keV) and half-life ($\sim$ 25 μs) has been observed in different $N = 151$ nuclei, suggesting the same configuration to be present in all isotones. It should be noted that the calculations shown in figure 4.6 place the $5/2^+[622]$ state above the $7/2^+[624]$ state and hence do not predict an isomeric character for the $5/2^+$ state.

4.3 Experimental details

Two new in-beam γ-ray spectroscopic measurements were performed at JYFL under improved experimental conditions.
The first experiment carried out after the commissioning of JUROGAM in 2003 was a new in-beam γ-ray spectroscopic study of ^{254}No. The GREAT focal plane setup was not yet completed and was operated without the PLANAR and CLOVER detector. A superclover on loan from GSI was placed behind the focal plane vacuum chamber but no useful data could be extracted from this. The PIN diodes had a gain range suitable for detecting escaping α's.
The ^{208}Pb(^{48}Ca,2n)^{254}No reaction was used and the beam energy was in first instance chosen to be at maximal cross section (219 MeV). In the end of the experiment a slightly higher beam energy (221 MeV) was used to try and populate higher spin states.
The stationary targets were situated in the helium filling gas of RITU and could withstand the beam intensities of up to 30 pnA used in the experiment. The maximum beam intensity was limited by the maximum counting rate of the individual germanium detectors ($\sim$ 10 kHz).

In January 2005 a spectroscopic measurement of ^{253}No was carried out with the complete GREAT spectrometer at the focal plane. This time the ^{207}Pb(^{48}Ca,2n)^{253}No reaction was used at maximal cross section. The PIN diodes were set up to measure conversion electrons.
Details of both experiments can be found in table 4.1.

Table 4.1: Some details from the ^{254}No and ^{253}No experiments.

	^{254}No	^{253}No
Beam material	$^{48}Ca^{10+}$	$^{48}Ca^{10+}$
Beam energy	219 MeV, 221 MeV	219 MeV
Excitation energy compound nucleus	22.5 MeV, 24.0 MeV	22.6 MeV
Average beam intensity	16 pnA, 26 pnA	18 pnA
time beam on target	116 h, 42 h	240 h
target material	^{208}Pb	^{207}Pb
target thickness	500 μg/cm^2	610 μg/cm^2
number of recoils detected	54398	82174
number of tagged No α's	11844	9296
half-life (gs)	55 s	1.7 m
α-decay energy	8.09 MeV	8.01, 8.04, 8.06 MeV

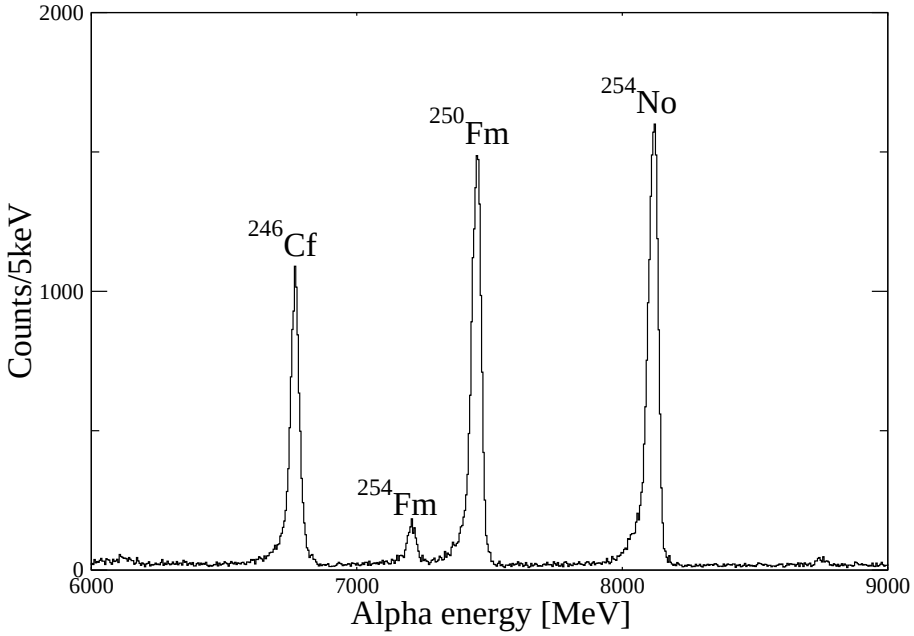

Figure 4.9: Alpha spectrum (vetoed with MWPC) of ^{254}No, the α-decay daughter ^{250}Fm and granddaughter ^{246}Cf and the EC granddaughter ^{254}Fm.

4.4 In-beam γ-ray spectroscopy of ^{254}No

The total α-particle energy spectrum is shown in figure 4.9. About $15 - 20$ % of the ground-state α decays of ^{254}No are expected to feed the first excited 2^+ level at approximately 45 keV in ^{250}Fm. However, the energy of the α particle and the subsequent conversion electron are summed up in the DSSSD detector and only one α peak is seen. Also daughter and granddaughter products are observed.

Approximately 54400 recoil events were selected and the associated prompt γ rays detected in JUROGAM are displayed in the recoil-gated γ-ray singles spectrum shown in figure 4.10(a), which is discussed below. The data taken at the higher beam energy (221 MeV) (displayed in figure 4.10(c)) did not show a significant enhancement in the population of the higher spin states and contained relatively low statistics, thus the data displayed are always for both beam energies combined. Also shown for completeness in figure 4.10(b) is the γ-ray singles spectrum obtained using the RDT technique. The spectrum was obtained by selecting only those recoils which were followed by an 8.09 MeV ^{254}No α decay in the same pixel of the DSSSD within a search time of

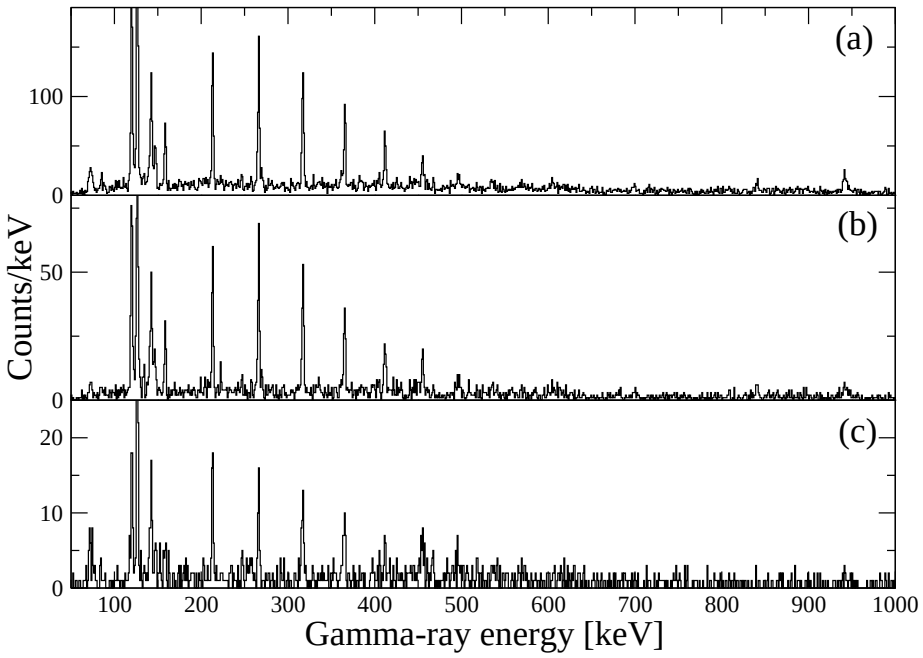

Figure 4.10: Gamma-ray singles spectra of ^{254}No with data of both beam energies combined: (a) Recoil-gated γ-ray singles spectrum (b) No-α tagged γ-ray singles spectrum (c) The recoil-gated γ-ray singles spectrum for higher beam energy only.

180 seconds. A total of approximately 12000 correlated recoil-α pairs were found.

4.4.1 Rotational band

The regular sequence of peaks seen in figure 4.10 are assumed to form an yrast rotational band of stretched $E2$ transitions built upon the ground state of ^{254}No. The earlier assignments of these transitions to the ground-state band of ^{254}No (up to a spin of $20\hbar$) [Rei99, Lei99, Rei00] could be confirmed and the transitions are marked in figure 4.11. The spin assignments are based on the VMI method (equation 2.22). Due to the low level of statistics, angular correlations or distributions could not be performed to confirm the multipolarity of the transitions in this experiment.
The energy of the 20^+ to 18^+ transition was determined to be 498(1) keV, in agreement with the tentative value given in [Rei00]. A clear peak is observed at an energy of 536(1) keV, which is assumed to be the 22^+ to 20^+ transition. This assignment is supported by the recoil-gated γ-γ coincidence data. Example spectra from the recoil-gated γ-γ coincidence data for the ground-state band transitions are shown in figure 4.12 and in the upper two panels of figure 4.13.

Figure 4.12 shows a sum of gated spectra, projected from the recoil-gated γ-γ coin-

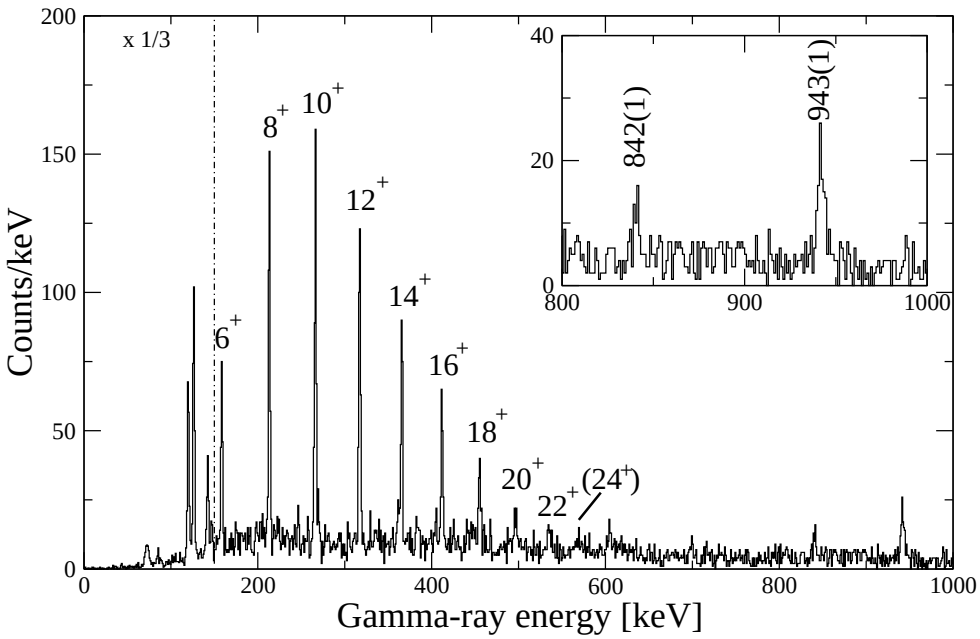

Figure 4.11: Recoil-gated γ-ray singles spectrum of ^{254}No (X-ray region scaled with factor 1/3). The rotational ground-state band transitions are labelled with their respective spin assignments. The inset displays an expansion of the spectrum showing the two prominent high-energy γ-ray peaks.

cidence matrix, with gates on ground-state band transitions from the 6^+ state up to the 18^+ state. The spectrum clearly shows all transitions up to the 22^+ state and the peak at an energy of 570(1) keV is tentatively assigned as the 24^+ to 22^+ transition. If the dynamical moment of inertia continues to behave smoothly (see figure 4.14), the next transition is expected to have an energy around 600 keV. A cluster of counts is observed at this energy in figure 4.12, though inspection of the recoil-gated singles spectrum (figure 4.11) suggests that there is a contribution from some other structure at this energy. This structure is more clearly visible in the α-tagged spectrum in figure 4.10(b). Also of note in the spectrum in figure 4.12 is the sequence of peaks at 397, 440 and 483 keV and one at 335 keV, which could not be placed in the level scheme due to the lack of statistics.

As in the earlier γ-ray spectroscopic studies, the lowest two transitions of the ground-state band were not observed due to strong internal conversion. However, their energies can be extrapolated from a Harris fit to the known members of the band. Such a fit (according to equation 2.21) was performed for the well-established members of the ground-state band and the Harris parameters were determined to be $\mathcal{J}_0 = 68.21\hbar^2/\text{MeV}$ and $\mathcal{J}_1 = 162.22\hbar^4/\text{MeV}^3$ (see figure 4.14). Using those values, equation 2.22 was used to extrapolate to the unknown members of the band. The 4^+ to 2^+ and the 2^+ to 0^+ transition energies were calculated to be 44(1) keV and 102(1) keV respectively. This method was proven to be valid as the energy of the 4^+ to 2^+ tran-

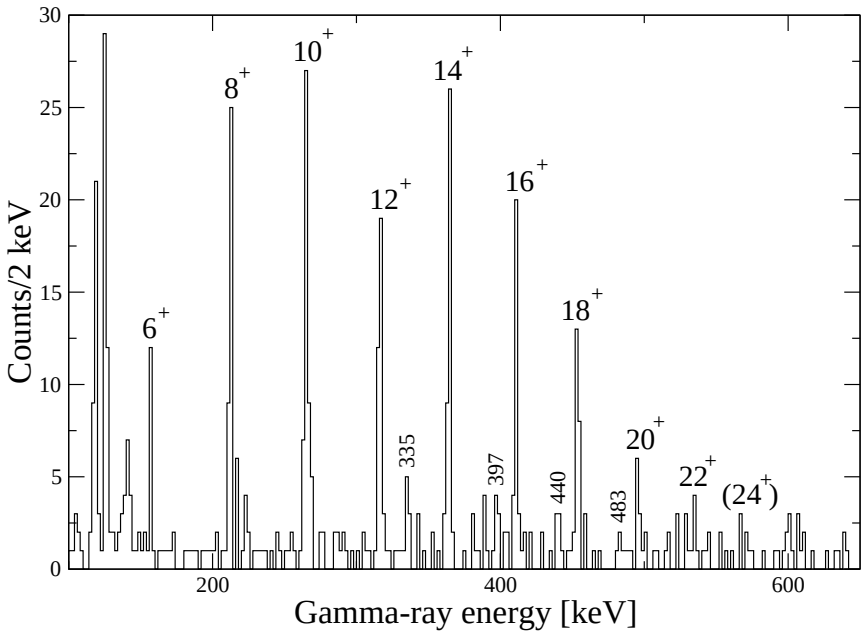

Figure 4.12: A sum of γ-ray spectra projected from the recoil-gated γ-γ coincidence matrix. The sum spectrum includes spectra gated on the ground-state band transitions from the 6^+ state up to the 18^+ state.

sition was measured to be 101(1) keV by conversion electron spectroscopy [Hum04].

The intensities of the ground-state band transitions are plotted in figure 4.15 as a function of spin, corrected for detection efficiency and for internal conversion assuming $E2$ multipolarity. The intensity increases with decreasing spin and levels off at spin $10\hbar$ which confirms the feeding is mainly situated between spin $10 - 20\hbar$ as discussed in section 4.2.1.

4.4.2 High-energy transitions

An interesting feature of the recoil-gated γ-ray singles spectrum is the observation at high energies of two intense transitions at 842(1) keV and 943(1) keV, as shown in figure 4.11. An expansion of the high-energy part of the spectrum is shown in the inset. The intensities of these transitions are 31(8) % and 86(14) % of the 8^+ to 6^+ ground-state band transition, respectively (where all intensities are corrected for γ-ray efficiency only, not for internal conversion). The energy difference of these two γ rays (101(1) keV) corresponds to the energy of the 4^+ to 2^+ transition (101.1(6) keV) measured in the recent conversion-electron spectroscopic study [Hum04]. The γ rays are therefore assumed to originate from a high-lying low-spin state which decays into the 4^+ and 2^+ yrast states as shown in the partial level scheme of figure 4.16. This as-

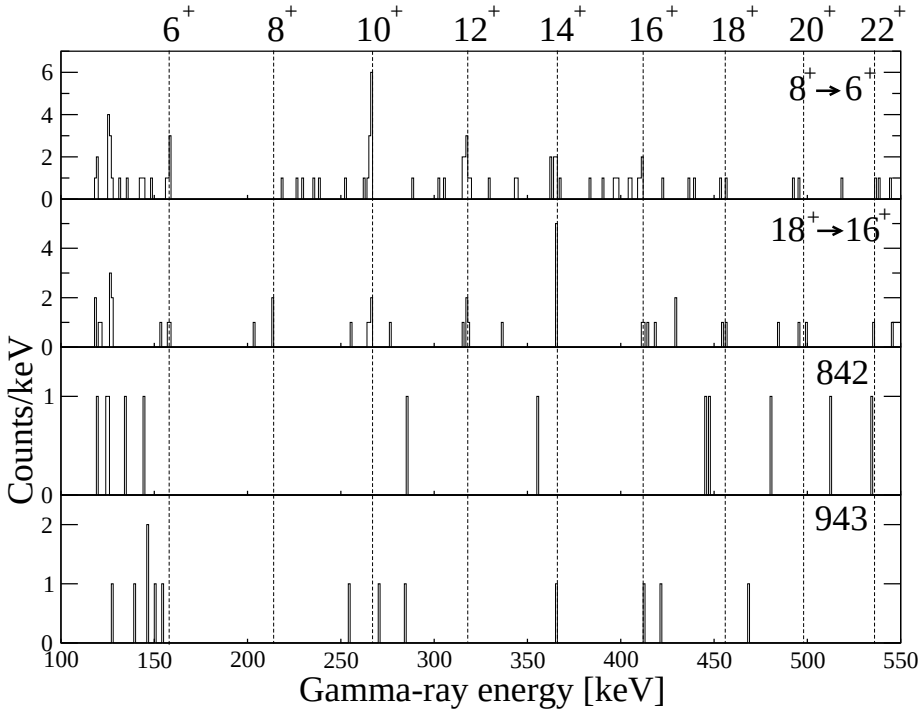

Figure 4.13: Example spectra projected from the recoil-gated γ-γ coincidence matrix. The labels in the upper right-hand corner indicate the transition or transition energy used as a gate. The upper two panels show spectra gated on ground-state band transitions, the lower two spectra gated on the high-energy transitions. Dotted lines indicate the positions of the ground-state band transitions.

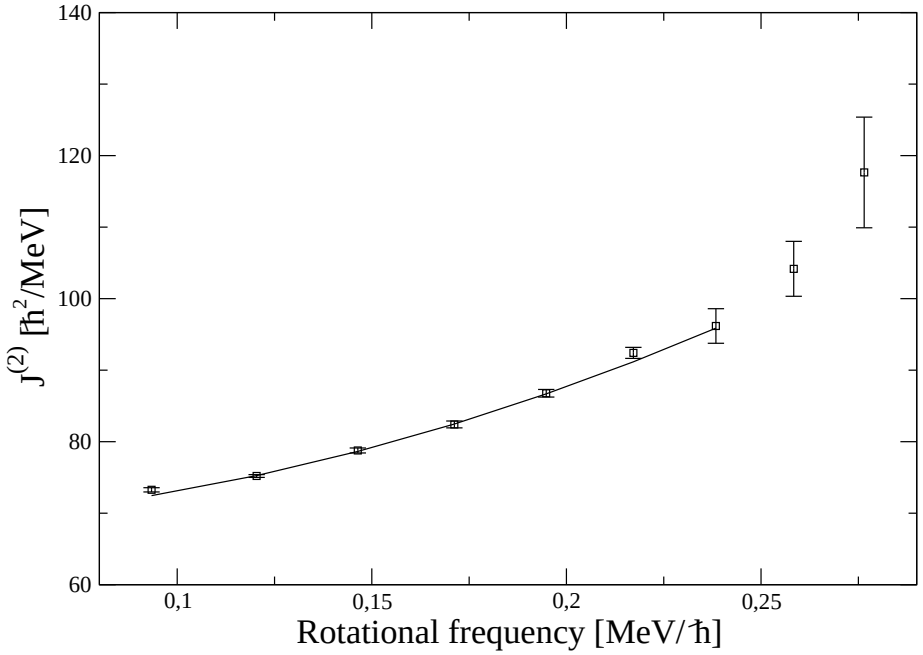

Figure 4.14: Dynamical moment of inertia $\mathcal{J}^{(2)}$ against rotational frequency of the ground-state band of ^{254}No. The solid line represents the Harris fit to the well established members of the ground-state band.

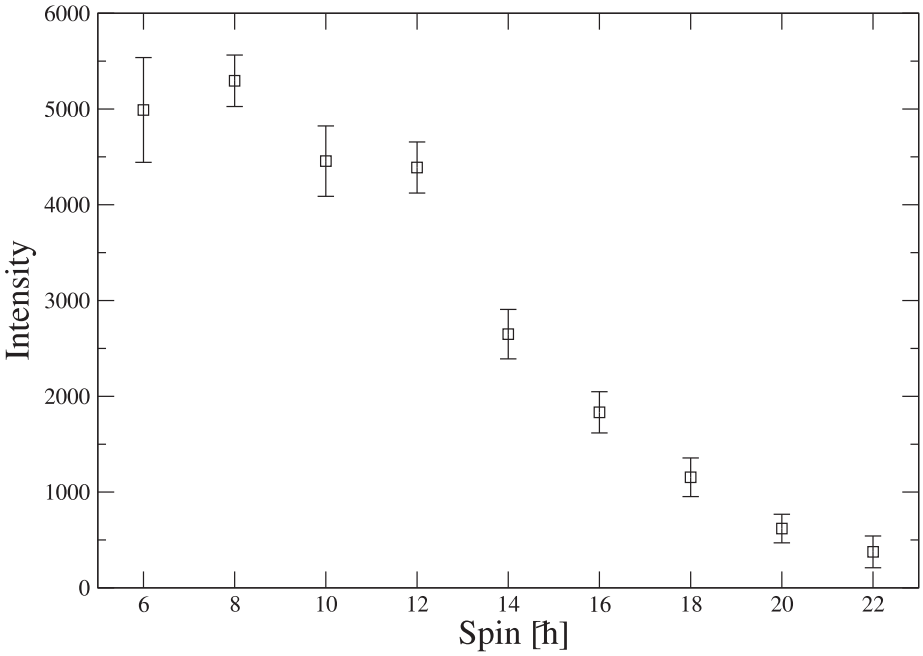

Figure 4.15: Intensity of the ground-state band transitions as a function of the initial spin. The peak areas are corrected for detection efficiency and for internal conversion assuming $E2$ character.

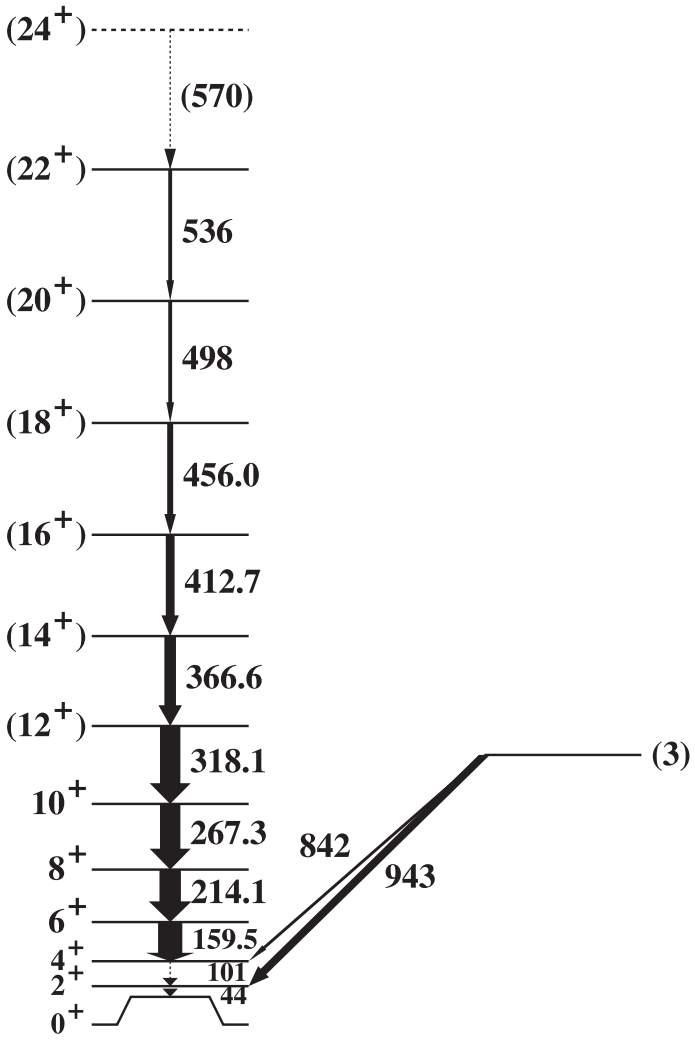

Figure 4.16: Partial level scheme of ^{254}No.

sumption is supported by the absence of clear γ-γ coincidences with ground-state band transitions above the 4^+ state, as illustrated in figure 4.13 where coincidence spectra gated on both the high energy lines and sample ground-state band transitions are shown. Although the 18^+ to 16^+ ground-state band transition and the 943 keV transition have comparable areas in the recoil-gated γ-ray singles spectrum of figure 4.11, they show a large difference in the number of coincidences with the ground-state band transitions above a spin of 4^+. The positions of the ground-state band transition energies are marked with vertical dotted lines in figure 4.13. The second panel of figure 4.13 shows the coincidence spectrum obtained by gating on the 18^+ to 16^+ transition, where coincidences with the ground-state transitions can clearly be seen. The coincidence spectra gated on the 842 keV and 943 keV transitions (shown in the lower two panels of figure 4.13) do not show such a clear correlation.

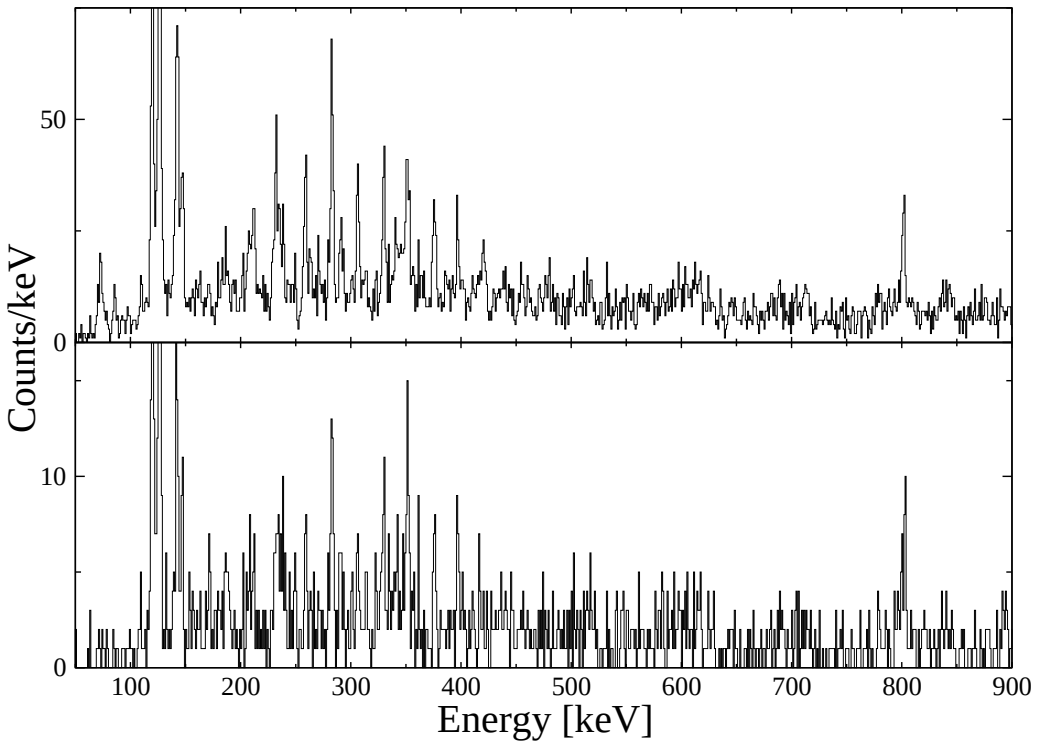

Figure 4.17: Recoil-gated (upper panel) and α-tagged (lower panel) γ-ray singles spectra of ^{253}No.

4.5 Spectroscopic study of ^{253}No

During the study of ^{253}No interesting results were obtained both at the target and the focal plane of RITU. Prompt γ-ray spectroscopy, decay and isomer spectroscopy could be performed during the same experiment.

4.5.1 Prompt γ-ray spectroscopy

The recoil-gated and α-tagged γ-ray singles spectra of ^{253}No are shown in figure 4.17. A total of 82174 recoils were selected and, within a search time of 6 minutes, 9300 recoils could be correlated to a ^{253}No α decay in the same pixel. Both spectra show the same structures confirming the predominant production of the 2n evaporation channel ^{253}No. The total intensity in an odd-mass nucleus is distributed over many different bands, where the unresolved bands contribute to the background level, making the latter higher than in ^{254}No (see figure 4.10).

In odd-mass nuclei, rotational bands are built on single-particle states with half-integer

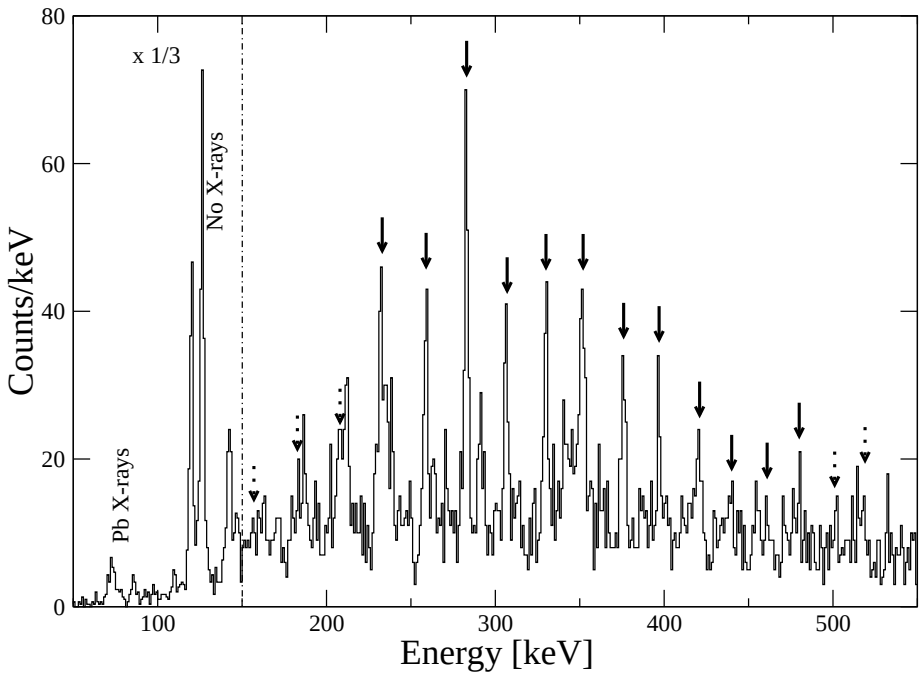

Figure 4.18: Expansion of recoil-gated γ-ray singles spectrum with band members indicated by arrows. (X-ray region rescaled by factor 1/3).

K-values and in the strong coupling limit two signature partner bands are expected. The main peaks visible in the spectrum of figure 4.17 and more detailed in figure 4.18 are assumed to be stretched $E2$ transitions belonging alternately to the positive and negative signature partner of a strongly coupled band. Although the tentative spin assignment will be discussed further, for the purpose of clarity the transitions are already grouped according to signature:

$$\alpha = +\frac{1}{2}: \quad (157), (208), 259, 307, 352, 397, 440, 480, (519) \text{ keV} \tag{4.1}$$

$$\alpha = -\frac{1}{2}: \quad (184), 233, 283, 330, 376, 421, 461, (501) \text{ keV}. \tag{4.2}$$

The energies in brackets are tentative extensions to lower and higher energies. Errors amount to ± 1 keV for the most intense transitions and ± 2 keV for the tentative ones.

The cascade nature of these transitions is supported by γ-γ coincidence data. In figure 4.19 the sum of the γ-ray spectra projected from the γ-γ coincidence matrix gated on the transitions of each signature partner separately as well as on both signature partners combined are shown. From figure 4.19 the tentative extensions to lower and higher energy are visible. They are based on the coincidence data and to a lesser extent on the assumption of a regular continuation of the rotational band structure. At low

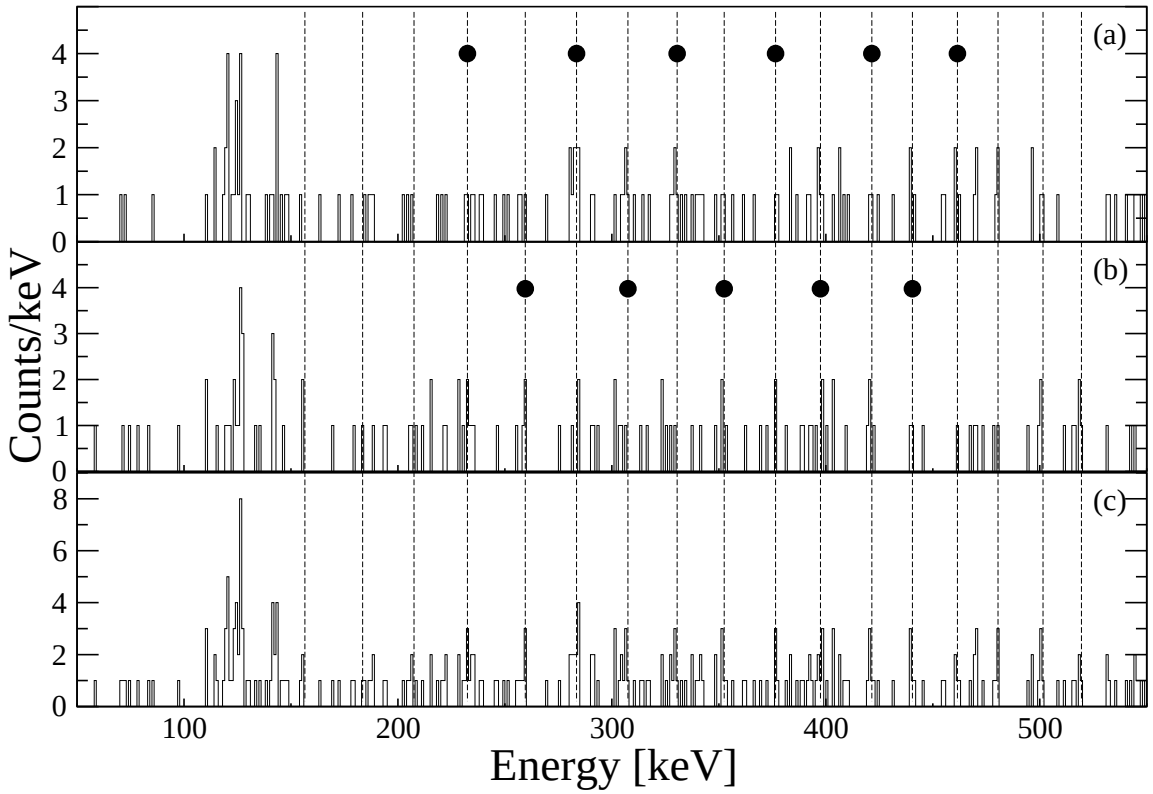

Figure 4.19: Sum of γ-ray spectra projected from the γ-γ coincidence matrix with spectra gated on band transitions of both signature partners separately (panel (a) negative signature and panel (b) positive signature, gated transitions marked with dot) and the sum of both in panel (c). The positions of the band transitions are marked with dashed lines.

energy the assignment is not straightforward and stressed to be very tentative. Note that at lower energy in figure 4.18 several peaks lie within a few keV of the stated transition energies and the coincidence statistics are very low.

To assign spin values to the transitions mentioned above, three different approaches were used.
The first method was based on equation 2.15 and a least χ^2 fit to the transition energies was performed with I and K as variable parameters. The obtained tentative spin assignments are shown in figure 4.21. As the transitions only start to be clearly visible higher up the band and K only introduces a second order effect, the fit is not sensitive enough to K. This is illustrated in figure 4.20 where the evolution of χ^2 with varying I and K is plotted. Whereas χ^2 reaches a clear minimum at a certain spin value, its behaviour is very constant as a function of K.

An extrapolation to the low energy region has been made by fitting equation 2.15 (ignoring the unknown parameter K) to the main visible transitions which resulted in

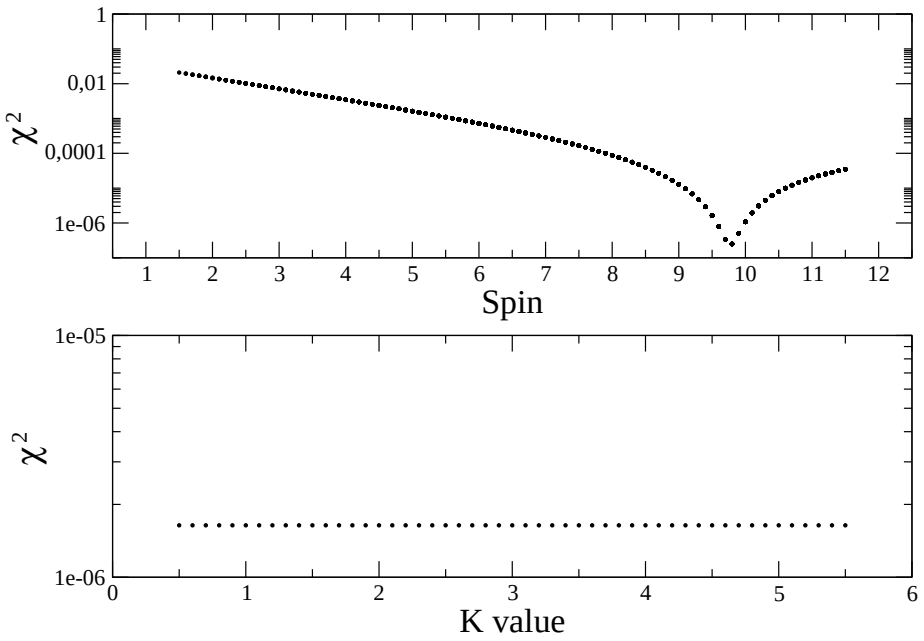

Figure 4.20: Upper panel: the value of χ^2 as a function of the spin of the level that the 233 keV transition originates from. Lower panel: the value of χ^2 as a function of the K value for a fixed spin.

low energy transitions of 132 and 183 keV for the $\alpha = -1/2$ and 157 and 208 keV for the $\alpha = +1/2$ signature band. Even though K was ignored, it would only introduce a second order correction and the values are assumed not to deviate too much from the real value. The calculated transition energies do indeed coincide with suggested candidates for the low energy transitions stated previously.

To check the spin determination, the "ab" formula [Wu92]:

$$E(I) \quad = \quad a(\sqrt{1 + bI(I+1)} - 1) \tag{4.3}$$

was fitted to the experimental transition energies and the parameters a and b were obtained for different spin assumptions. The root mean square (rms) deviation between the calculated values from equation 4.3 and the experimental energies is predicted to show a pronounced minimum at the correct spin assignment [Wu92]. The tentative spin assignment (as shown in figure 4.21) is represented by I_0. The assigned spins of the different levels are then artificially shifted one or two units of $\hbar$ up or down with respect to the I_0 value and the obtained rms deviation for those different spin assumptions is shown in figure 4.22. A clear minimum is obtained for the tentative spin assignment obtained above. The extrapolations to lower and higher transition energies as suggested in the lists 4.1 and 4.2 are reproduced to within 1 keV based on equation 4.3.

Additional support for this spin assignment comes from the study of the variation of

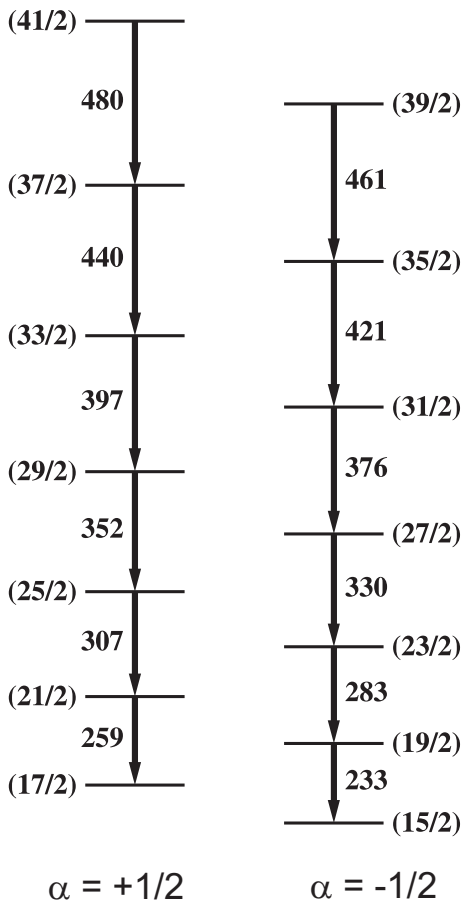

Figure 4.21: Display of the tentative spin assignment of the main visible transitions of two signature partner bands.

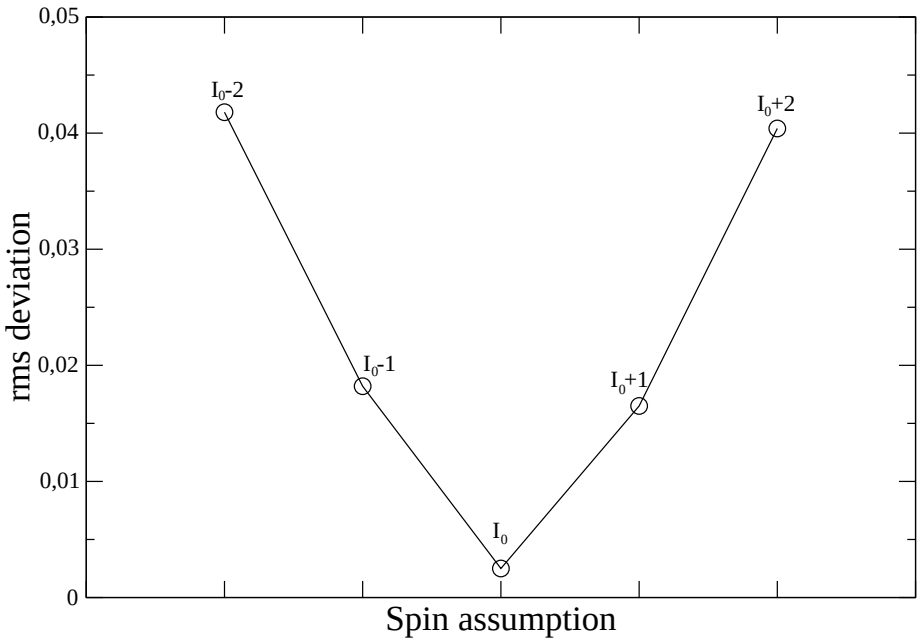

Figure 4.22: Root mean square (rms) deviation between calculated and experimental values based on the "ab" formula for different spin assumptions.

the moments of inertia with the aligned angular momentum of a rotational band [Liu98]. The behaviour of $\mathcal{J}^{(1)}$ as a function of $\xi = \sqrt{I(I+1) - K^2}$ is plotted in figure 4.23 for different spin assumptions together with the spin independent dynamical moment of inertia $\mathcal{J}^{(2)}$. The low energy transitions (157, 184 and 208 keV) are included. The plots shown are for $K = 3.5$ but other K values give similar results. Again the tentative assignment is represented by I_0 and the spins are then increased or decreased by one or more units of $\hbar$. Based on [Liu98] and the fact that the parameter b was found to be positive when fitting equation 4.3, the curves of the two moments of inertia $\mathcal{J}^{(1)}$ and $\mathcal{J}^{(2)}$ should monotonically increase with increasing ξ, be concave upwards and never cross at non-zero spin values. In the limit of $\xi \to 0$ the moments of inertia should converge to the band-head moment of inertia $J_0 = \hbar^2/ab$ and their derivative with respect to ξ should be zero, meaning the curves should be horizontal at low ξ values. From all the plots shown in figure 4.23 only the one with the tentative spin assignment I_0 does exhibit those properties and the band-head moment of inertia $J_0 = 75.36\hbar^2/\text{MeV}$, calculated with the fitted parameters a and b from equation 4.3, does correspond to the convergence point.
Hence all three approaches agree on tentative spin assignment given in figure 4.21. However, all methods are model dependent and only valid if the alignment i_0 is zero and the obtained values actually represent $I - i_0$ [Wu92]. However, I and i_0 can not be extracted separately from the experimental data.

In the high-energy part of figure 4.17 a very intense peak is found at 802(1) keV.

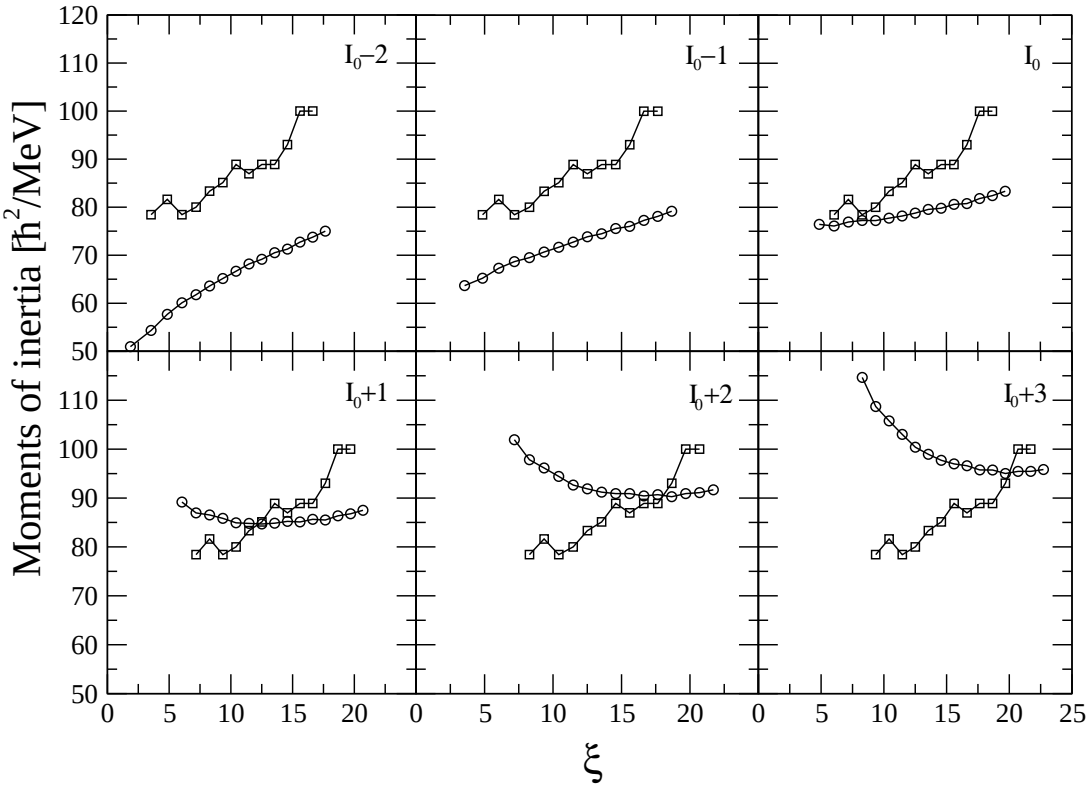

Figure 4.23: The variation of the moments of inertia $\mathcal{J}^{(1)}$ (circles) and $\mathcal{J}^{(2)}$ (squares) with aligned angular momentum $\xi = \sqrt{I(I+1) - K^2}$ for different spin assumptions.

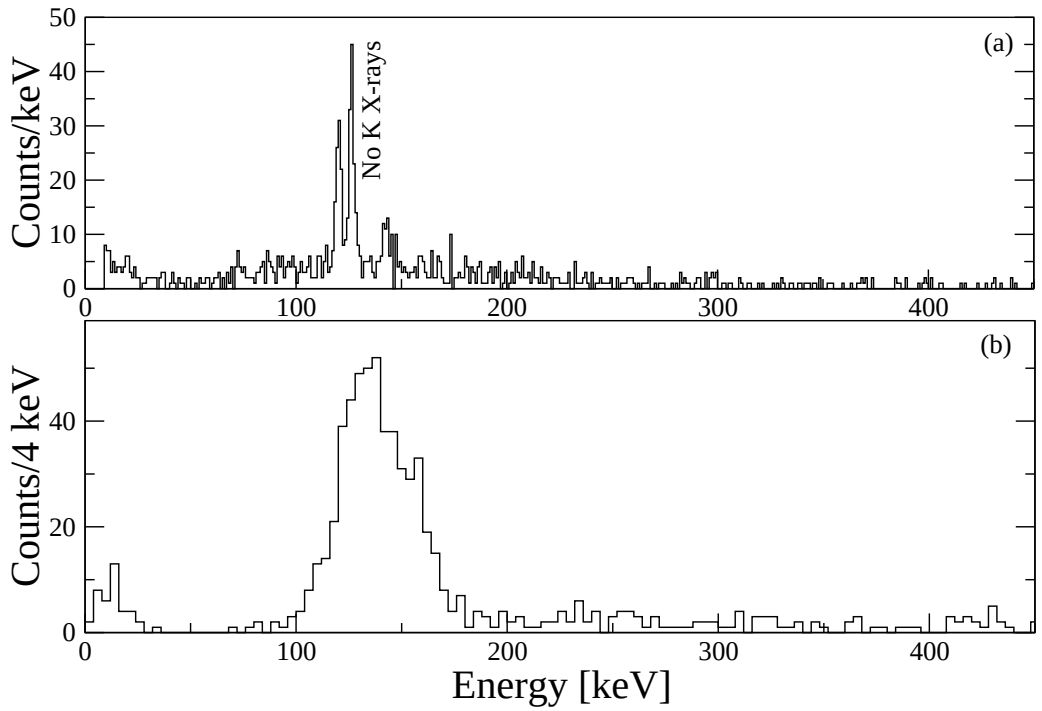

Figure 4.24: Focal plane (a) γ-ray and (b) electron spectra associated with implanted recoils within a 90 μs search time.

This peak is coincident with nobelium K X-rays but no other coincidence with clear structures were found. Several other peaks show up between the main band transitions, indicating the presence of other bandstructures. The level of statistics is however too low to allow further investigation.

4.5.2 Isomer spectroscopy

If a recoil is implanted in an isomeric state, the decay out of the state can be observed in the detectors at the focal plane. In figure 4.24, γ rays and conversion electrons observed within 90 μs after a recoil implantation are displayed.[1] A clear structure is seen around 140 keV in the electron spectrum shown in the lower panel. The counts at very low energy (below 40 keV) in the electron spectrum are solely due to noise. In the γ-ray spectrum only nobelium K X-rays are visible.

The time difference between the electrons in the broad peak at around 140 keV in

[1] To improve the quality of the planar spectrum, only those planar events were accepted for which the horizontal and vertical strip in the detector gave the same energy within a few keV. This way, the background of scattered events was reduced significantly and a rather clean spectrum was obtained.

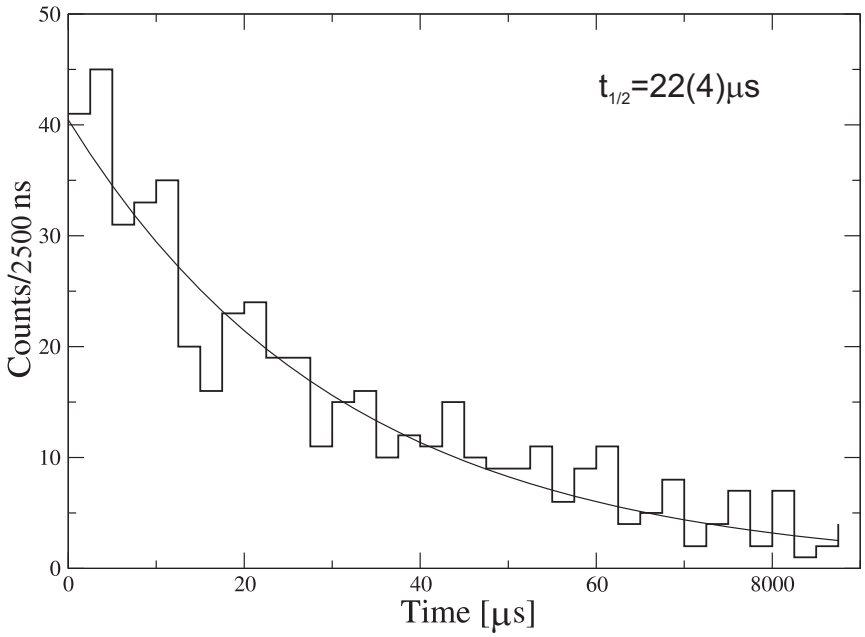

Figure 4.25: Exponential fit of the isomeric half-life from the time difference between recoil implantation and electron decay.

figure 4.24(b) and the associated recoil implantation is plotted in figure 4.25. A fit of the exponential behaviour results in a half-life of 22(4) μs. The nobelium K X-rays show a similar time behaviour and here a half-life of 28(3) μs was deduced. This indicates that they originate from the decay of the same isomeric state.
Prompt γ rays at the target position associated with electron-tagged isomeric recoils at the focal plane are shown in figure 4.26. A few small peaks are visible but no indication of a band structure is present.

4.5.3 Decay spectroscopy

In prompt coincidence with the ^{253}No α decay, electrons and γ rays belonging to the daughter nucleus ^{249}Fm were observed as shown in figure 4.27.[2] Three distinct γ-ray transitions with energies of 151, 221 and 279 keV show up along with associated conversion electrons (L+M electrons for all three transitions and also K electrons for the 279 keV transition). No γ-γ coincidences between the observed transitions were found.
As the recoil is implanted into the DSSSD detector, radiation source and detector are not separated. Hence emission of conversion electrons subsequent to the α decay leads to the detection of their sum energy [Hes89]. This is illustrated in figure 4.28

[2] Idem previous footnote.

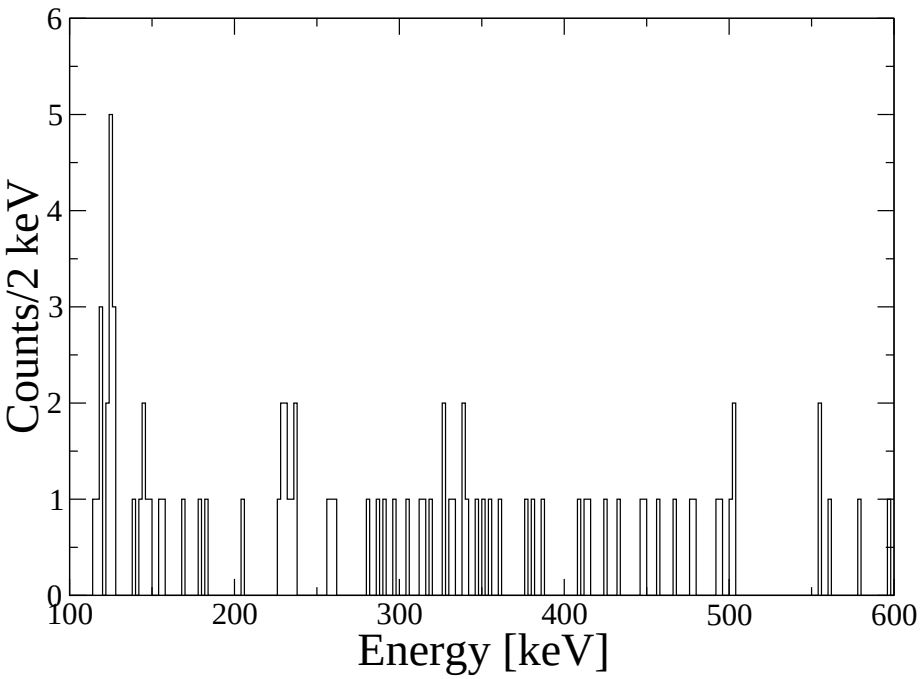

Figure 4.26: Isomer tagged γ-ray singles spectrum of ^{253}No.

where the γ-ray energy is plotted against observed α energy. While the width of the α peak in coincidence with the 279 keV transition is comparable with a ground-state to ground-state transition, the coincidence α peaks for the 221 and 151 keV γ rays seem to have a contribution from electron coincidence summing. Note also that although the linewidth of the α decays in coincidence with the three γ rays is different in the α-γ matrix, the minimum energy is the same for each suggesting that in all three cases the α decay populates the same state in ^{249}Fm.

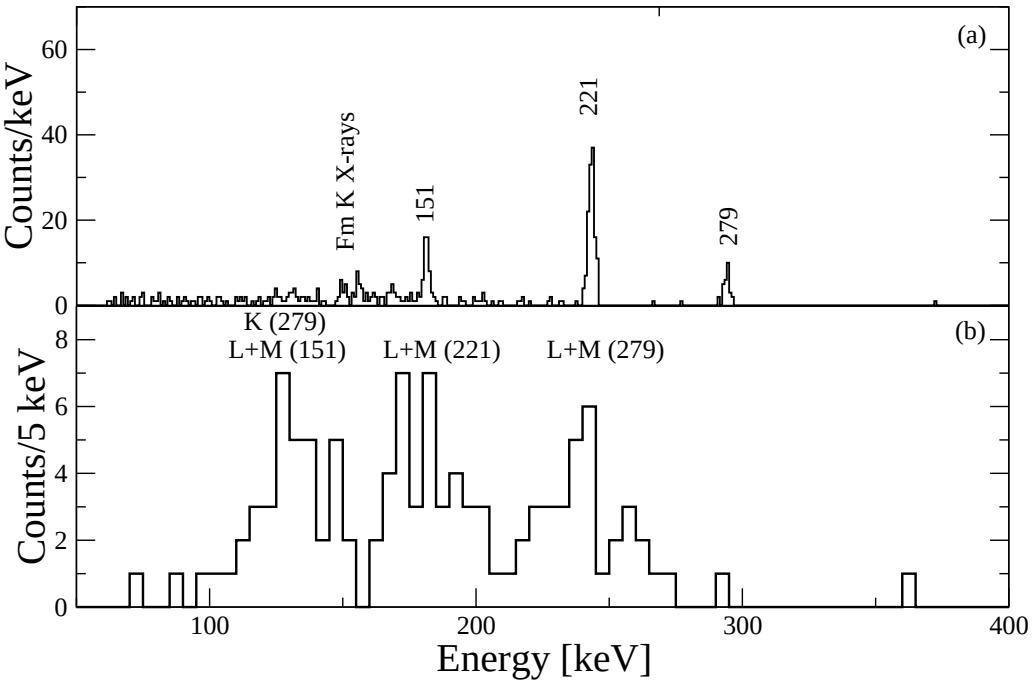

Figure 4.27: The α-decay gated focal plane decay spectra of (a) γ rays in the planar detector and (b) electrons in the PIN diodes.

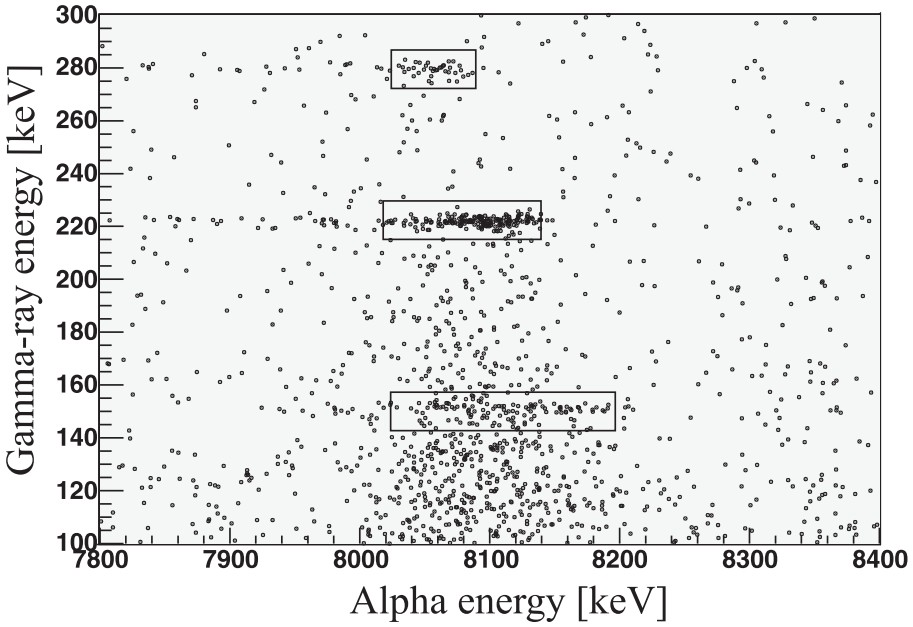

Figure 4.28: Plot of γ-ray energy versus α energy. The boxes indicate coincidences of the three peaks shown in figure 4.27.

5 Discussion

Based on the recent experiments with JUROGAM-RITU-GREAT*, information about the transfermium nuclei ^{254}No and ^{253}No could be deduced.*
The ground-state rotational band of ^{254}No was confirmed and extended up to spin $22\hbar$ and a rotational structure was observed in ^{253}No.
After the assignment of a band-head configuration to the rotational band structure in ^{253}No, the rotational properties of various transfermium elements are discussed.
In both nuclei hints for non-yrast structures were observed in the form of high-energy γ-ray transitions. Interpretation of the origin of those transitions will be addressed in this chapter and supported by more recent experimental results. Furthermore the interpretation of the isomeric structure in ^{253}No as well as the level structure in ^{249}Fm deduced from decay spectroscopy will be given.
The chapter will be concluded with a summary of the experimental and theoretical findings and a look into the future prospects of the study of transfermium nuclei.

5.1 Rotational properties

A rotational band structure has been observed in ^{254}No and ^{253}No as shown in chapter 4. While in the even-even nucleus ^{254}No the assignment of the structure to the 0^+ ground state was straightforward, in ^{253}No the character of the band-head the rotational structure is based on is not that evident and will be discussed in this section. To summarise, the rotational properties are compared with other transfermium nuclei and theoretical predictions based on the dynamical moment of inertia.

5.1.1 Interpretation of the rotational band in ^{253}No

In heavy-ion induced fusion-evaporation reactions mainly the yrast states of the final nucleus are populated. However, when producing very heavy elements, only a limited amount of angular momentum is brought into the system, enhancing the population of the non-yrast states at lower spin values. Specific theoretical calculations or experimental values estimating the level of non-yrast population are however not available. With this in mind, the band shown in figure 4.21 can in principle be built upon any of the low-lying states predicted by theoretical calculations (see section 4.2.2). The

g_K values of the lowest lying single-particle states were calculated based on the model in [Cwi94] and following values were obtained: -0.25 ($9/2^-[734]$), $+0.28$ ($7/2^+[624]$), -0.41 ($5/2^+[622]$) and -1.70 ($1/2^+[620]$). Non-yrast structures with dominant $M1$ transitions will have a very low probability to be observed via in-beam γ-ray spectroscopy. Therefore, excluding excited states with dominant $M1$ transitions, the observed band is expected to be built either upon the $9/2^-[734]$ ground state of ^{253}No, or upon the only low-lying excited single-particle state with positive g_K value, the $7/2^+[624]$ state. The transition energies of the bands built on these states are expected to be very similar and hence the two bands are not easily distinguishable. Also, the procedures used for the spin assignment of the different transitions were not sensitive enough to the K value of the band to decide on $K = 9/2$ or $K = 7/2$ (see section 4.5.1).

If the main visible band belongs to the excited $7/2^+[624]$ state, $E1$ transitions out of this band to the assumed $9/2^-[734]$ ground-state band should be clearly distinguishable in both singles and coincidence spectra (see figure 4.18 and 4.19). The 290, 342, 402 and 472 keV peaks present in the singles and coincidence spectra around the theoretically predicted energy of $\sim$ 300 keV for the $7/2^+[624]$ band-head might be candidates. None of these candidates are intens enough, however, to be $E1$ transitions depopulating the lowest members of the $7/2^+[624]$ band, carrying the intensity of one signature partner.
In the paper by P. Reiter *et al.* [Rei05] the transitions of the broad peak around 355 keV are assumed to be the $E1$ transitions out of the band. As this peak also comprises a member of the band, self-coincidences of this broad peak are expected. However, no such coincidences could be observed in their experiment [Kho06], nor in the data discussed here, although this might be due to the low level of statistics.

In order to aid the interpretation, a simulation of the spectra for the signature partner bands built upon the $9/2^-[734]$ and $7/2^+[624]$ single-particle states was performed. As input, the tentative spins and energies of the $E2$ transitions of a strongly coupled band as seen in figure 4.21 were used, with the extensions to lower transition energies as mentioned in section 4.5.1. Transitions linking the band with mixed $M1$ and non-stretched $E2$ character were added and the relative position between the two signature partners was obtained by fitting the level energies with equation 2.15. The total level scheme used as an input is displayed in figure 5.1, where the lowest level is omitted in the simulation of the $K = 9/2$ band.

Branching ratios were calculated for a $K = 7/2$ band built upon the $7/2^+[624]$ single-neutron orbital with $g_K = +0.28$ and for a $K = 9/2$ band built upon the $9/2^-[734]$ orbital with $g_K = -0.25$. The calculated transition strengths were based on the rotational model of Bohr and Mottelson using the expressions in table 2.1, where the $B(M1)$ and $B(E2)$ values obtained from equations 2.31 and 2.32 were corrected for internal conversion and the parameters Q_0=13.1 eb and $g_R = 0.4$ were used.

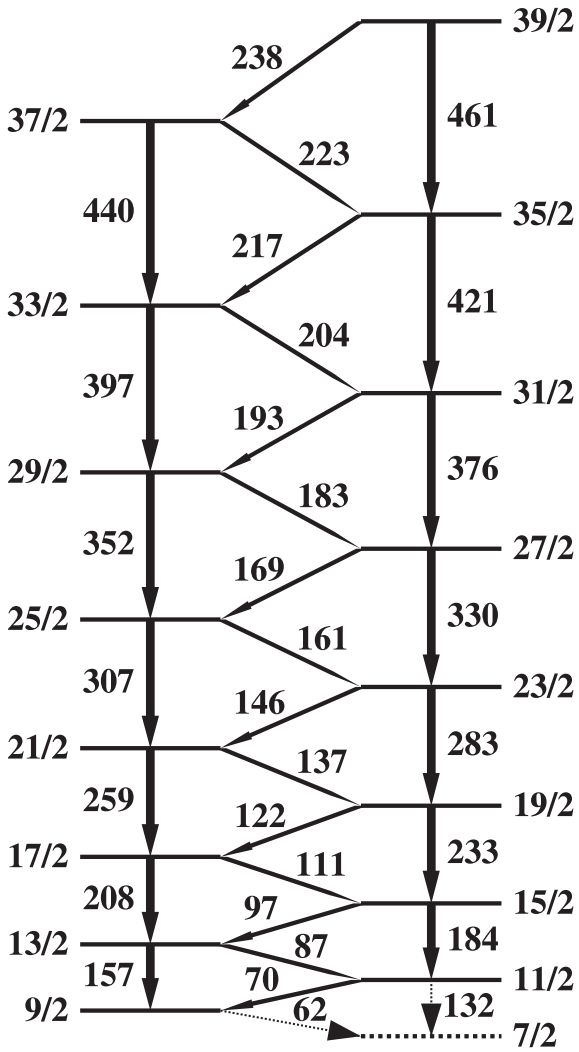

Figure 5.1: Level scheme used as an input for the simulation with $E2$ cascades linked by $M1$ transitions.

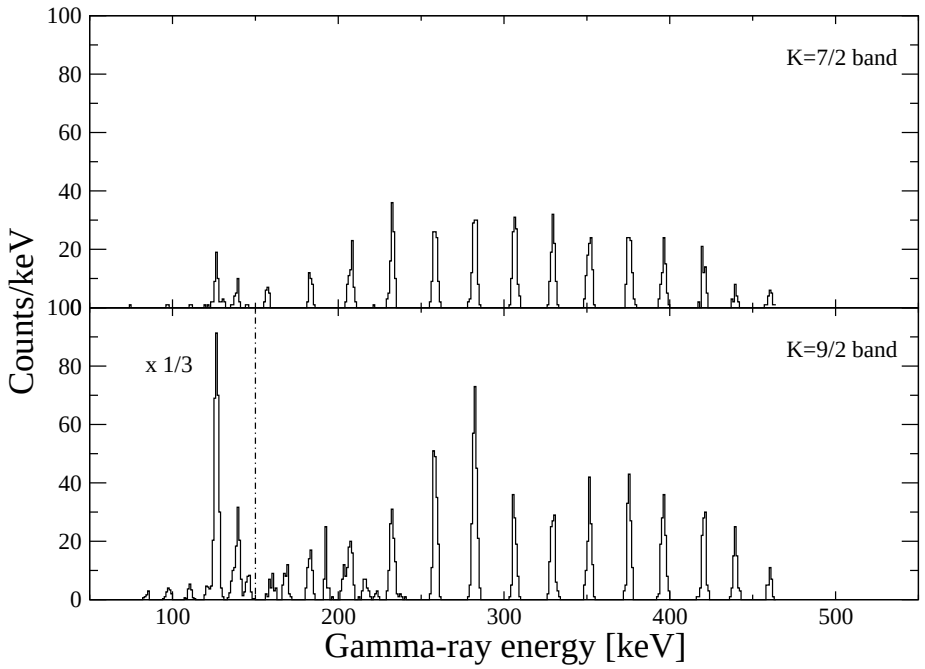

Figure 5.2: Example simulated γ-ray singles spectra for the $K = 7/2$ and $K = 9/2$ band. (X-ray region scaled by factor $1/3$ for $K = 9/2$ band)

The spin dependent population of the states was assumed to be the same as the measured feeding pattern of ^{254}No [Rei00] and the detection efficiency of JUROGAM was taken from figure 3.4. The simulation was repeated 2000 times to remove the dependence on a specific set of random numbers. The total number of events was scaled to match the experimentally observed number of counts in the 307 keV peak in the γ-ray singles spectrum. The K_α and K_β X-rays were grouped at 127 and 140 keV in the simulated spectra respectively to make any underlying structure more visible. Both singles and coincidence data were simulated and example spectra from one simulation are shown in figures 5.2, 5.3 and 5.4 and some quantities, averaged over the 2000 simulations, are summarised in table 5.1.

Table 5.1: Summary of experimental and simulated values. (simulation repeated 2000 times)

	experimental	$K = 7/2$ band	$K = 9/2$ band
single No K X-rays	1213	64	1060
single area 146 keV peak	$\sim$42	2	73
single area 111 keV peak	$\sim$21	2	43
straight/cross coincidences	1.06	11.1	1.8
number of events at target		6300	22000

To create the simulated singles spectra, a different total number of events at the target

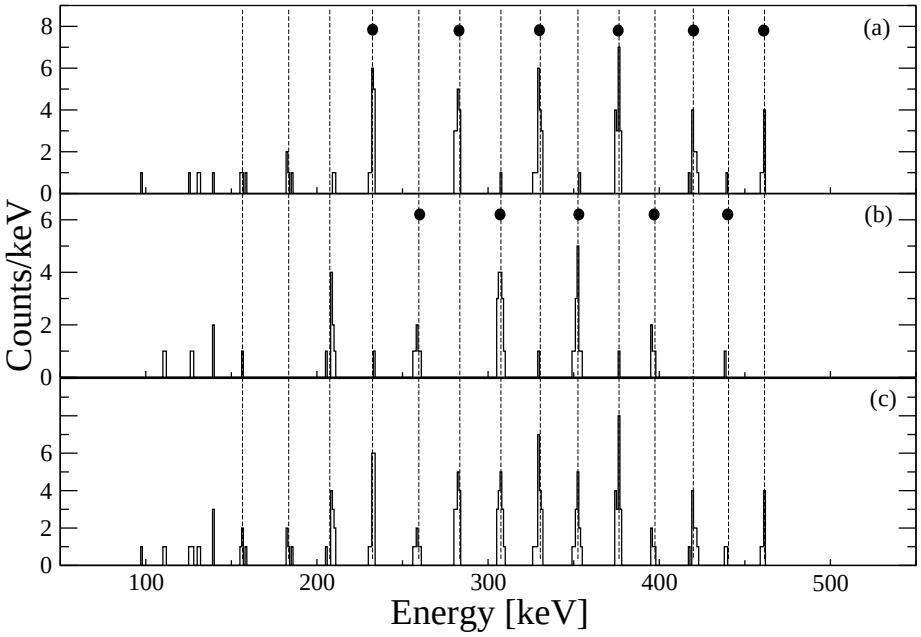

Figure 5.3: Example simulated coincidence data for the $K = 7/2$ band. Sum of coincidence spectra gated on band transitions of both signature partners separately (panel (a) negative signature and panel (b) positive signature, gated transitions marked with dot) and the sum of both in panel (c). The positions of the $E2$ band transitions are marked with dotted lines.

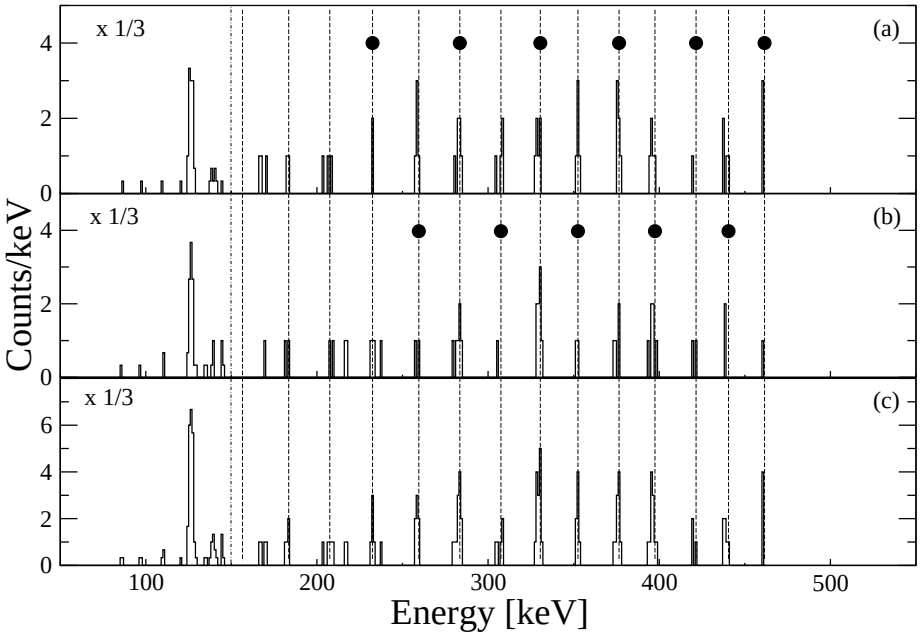

Figure 5.4: Idem to figure 5.3 for $K = 9/2$ band. (X-ray region scaled with factor $1/3$)

was assumed for the different configurations to match the 307 keV transition strength. The total number of events used as an input is shown in table 5.1 and from this it can be seen that the $K = 9/2$ band has to be fed 3.5 times as much as the $K = 7/2$ band to be equally well visible. The $K = 9/2$ band is assumed to be yrast and the $K = 7/2$ band is expected to lie about 300 keV higher according to calculations shown in figure 4.6.
Cranking calculations were performed using the cranking code from [Pau99] for the single-particle neutron states with a Woods-Saxon potential. The deformation parameters were taken from Cwiok *et al.* [Cwi94] and the calculated quasi-neutron levels are shown in figure 5.5. The $9/2^-$ level is closest to the Fermi surface, which is situated at $e' = 0.57$ MeV for zero rotation, the next level being a $7/2^+$ state. These cranking calculations show that the ground-state $9/2^-$ band does not cross any higher lying positive parity band in the region where the main feeding is situated, i.e. below a transition energy of ~ 500 keV ($\omega \sim 250$ keV).
Hence a rather strong non-yrast feeding has to go to the $K = 7/2$ band to make it more visible than the $K = 9/2$ yrast band. Although, as mentioned before, heavy-ion induced fusion-evaporation reactions usually very much favour the feeding of yrast states, in the reaction used here the entry distribution is situated at low spins and some non-yrast feeding is expected. The extent to which this is so is difficult to know however as there is not enough data available in the region to make careful studies of known population patterns in such reactions possible.

The strength of the stretched $E2$ γ-ray transitions as a function of the position of the transitions in the band is dependent on the configuration. The peak area of the stretched $E2$ transitions as a function of transition energy for experimental and simulated data are plotted in figure 5.6. The experimental data agree better with the results of the $K = 7/2$ band simulation at higher transition energies. However, the behaviour around the 283 keV transition is better reproduced with the $K = 9/2$ band simulation. The simulated data is of course dependent on the feeding pattern used, which is assumed to be identical for the yrast and the non-yrast states. This rather good agreement might therefore be considered more as a confirmation that the chosen feeding pattern is valid than as an argument to support a certain assumption on the band-head configuration.

The experimental γ-ray singles spectrum in figure 4.17 is dominated by nobelium K_α and K_β X-rays. As for the simulated data (see figure 5.2) only the $K = 9/2$ band spectrum has a large number of K X-rays present, originating from converted transitions in the simulated band. When gating on the $E2$ band transitions, only K X-rays in coincidence with the members of the signature partner bands should remain. In the experimental data a reasonable number of K X-rays remain after gating, comparable again to the $K = 9/2$ simulated data of figure 5.4. There are hardly any K X-rays in the $K = 7/2$ simulation of figure 5.3.
One must, however, be careful to draw any definite conclusions from this as the K

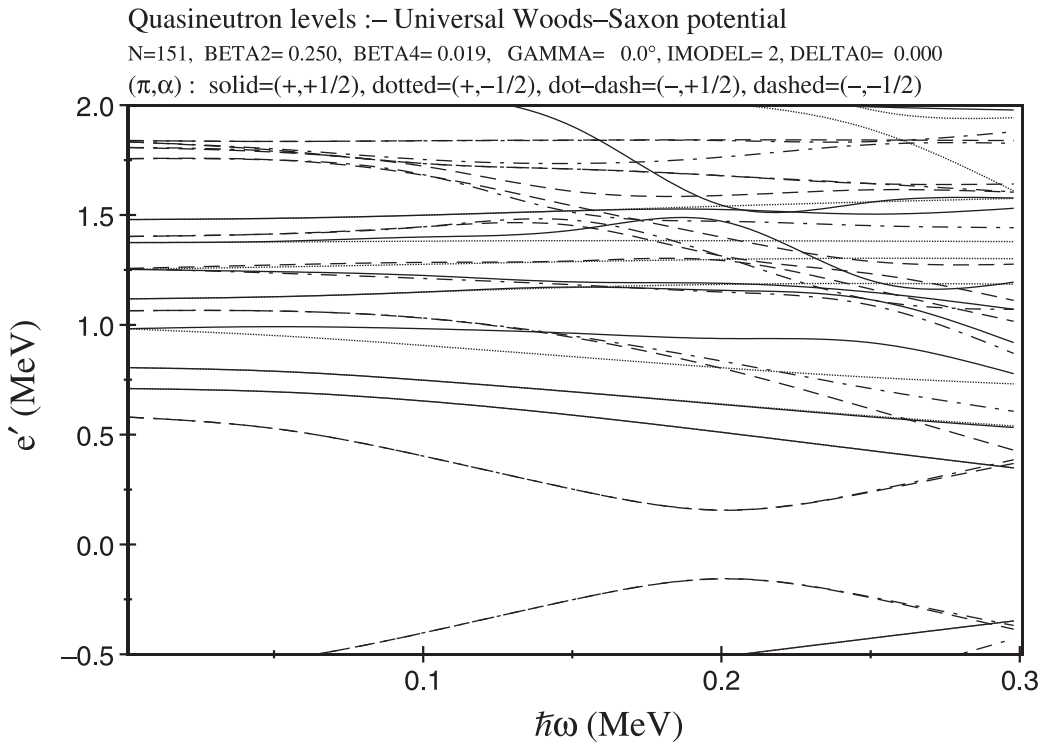

Figure 5.5: Quasi-neutron levels in ^{253}No obtained by cranking calculations.

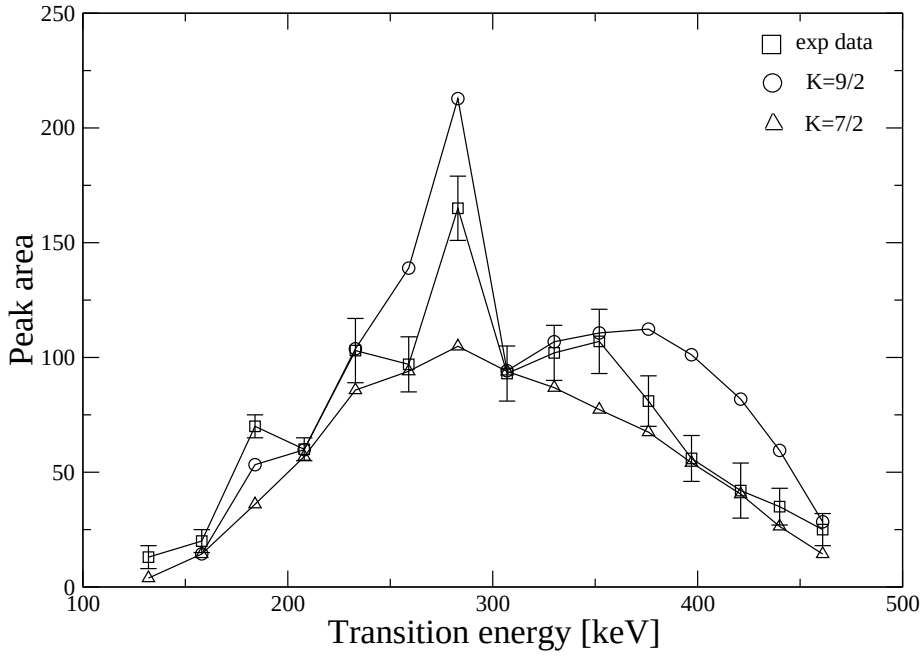

Figure 5.6: Plot of the yield (peak area) in function of transition energy for the experimental data and simulations of $K = 7/2$ and $K = 9/2$ band.

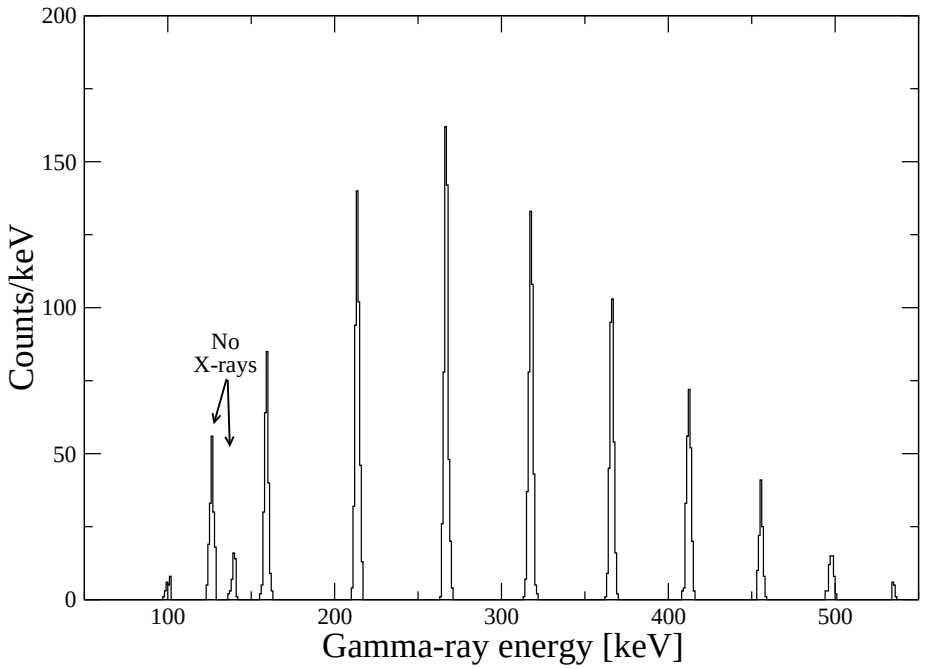

Figure 5.7: Simulated singles γ-ray spectrum for the ground-state band of ^{254}No.

X-rays in the experimental spectrum can originate from other populated structures whose γ-ray transitions are not resolved in the spectrum. In the case of ^{254}No for example, a large number of K X-rays are present in both singles and coincidence data which can for most part not be accounted for by the ground-state rotational band. This can be seen from the simulated singles γ-ray spectrum of the ground-state band in ^{254}No up to spin $22\hbar$ in figure 5.7 and the experimental spectrum in figure 4.11. Hence most of the K X-ray intensity must originate from unresolved higher-lying structures feeding into the ground-state band.

When comparing the experimentally observed intensity ratios of the $K_{\alpha 1,\alpha 2,\alpha 3}$ and $K_{\beta 1,\beta 2,\beta 3}$ X-rays to the theoretical values [Fir96], it was found that about half of the 95 counts in the peak at ~ 147 keV are not $K_{\beta 2}$ X-rays . In the simulated spectra, an $M1$ transition at 146 keV is clearly visible for the $K = 9/2$ band but almost absent for the $K = 7/2$ band (see table 5.1).
Also the other $M1$ transitions are much stronger in the $K = 9/2$ band simulation due to the strong transition strength between the two signature partners in a negative g_K structure. For example, the intensity of the 111 keV $M1$ transition is compared in table 5.1. Also here, the $K = 9/2$ band corresponds rather well to the data while the value obtained for the $K = 7/2$ band is a factor of 10 different to the experimental value.
The low energy region for the simulated and experimental spectra is enlarged in figure 5.8. In the experimental singles data in panel (c), a large number of low energy

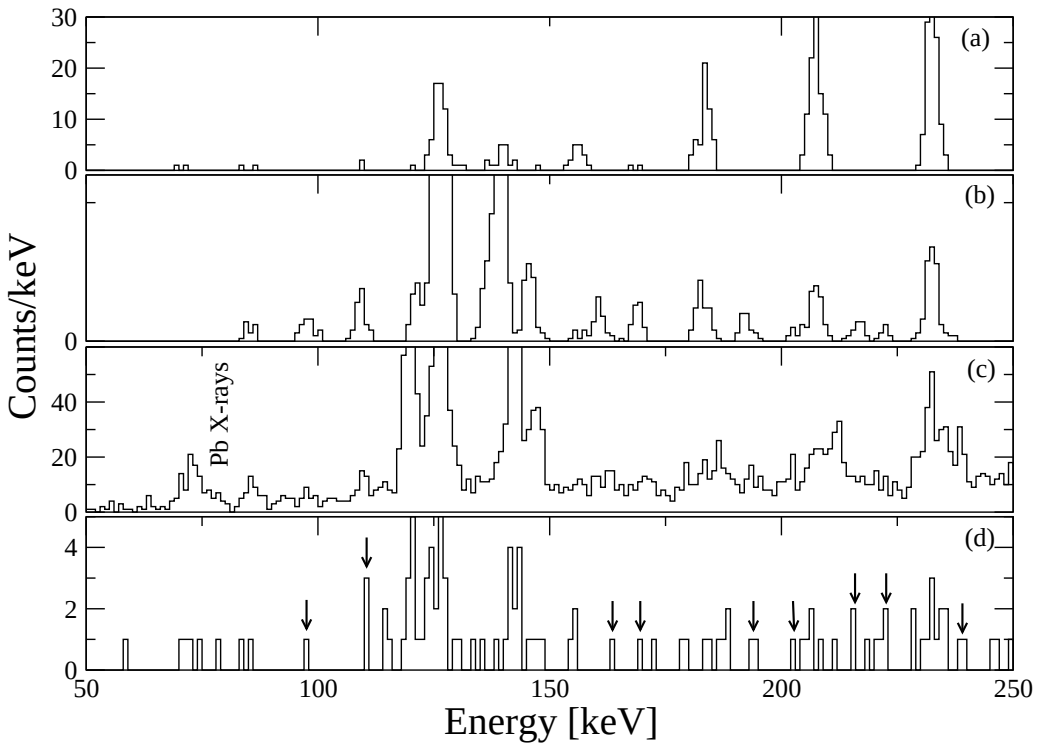

Figure 5.8: Enlargement of low energy part of γ-ray spectra: γ-ray singles spectra for the (a) $K = 7/2$ band simulation and (b) $K = 9/2$ band simulation and experimental (c) singles and (d) coincidence data. In (d) coincidence counts with suggested $M1$ transitions are marked with arrows.

peaks are seen which are good candidates for the interlinking $M1$ transitions. The sum of coincidence gates on both signature partners together is shown for the experimental data in panel (d). Despite the very low statistics, the expected $M1$ transitions are present and marked with arrows (only those $M1$ transitions are marked whose energy does not coincide with the energy of an $E2$ transition or X-ray). The correspondence of the structure in the experimental spectrum and the expected $M1$ transitions in both the experimental singles and coincidence spectra favours the $K = 9/2$ assignment.

From the coincidence data, one can estimate the strength of the $M1$ and non-stretched $E2$ transitions between the two signature partners by looking at the number of coincidences interlinking the two signature partners. For the $K = 9/2$ band a comparable number of coincidences between the two signature partners ('cross coincidences') to coincidences between the transitions of the same signature partner ('straight coincidences') are seen. In the $K = 7/2$ simulation the 'straight coincidences' clearly dominate. Ratios of straight to cross coincidences were taken (shown in table 5.1) and the experimental data shows a low ratio of straight to cross coincidences, clearly favouring the $K = 9/2$ band. The distribution of those ratios for 2000 simulations is shown in figure 5.9. Around the experimental ratio of 1, the simulated distribution of

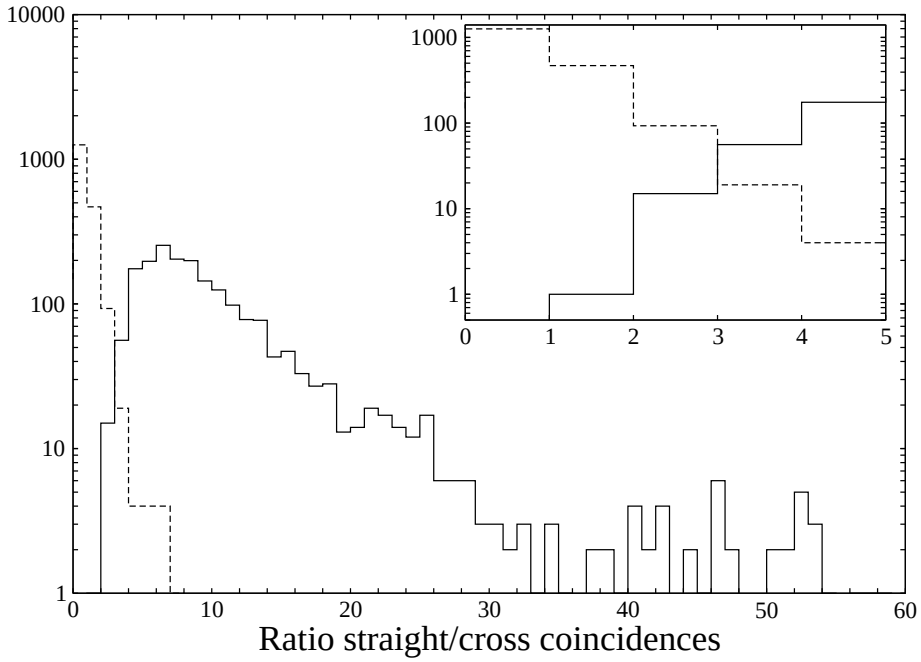

Figure 5.9: Distribution of the ratio of straight to cross coincidences for the simulated $K = 7/2$ (solid line) and $K = 9/2$ (dashed line) band with the region of low values of the ratio expanded in the inset.

the $K = 9/2$ band clearly dominates the simulated $K = 7/2$ band distribution. Hence, although coincidence statistics are very low, on the basis of the γ-γ coincidence data the $K = 9/2$ assignment seems very probable.

A strong final argument is based on the comparison of the γ-ray intensity ratio of mixed $M1$ and non-stretched $E2$ transitions (denoted $E2$') connecting the two signature partners to the stretched $E2$ transitions within the same signature partner. These values can be obtained from the experimental data by taking the efficiency corrected ratio of the areas of the different peaks. The theoretical γ-ray transition strengths were again based on the rotational model of Bohr and Mottelson using the $B(M1)$ and $B(E2)$ values obtained from equations 2.31 and 2.32 with Q_0=13.1 eb and $g_R = 0.4$ and the expressions in table 2.1. The calculated total γ-ray transition probabilities for $K = 7/2$ and $K = 9/2$ are plotted in figure 5.10 as a function of the spin of the de-exciting state. The experimental data points are in very good agreement with the theoretical values of the $K = 9/2$ band and almost an order of magnitude different from the $K = 7/2$ theoretical values.
Moreover, the experimental g_K factor could be calculated based on the ratio of equations 2.31 and 2.32. For $K = 9/2$ the average solutions for g_K were 1.04(5) and $-0.24(5)$ and for $K = 7/2$ the values for g_K were calculated to be 1.23(14) and $-0.43(14)$. The negative solution $g_K = -0.24(5)$ corresponds very well to the theo-

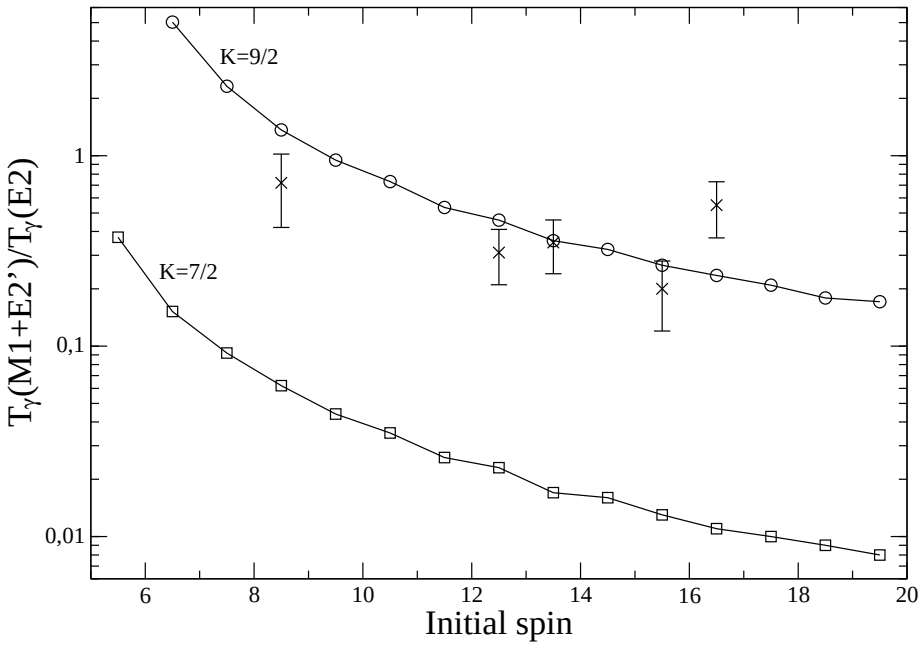

Figure 5.10: The ratio of the calculated total γ-ray transition probabilities T_γ of mixed $M1$ and non-stretched $E2$ ($E2$') transitions to stretched $E2$ transitions as a function of the spin of the initial state for the $K = 7/2$ (squares) and $K = 9/2$ (circles) configurations. The experimental total γ-ray transition probabilities (crosses) are shown with error bars.

retical value for the $K = 9/2$ band which is $g_K = -0.25$. In the $K = 7/2$ case, the g_K values are far from the theoretical values of the $K = 7/2$ band ($g_K = +0.28$).
Hence, both the value of g_K and the γ-ray transition probabilities extracted from the experimental data agree very well with the theoretical values for the $K = 9/2$ band.

Most of the arguments presented above were based on models and assumptions and often a low level of statistics. Therefore no definite assignment can be made. But nevertheless almost all arguments point towards the observation of a band based on the $9/2^-[734]$ single-particle state, making this the tentative assignment here. As the $K = 9/2$ assignment is in disagreement with the $K = 7/2$ assignment made by Reiter *et al.* [Rei05], further experiments might be necessary to draw any firm conclusions.

The $9/2^-[734]$ state, originating from the $1j15/2$ orbital, has relatively large j and small Ω and hence some Coriolis alignment is expected to occur. Although the alignment i_0 can not be extracted directly from the experimental data, predictions can be made based on systematics. The rotational parameter $A = \frac{\hbar^2}{2\mathcal{J}^{(0)}}$ (see equation 2.13) is assumed to stay constant within an isotonic chain provided no structural changes occur. To obtain a value of A close to the values of the isotones ^{247}Cm ($A = 5.6$) and ^{249}Cf ($A = 5.7$) fitted using equation 2.13 [nndc] the spin values I_0 obtained in section 4.5 have to be increased by $1\hbar$, giving $A \sim 5.8$. Hence the systematics of the

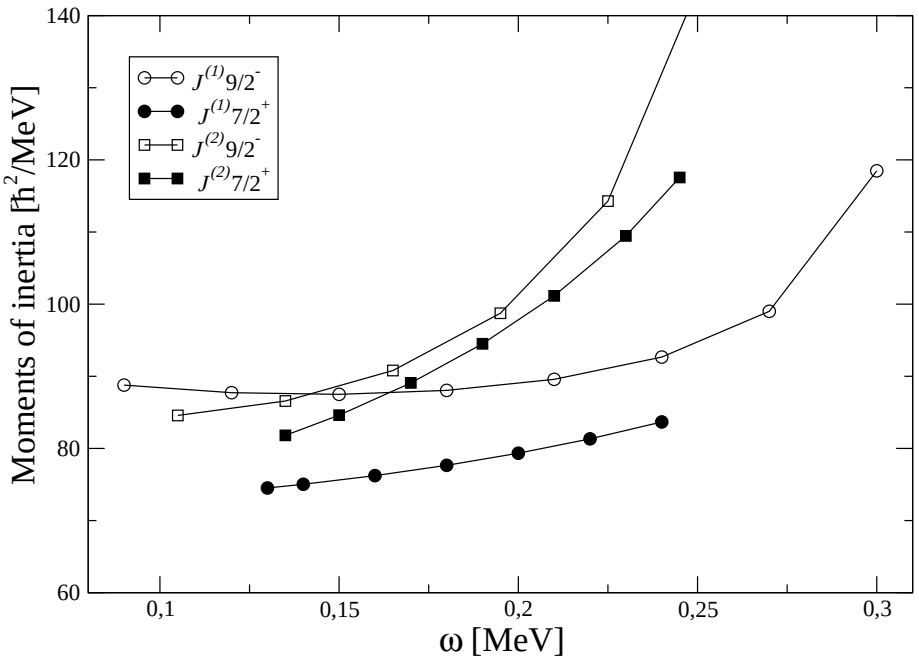

Figure 5.11: Calculated moments of inertia with cranked HFB for the rotational bands built on the $9/2^-[734]$ and $7/2^+[624]$ single-particle states. [Afa06, Rei05]

rotational bands built on the $9/2^-[734]$ state is followed if an alignment i_0 of $1\hbar$ is taken into account.
The presence of particle alignment for the $K = 9/2$ band is supported by cranked HFB calculations shown in figure 5.11 for both $K = 9/2$ and $K = 7/2$ [Afa06, Rei05]. For the $7/2^+[624]$ state originating from the $2g9/2$ orbital no alignment is expected and the moments of inertia converge at low frequencies. This behaviour corresponds to the plot in figure 4.23 for the I_0 spin assignment and alignment $i_0 = 0\hbar$. For the $K = 9/2$ band, however, the moments of inertia cross at a rotational frequency of around 0.14 MeV. This behaviour is similar to the one shown in figure 4.23 for the $I_0 + 1$ case, indicating an alignment i_0 of $1\hbar$.

The tentative partial level scheme of ^{253}No including the assignment of the band-head configuration and the deduced alignment is shown in figure 5.12.

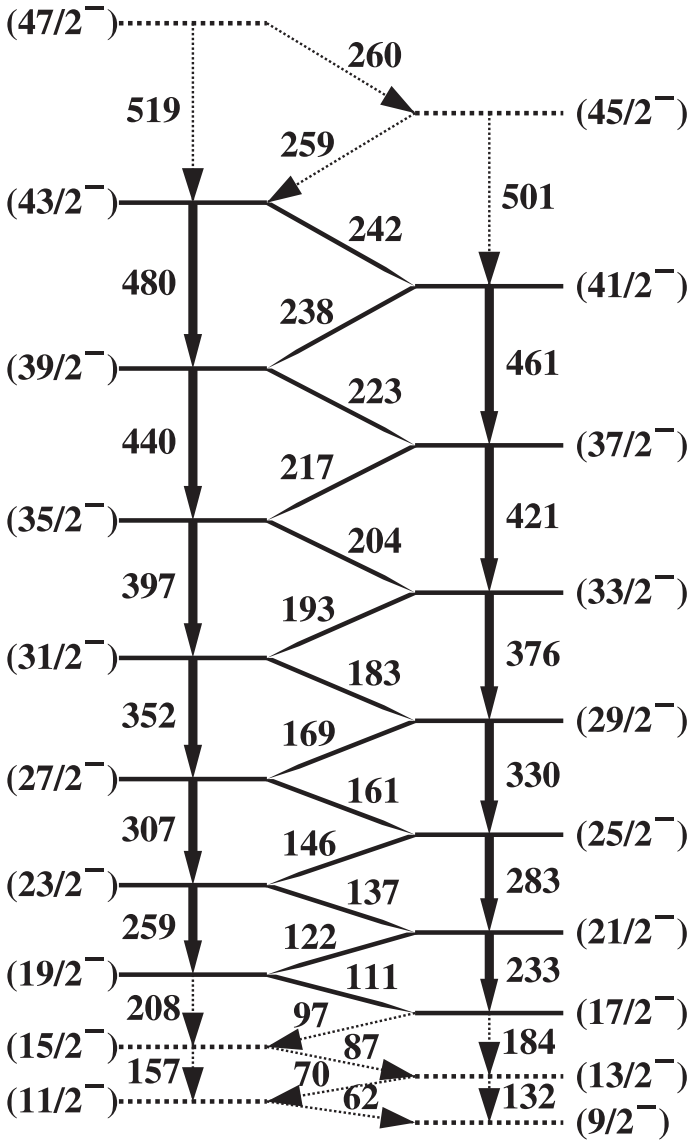

Figure 5.12: The tentative partial level scheme of ^{253}No.

5.1.2 Moments of inertia

The rotational properties of different transfermium nuclei have been studied and are here compared based on the dynamical moment of inertia of the observed rotational structures. The $\mathcal{J}^{(2)}$ values as a function of the rotational frequency ω for the known rotational bands in transfermium nuclei (^{251}Md [Cha06], ^{250}Fm [Bas06] and ^{252}No [Her02a] with $N = 150$, ^{253}No with $N = 151$ and ^{254}No with $N = 152$) are shown in figure 5.13. From this figure, a similarity in the behaviour of the $N = 150$ isotones is apparent.

Besides contributing to the stabilisation, pairing correlations play a substantial role in the collective motion of nuclei. They cause the moments of inertia to be smaller than the rigid rotor value of $\sim 150\ \hbar^2/\mathrm{MeV}$. As the rotational frequency increases, the pairing correlations are reduced by the alignment of the nucleon pairs and the moments of inertia show a gradual increase. The heavy $N = 152$ isotones have significantly slower alignment than the $N = 150$ isotones nuclei with a minimum predicted for ^{254}No [Ben03].
The difference in behaviour between $N = 150$ and $N = 152$ isotones has been qualitatively described by non-relativistic mean-field theory [Ben03] but the quantitative description is still lacking. Duguet *et al.* [Dug01] can reproduce the fact that the moment of inertia increases faster for ^{252}No than for ^{254}No, although the experimental difference is more pronounced. The results from cranked relativistic mean-field theory [Afa03] reproduce the moments of inertia rather well up to rotational frequencies of $\omega \approx 0.18$ MeV if the strength of the pairing correlations is reduced by ~ 12 % compared to lighter nuclei. The latter calculation gives the reversed behaviour compared to experiment but this is attributed to the fact that in the calculations $N = 150$ is obtained as a deformed shell gap while experimentally the gap is at $N = 152$. The fact that ^{254}No is more deformed than ^{252}No is apparent from the relative magnitudes of the dynamical moment of inertia at low frequencies.

In odd-mass nuclei, the pairing correlation is reduced because of the blocking effect of the odd nucleon, excluding the occupied level from pairing correlations. Consequently, the moments of inertia will be closer to the rigid rotor value and hence larger than in the even-even neighbour. This can be seen from figure 5.13 where the moment of inertia of ^{253}No lies higher than that of the even-even neighbour ^{254}No.

An upbend is visible for ^{252}No at a rotational frequency of around 0.2 MeV/$\hbar$. In ^{254}No such an upbend is predicted to happen at a rotational frequency of ~ 0.32 MeV/$\hbar$ due to the full alignment of the $\pi i13/2$ and $\nu j15/2$ valence nucleons. The rotational frequency ω for the experimental data approaches the calculated value at which the upbend is expected, but no upbend can yet be seen.

The moments of inertia of ^{254}No and ^{253}No, calculated by Bender *et al.* [Ben03], are

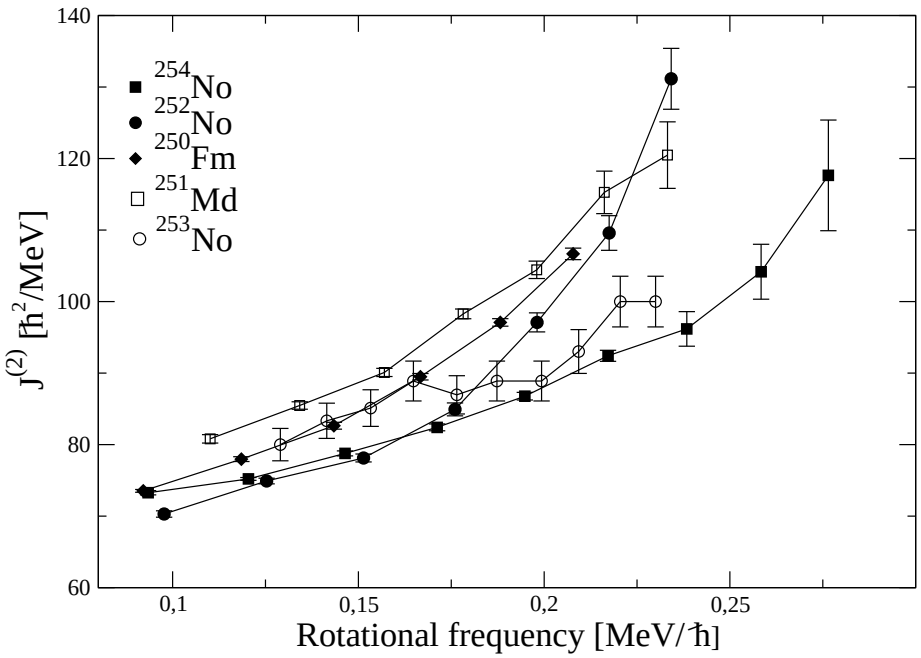

Figure 5.13: Dynamical moment of inertia $\mathcal{J}^{(2)}$ against rotational frequency for the ground-state band of ^{251}Md, ^{250}Fm, ^{252}No, ^{253}No and ^{254}No.

shown together with the experimentally obtained values in figures 5.14 and 5.15. The general behaviour is rather well described by the theoretical calculations for both nuclei. The observed band in ^{253}No with the tentative extensions to lower and higher transition energies seems to follow the theoretical predictions for the $K = 9/2$ band rather well.

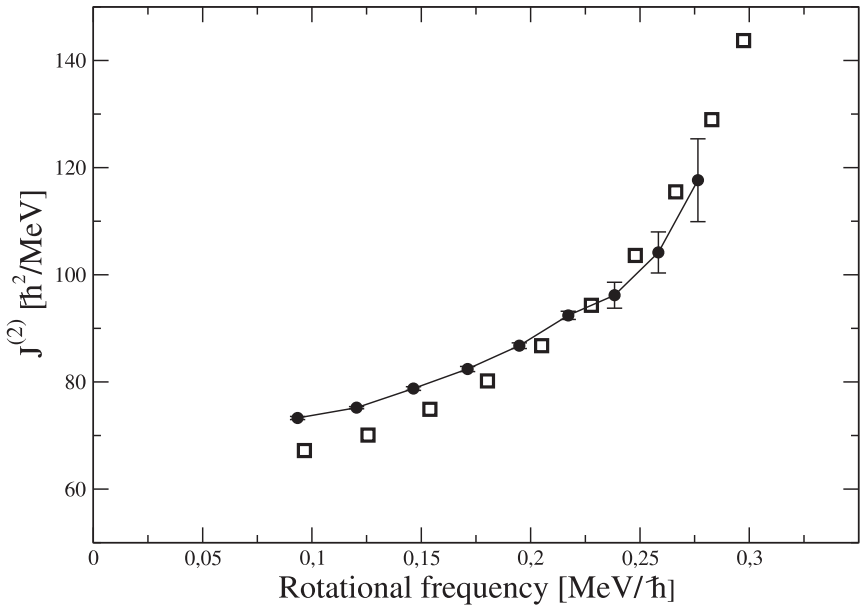

Figure 5.14: Calculated (empty symbols) and experimental (filled symbols) dynamical moment of inertia for ^{254}No. Calculations from [Ben03].

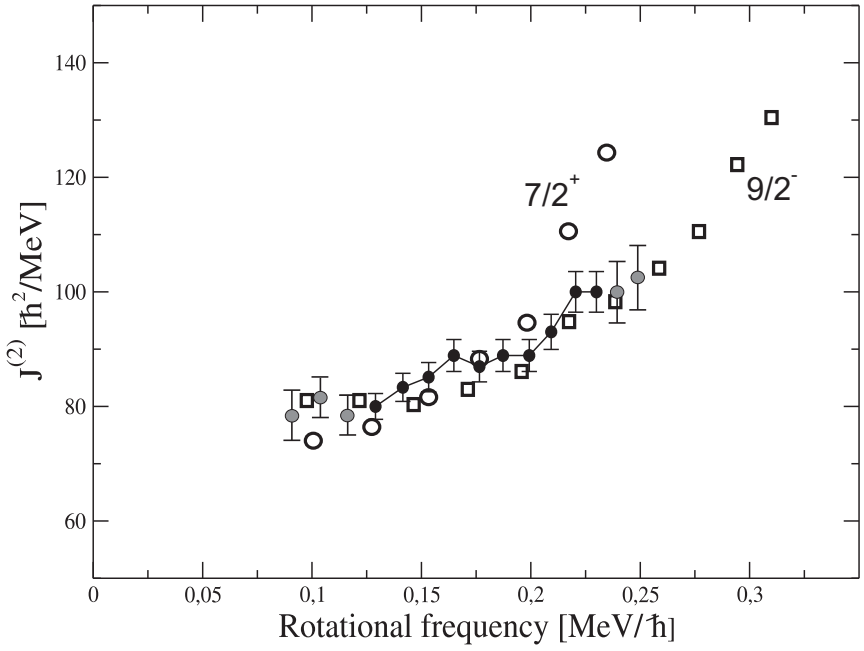

Figure 5.15: Calculated (empty symbols) and experimental (filled symbols) dynamical moment of inertia for ^{253}No. Calculations for one signature partner band for two different band-head assumptions [Ben03] (circles for $K = 7/2$ and squares for $K = 9/2$). Experimental values shown are for both signature partners combined with in black the main visible transitions and in grey the tentative extensions.

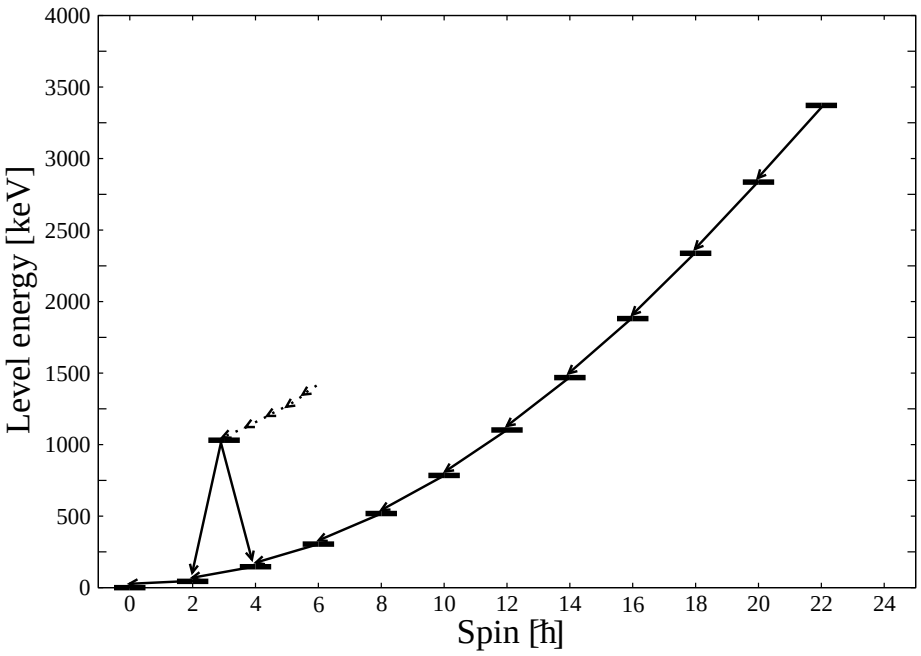

Figure 5.16: Yrast plot of ground-state band with suggested positioning of high energy lines. The assumed feeding pattern of the high-lying low-spin state is indicated with dashed lines.

5.2 Non-yrast structures: high-K states and isomers

The presence of high-energy γ-ray transitions and delayed electromagnetic decays point towards the observation of non-yrast structures in both ^{254}No and ^{253}No. The assignment of the transitions to the decay from isomeric states or high-K states to the ground-state band is discussed in this section.

5.2.1 $K = 3$ structure in ^{254}No

Having placed the two high-energy γ rays feeding the 4^+ and 2^+ states as shown schematically in the yrast plot in figure 5.16, it then remains to speculate as to the spin and parity of the decaying state. Due to the low level of statistics obtained, it has not been possible to perform an angular distribution analysis to aid in the determination of the γ-ray multipolarities. However, as the γ rays are observed prompt in the germanium detectors surrounding the target, the multipolarity of the transitions can immediately be constrained to $E1$, $M1$, $E2$ or $M2$. Higher multipolarity decays would exhibit too long a life-time to be observed promptly. The possible spins and parities of the decaying state are then $I^\pi = 2^\pm$, $3^\pm$ or $4^\pm$.
The basic argument for the following discussion is the fact that we observe the decay

out of a band-head state. Would this not be the case, interband γ-ray transitions from lower-lying band members to the ground-state band should be visible. And as can be seen from figure 4.11, no evidence for further interband transitions can be gleaned from the spectra.
The $I^\pi = 4^\pm$ possibility can then be quickly ruled out, as for a $K = 4$ band the transition is strongly K-hindered and hence too slow to be observed in the target array (see equations 2.34 and 2.35 and figure 2.11.).

Very little systematic data exist in this region of the nuclear chart, though in lighter isotopes of Fm, Cf and Cm, a number of octupole $K = 2^-$ bands (e.g. ^{250}Cf [Fre77], ^{246}Cm [Mul71, Ahm76]) and $K = 2^+$ or $K = 3^+$ bands (e.g. ^{256}Fm [Hal89], ^{252}Cf [Fie73]) have been observed. They are interpreted either as octupole vibrational states or two quasi-particle excitations.
The $I^\pi = 2^\pm$ possibilities can be ruled out on the basis of the observed decay pattern. For a $K = 2^+$ band-head state, the Alaga rules (see equation 2.33) suggest that for $E2$ transitions decaying to the 4^+, 2^+ and 0^+ states, the intensities should approximately have the relationship 3:100:85, respectively. This is clearly not what is observed, as there is no strong transition to the 0^+ ground state. The case of $K^\pi = 2^-$ can be ruled out by comparing the decay patterns observed from the known $K^\pi = 2^-$ octupole bands in the isotones ^{250}Cf and ^{246}Cm. In both cases, the 2^- state decays by a dominating $E1$ transition to the 2^+ state (see, for example refs. [Fre77, Ahm76]). Again, this is clearly not what is observed in the present case. The most plausible spin assignment is then $I = 3$.
Assignment of the parity of this state is difficult from the present data as there is no clear evidence for decays of the band members above this state. Feeding to this high-lying low-spin state is expected to proceed via highly-converted low-energy $M1$ transitions. Recently, a broad distribution comprising high-multiplicity electron cascades was observed in an in-beam conversion electron spectroscopic study of ^{254}No as mentioned in section 4.2.1. These cascades are expected to arise from $M1$ transitions in bands built on high-K states. It was not possible to observe these highly converted transitions in the present experiment.
As mentioned before, no other interband γ rays were observed. It could be argued that this non-observation of interband transitions suggests that such transitions are K-hindered, and are not observed as the decay is dominated by unhindered in-band low-energy $M1$ transitions.

In the octupole case the interband transitions may be expected to carry more intensity as it is assumed that the K-hindrance is less pronounced for collective structures. However, inspection of the level schemes and decay intensities observed in the $K = 2$ octupole bands in ^{250}Cf and ^{246}Cm shows that the intensities of interband transitions from the band members are at most only around 8 % [Fre77, Ahm76] of the decay intensity of the band-head state. Such transitions would have an intensity of less than 10 counts in the spectra obtained here and it is therefore again not possible to draw

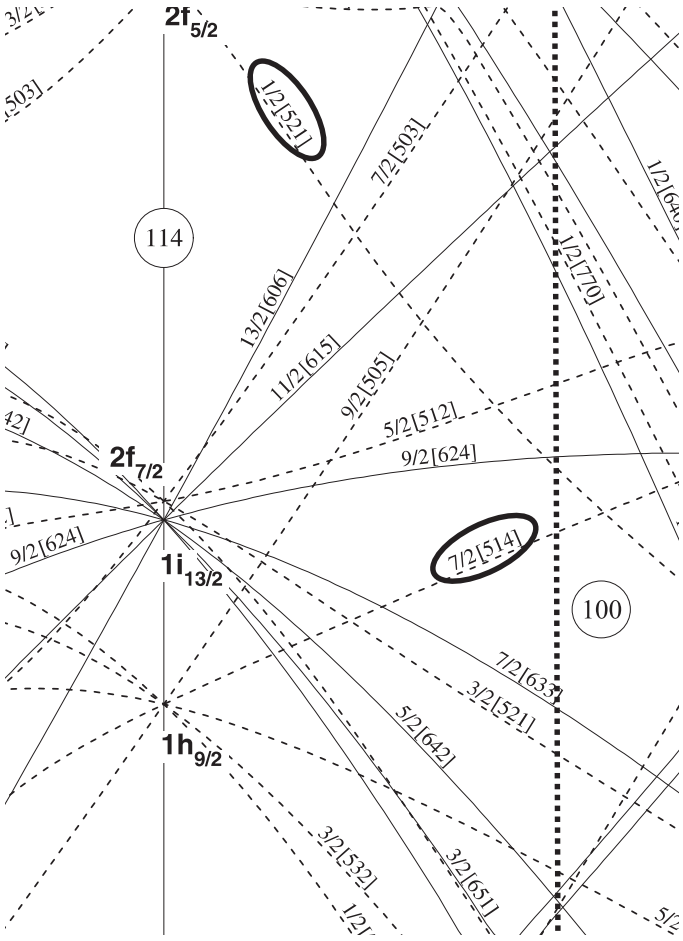

Figure 5.17: Detail of figure 2.5 showing the Nilsson states for proton number $Z \geq 82$. The single-particle states of interest here are circled and the deformation of ^{254}No is indicated by a dotted line.

any conclusion. The limited data available in the region also suggest that the $K = 2$ octupole bands lie lowest in energy, which may be an argument against the $K^\pi = 3^-$ scenario. Calculations of Neergård and Vogel performed in the 1970's also predict that the $K = 2$ octupole states lie lowest, at least up to Fm, the highest Z element considered [Nee70]. It should be noted, however, that the systematic behaviour is such that the energies of the $K = 2$ and $K = 3$ bands converge when going to heavier systems.

This then leaves the $K^\pi = 3^+$ scenario. An excellent candidate for a two quasi-particle $K^\pi = 3^+$ state can be formed by coupling the proton $7/2^-[514]$ and $1/2^-[521]$ orbitals which are close to the Fermi surface in ^{254}No (see figure 5.17). On the basis of Weisskopf estimates and the systematics of K-hindrance factors of Löbner *et al.* (see equation 2.35, table 2.1 and figure 2.11), the lifetime of such a $K^\pi = 3^+$ band-head

state is expected to be less than 1 ns. A lifetime at this level means that the state decays well within the focus of the detectors surrounding the target.

Experimental support for the tentative $K^\pi = 3^+$ assignment was obtained during a recent experiment, studying high-K isomers in ^{254}No.

5.2.2 K-isomers in ^{254}No

As mentioned in section 4.2.1, an isomeric state has been predicted and observed in ^{254}No. However, no discrete transitions depopulating the isomer could be detected.
Recently, a dedicated experiment to study high-K isomers in ^{254}No, carried out at Jyväskylä, could shed more light on the isomer decay path [Her05]. An isomeric state was observed with a 266(2) ms half-life, in good agreement with the previously published values, concluding that the same isomer is observed. An isomeric ratio of ~ 30 % was determined.
The PLANAR γ-ray spectrum in coincidence with an electron cascade revealed, apart from nobelium L and K X-rays, a strong 53 keV line and several regularly-spaced low-energy transitions. However, no coincident transitions of the ground-state band down to 4^+ were seen, which led to the conclusion that the isomer has a different decay path than previously assumed.
Furthermore, the same two high-energy transitions (842 and 943 keV) discussed in section 4.4.2 were observed in the CLOVER in coincidence with an electron cascade, with an additional weak line at 887 keV. So even though they are in the decay path of the isomer because of the delayed detection, they can not originate directly from the isomeric state due to the prompt detection. Hence, a decay path of the isomer via an intermediate structure was proposed in [Her05]. Determining the multipolarities of the high-energy transitions 841 and 943 keV as $M1$ and the 53 keV as $E1$, based on the nobelium K and L X-ray intensities respectively, and assuming $M1$ character for the weak low-energy transitions forming a rotational structure, the level scheme shown in 5.18 was obtained. Further support for the placement of the high-energy transitions as in the level scheme shown here and in figure 4.16 was provided from focal plane coincidence data where one coincidence on a zero background was observed between the high-energy 841 keV and the $4^+ \rightarrow 2^+$ ground-state band transitions.
These data support the reasoning presented above concerning the presence of a $K^\pi = 3^+$ band-head in ^{254}No decaying into the 4^+ and 2^+ ground-state band levels.

5.2.3 Isomerism in ^{253}No

Based on the feeding and de-excitation pattern of the isomeric state observed in ^{253}No, tentative assignments of its structure and excitation energy can be made.

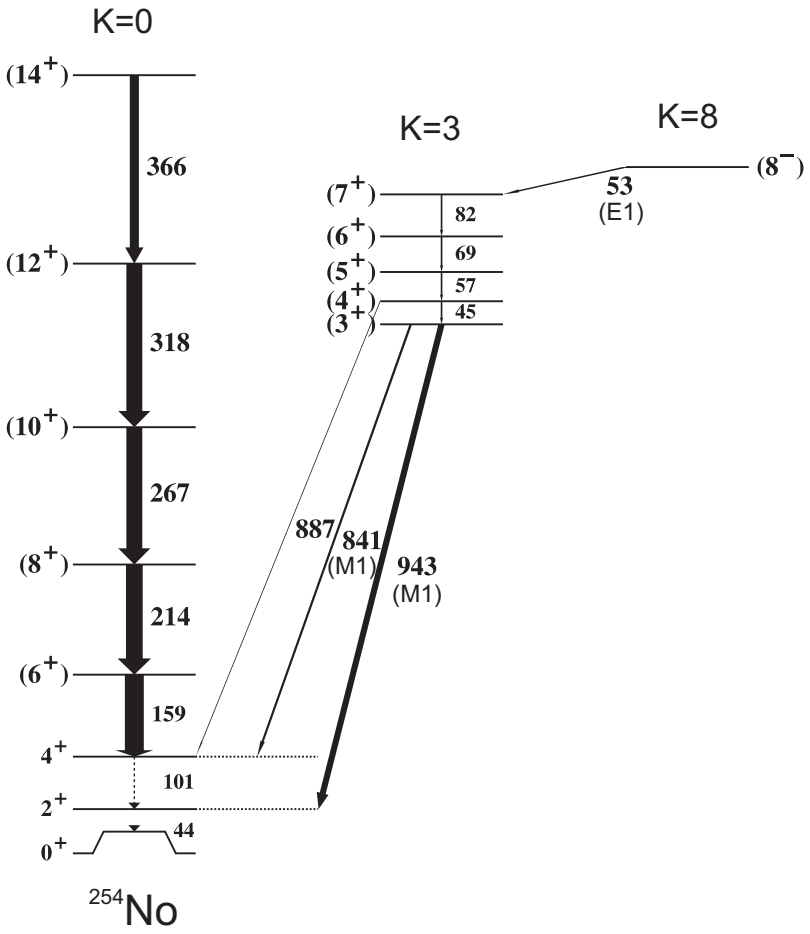

Figure 5.18: Partial level scheme of ^{254}No showing the decay path of the $K = 8$ isomer. [Her05]

In the absence of visible γ rays, the de-excitation path of the isomer was only observed via nobelium K X-rays and conversion electrons and is assumed to proceed via a single transition.
The nature of the electrons in figure 4.24 is not immediately evident. If the broad peak at around 140 keV is due to K-conversion of the transition de-exciting the isomeric state, the L and M electrons should lie at about 120 keV higher. For a $M2$ transition of 280 keV the ratio $\alpha_K/(\alpha_L + \alpha_M)$ is 1.92 so the peak comprising L and M electrons should only be at most a factor of two smaller but is absent in the spectrum. If on the other hand the visible electrons are L and M electrons, the K electrons should be present around 20 keV, which is below the threshold of the detectors. In addition, a fit of the broad electron peak with two gaussian shapes gives a difference between the two centroids close to the difference in binding energy between the L and M electrons in nobelium and a FWHM close to that of the ^{133}Ba source data. Hence it is assumed that the visible electrons are L and M electrons and the excitation energy of the isomer is determined to be 160(10) keV based on equation 2.38. The multipolarity of the transition can be verified by comparing the ratio of K conversion obtained from the K X-ray intensity to the L+M conversion derived from the electron intensity with the theoretical values (see table 5.2). The experimental α_K/α_{L+M} ratio of 0.73(22) is most consistent with an $M2$ transition.

Table 5.2: Theoretical values of α_K/α_{L+M} for a 160 keV transition in ^{253}No assuming different multipolarities.

transition	$E1$	$M1$	$E2$	$M2$	$E3$	$M3$
α_K/α_{L+M}	2.9	3.5	0.0070	1.3	0.0011	0.12

No clear transitions feeding the isomeric state could be distinguished in figure 4.26, suggesting that the band built on the isomeric state mainly decays via highly converted transitions. The state is therefore expected to have a large negative g_K value, favouring $M1$ transition strength and as such difficult to detect via γ-ray spectroscopy. Based on the available low-lying levels shown in figure 4.6, a suitable candidate for the isomeric state would be the $5/2^+$ state with $g_K = -0.41$, decaying by an $M2$ transition to the $9/2^-$ ground state.

Shortly after this experiment, an α-γ decay study of ^{257}Rf was carried out by Hessberger *et al.* [Hes06]. They also clearly observed delayed nobelium K X-rays but no γ-ray transitions de-exciting the isomeric $5/2^+[622]$ state were observed. They deduced a tentative transition energy of 180(30) keV in case of a mixed $M2/E3$ transition with a half-life of 23(4) μs. Hence this experiment confirms the values obtained here. Both recent experiments disagree with the results obtained in [Hes97].

5.2.4 Other non-yrast structures

Signs of non-yrast structures have been observed in several transfermium nuclei.
In the even-even nuclei ^{254}No, ^{252}No and ^{250}Fm a concentration of closely spaced peaks is observed at around 600 keV. They are assumed to be inter-band transitions between a β-vibrational band and the ground-state band. The transition energies in the two bands are expected to be similar and therefore all the interband transitions are concentrated at around the same energy.
In those even-even nuclei transitions at higher energy are also observed. In a similar manner to the interpretation given for ^{254}No they are expected to de-excite high-K states and be part of an isomeric decay path.

A strong high-energy γ-ray at 802(1) keV has been detected in ^{253}No, the origin of which is not yet known. Measurement of the multipolarity of the transition was not possible and hence only speculation regarding the character of the de-exciting state can be made. States around or above 1 MeV in this region could be due to a three quasi-particle excitation or a vibrational excitation [Ahm05].
If the state is a three quasi-particle excitation, the most evident configuration for such a state would be the coupling of the lowest-lying two-proton configuration with the odd neutron, i.e. $((\pi 7/2^-[514] \otimes \pi 1/2^-[521])^{3^+} \otimes \nu 9/2^-[734])^{15/2^-}$. This state is then assumed to decay by the $\Delta K = 3$ hindered 802(1) keV $E2$ transition to the $11/2^-$ member of the $9/2^-[734]$ rotational band, placing the level at 864 keV. In the homologue rare-earth $N = 102$ isotones, similar structures have been observed around $1 - 2$ MeV. The lowest $K^\pi = 3^+$ state in the even-even nuclei ^{174}Hf and ^{172}Yb has been assigned a two quasi-neutron configuration $(\nu 5/2^-[512] \otimes \nu 1/2^-[521])^{3^+}$ and in the odd-Z nucleus ^{177}Re the lowest lying three quasi-particle configuration consists of a $\pi 9/2^-[514]$ proton coupled to the same two quasi-neutron 3^+ structure $((\nu 5/2^-[512] \otimes \nu 1/2^-[521])^{3^+} \otimes \pi 9/2^-[514])^{15/2^-}$ [nndc]. The three quasi-particle state in ^{177}Re decays into the rotational band built on the $\pi 9/2^-[514]$ configuration.
Recent decay spectroscopic studies by Ahmad *et al.* studying the nuclei ^{249}Bk [Ahm05] and ^{251}Cf [Ahm05a] revealed the presence of β- and octupole-vibrational bands at around 800 keV. Hence the high-energy γ-ray at 802(1) keV could also originate from a vibrational structure.

5.3 Decay spectroscopy

The observed α decay of the implanted recoils can be used to study decay properties of the ground state of the produced nuclei and level structure in the daughter nucleus. The α-decay branching ratio was determined for ^{254}No and ^{253}No. In the ^{253}No experiment the focal plane spectrometer was completed and allowed α-γ-electron coincidence measurements of ^{249}Fm to be carried out.

5.3.1 Alpha-decay branching ratios of ^{254}No and ^{253}No

The α-decay branching ratios of ^{254}No and ^{253}No were derived from the experimental data by comparing the nobelium K X-ray yield in the recoil-gated and α-tagged γ-ray singles spectra. After correcting for α detection efficiency ($\sim$ 55 %) and limited search time, an estimate of the α-decay branching ratio was obtained. For ^{254}No the α-decay branching ratio was determined to be 81(9) % while for ^{253}No a much lower value of 48(6) % was obtained.
To obtain those values in a different manner, the electron capture and β^+ decay path was followed and the produced number of the α-decaying granddaughter nuclei was derived from the singles α spectrum. As this method relies on the previously measured branching ratios for the granddaughter nucleus, the results are merely used to check the values obtained previously. ^{254}No has ^{254}Fm as an EC+β^+ granddaughter which has an estimated α-decay branching ratio of 100 %, resulting in an α-decay branching ratio for ^{254}No of $\sim$ 92 %, close to the previous value. Similarly, in ^{253}No, the electron capture decay grand-daughter ^{253}Fm has an α-decay branching ratio of 12(1) % and a half-life of 3 days. Taking both factors into account an α-decay branching ratio of $\sim$ 50 % was obtained, confirming the previously stated value.
The value obtained for ^{254}No is in agreement with the earlier measured value of 90(4) % [nndc]. The extracted α-decay branching ratio of ^{253}No is much lower than for ^{254}No. Up to now, only α-decay has been observed for ^{253}No and no branching ratio has been determined experimentally. Although systematic deduction of the EC half-life (10 min) [nndc] gives an estimated EC branching ratio of 15 %, which does not fully support the low α-decay branch, in other odd mass nobelium nuclei a significant EC+β^+ branch has been observed, making the obtained value of 48(6) % plausible.

5.3.2 Level structure in α-decay daughter ^{249}Fm

Three γ-ray transitions and associated internal conversion electrons could be observed in the α-γ decay study of ^{253}No and the multipolarity of the highest two transitions could be determined by comparing the L+M conversion coefficient to the theoretical

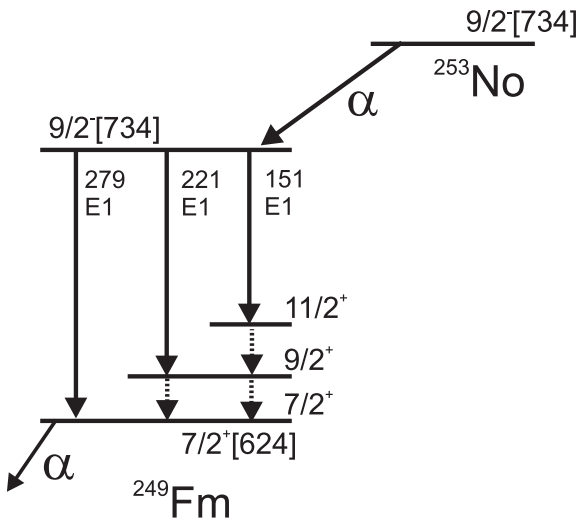

Figure 5.19: Level scheme of α-decay daughter ^{249}Fm obtained in an α-γ decay study of ^{253}No.

values as shown in table 5.3. The transitions are most compatible with an $E1$ or $E2$ transition according to present data and determined to be $E1$ in previous studies.

Table 5.3: Comparison of theoretical and experimental values for α_{L+M}.

transition	$E1$	$M1$	$E2$	$M2$	exp
221 keV	0.022	1.3	0.87	7.0	0.06(3)
279 keV	0.013	0.65	0.34	3.0	0.17(12)

Further it is noticeable that few K X-rays are observed, indicating that the possible non-observed highly converted transitions have a low transition energy.
With this information and the fact that no coincidences were detected between the observed transitions, the level scheme from two earlier studies (see section 4.2.2) was confirmed and is shown in figure 5.19. The α-γ decay study supports the $9/2^-$ spin and parity assignment of the ^{253}No ground state. No new information could be added to the previously obtained level scheme and the data was mainly used to demonstrate that α-γ-electron decay spectroscopy can be performed simultaneously with in-beam studies at the JUROGAM-RITU-GREAT setup.

5.4 Summary and future prospects

The gas-filled recoil separator RITU at JYFL has recently been provided with powerful and efficient spectrometers both at the target and at the focal plane. The JUROGAM target array and the GREAT focal plane spectrometer, in combination with the TDR data-acquisition system, give access to neutron-deficient heavy elements using the recoil-gating technique.
In this work, in-beam γ-ray spectroscopic studies of ^{254}No and ^{253}No have been discussed. In both nuclei, a rotational band was observed and interpreted as built upon the ground state, although in case of ^{253}No this assignment is tentative. Both isotopes were found to be robust against fission at least up to $22\hbar$, meaning the deformed shell stabilisation against fission persists up to high rotational frequencies. In both cases, the rotational properties were found to agree rather well with various theoretical predictions.
Evidence for non-yrast structure was found in ^{254}No and interpreted to be a $K^\pi = 3^+$ two quasi-particle excitation which was later confirmed in a dedicated study of high-K isomers in ^{254}No. Now the position of the $K^\pi = 3^+$ (and $K^\pi = 8^-$) state is fixed experimentally, theoretical predictions of the relative positions of the single-particle states in this region can be adjusted.
Other indications for non-yrast structures are present in spectra of both ^{254}No and ^{253}No and thought to originate from the decay out of a vibrational band or a high-K state.
Whilst for the experiment to study ^{254}No the focal plane spectrometer was not completed, in the study of ^{253}No the observation of isomeric states and α-decay fine structure was possible. Although the transitions feeding the isomeric state could not be observed, both X-rays and conversion electrons depopulating the isomeric state were detected in the GREAT spectrometer. The 22(4) μs isomer has tentatively been assigned a spin and parity of $5/2^+$ and an excitation energy of 160(10) keV.
In the α-decay daughter ^{249}Fm, three levels were identified and the spin and parity of the ground-state of ^{253}No was confirmed to be $9/2^-$.

One goal in the study of transfermium elements is to learn more about the region beyond it, around the next spherical doubly magic nucleus. Although this is a valid motivation, extrapolation from the region around ^{254}No to the region around $Z \sim 120$ and $N \sim 184$ is not that straightforward. After all, the shell structure of those nuclei is governed by large mass, hence weakened spin-orbit interaction, and large electric charge, which means prominent Coulomb interaction. Also the single-particle level density for very heavy elements is very high, so small changes in single-particle energies can produce spherical shell gaps at different proton or neutron numbers. However, transfermium elements are the heaviest elements which are at present accessible for in-beam spectroscopy and hence provide the best information we can obtain at high masses.

To further explore the region around ^{254}No, proposals have been accepted to study ^{248}Fm and ^{256}Rf for the first time, and the high-K isomeric structures in ^{254}No and ^{250}Fm at JYFL with the present setup.
The occurrence of highly converted transitions in the odd-mass transfermium nuclei and in the bands built upon high-K isomeric states renders it very difficult to study the nuclei via in-beam γ-ray spectroscopy alone. Simultaneous γ-ray and electron spectroscopy at the target position would be the best way to further investigate the region around ^{254}No. It is hoped that such studies will be possible within a few years at JYFL with the development of the new SAGE spectrometer which is in principle a combination of the SACRED and JUROGAM target spectrometers. SAGE will be designed and built in a collaboration led by the University of Liverpool and Daresbury Laboratory in the U.K..
A study of ^{253}No using this highly efficient target array will be the best way of confirming the assignments of the rotational structure seen in in-beam conversion electron and γ-ray spectroscopic studies separately. The configuration of the single-particle state the band is built on can be deduced from the $B(M1)/B(E2)$ branching ratio, which can be accurately measured provided both γ rays and conversion electrons are detected in the same experiment. Also for the study of the structures based on K-isomers, the combination of γ-ray and electron spectroscopy is desirable.
A further development planned at JYFL is the introduction of digital electronics. This would allow much higher count rates in individual channels and hence higher beam intensities can be used.

A broader range of nuclei will be accessible with the use of radioactive ion beams. More development is however needed as the current available intensities are two orders of magnitude lower than present stable beam intensities. But once the required intensities will be available, more neutron-rich heavy elements can be studied.
At this moment, only in-beam and decay spectroscopic studies are carried out in this region. A wide array of techniques are waiting to be applied: e.g. plunger measurements to measure the life-times of the excited levels [Dew03] and precise mass measurements of very heavy elements using e.g. SHIPTRAP [ship].

The search for the superheavy island of stability will therefore remain one of the main focuses of nuclear structure investigations.

References

[Abr73] M.M. Abraham, L.A. Boatner, C.B. Finch, R.W. Reynolds and W.P. Unruh, Phys. Lett. A **44** (1973) 527.

[Afa03] A.V. Afanasjev, T.L. Khoo, S. Frauendorf, G.A. Lalazissis and I. Ahmad, Phys. Rev. C **67** (2003) 024309.

[Afa06] A.V. Afanasjev, T.L. Khoo, private communication.

[Ahm76] I. Ahmad, D.D. Sharma and R.K. Sjoblom, Nucl. Phys. A **258** (1976) 221.

[Ahm76a] I. Ahmad, R.K. Sjoblom and P.R. Fields, Phys. Rev. C **14** (1976) 218.

[Ahm05] I. Ahmad, F.G. Kondev, E.F. Moore, M.P. Carpenter, R.R. Chasman, J.P. Greene, R.V.F. Janssens, T. Lauritsen, C.J. Lister, D. Seweryniak, R.W. Hoff, J.E. Evans, R.W. Lougheed, C.E. Porter and L.K. Felker, Phys. Rev. C **71** (2005) 054305.

[Ahm05a] I. Ahmad, J.P. Greene, E.F. Moore, F.G. Kondev, R.R. Chasman, C.E. Porter and L.K. Felker, Phys. Rev. C **72** (2005) 054308.

[Ala55] G. Alaga, K. Alder, A. Bohr and B.R. Mottelson, Dan. Mat. Fys. Medd. **29** (1955) 1.

[And04] A.N. Andreyev, P.A. Butler, R.D. Page, D.E. Appelbe, G.D. Jones, D.T. Joss, R.-D. Herzberg, P.H. Regan, J. Simpson and R. Wadsworth, Nucl. Instr. and Meth. in Phys. Res. A **533** (2004) 422.

[Bas06] J.E. Bastin, R.-D. Herzberg, P.A. Butler, G.D. Jones, R.D. Page, D.G. Jenkins, N. Amzal, P.M.T. Brew, N.J. Hammond, R.D. Humphreys, P.J.C. Ikin, T. Page, P.T. Greenlees, P.M. Jones, R. Julin, S. Juutinen, H. Kankaanpää, A. Keenan, H. Kettunen, P. Kuusiniemi, M. Leino, A.P. Leppänen, M. Muikku, P. Nieminen, P. Rahkila, C. Scholey, J. Uusitalo, E. Bouchez, A. Chatillon, A. Hürstel, W. Korten, Y. Le Coz, Ch. Theisen, D. Ackermann, J. Gerl, K. Helariutta, F.P. Hessberger, Ch. Schlegel, H.J. Wollersheim, M. Lach, A. Maj, W. Meczynski, J. Styczen, T.L. Khoo, C.J. Lister, A.V. Afanasjev, H.J. Maier, P. Reiter, P. Bednarczyk, K. Eskola and K. Hauschild, Phys. Rev. C **73** (2006) 024308.

[Bem73] C.E. Bemis, Jr., R.J. Silva, D.C. Hensley, O.L. Keller, Jr., J.R. Tarrant, L.D. Hunt, P.F. Dittner, R.L. Hahn and C.D. Goodman, Phys. Rev. Lett. **31** (1973) 647.

[Ben99] M. Bender, K. Rutz, P.-G. Reinhard, J.A. Maruhn and W. Greiner, Phys. Rev. C **60** (1999) 034304.

[Ben03] M. Bender, P. Bonche, T. Duguet and P.-H. Heenen, Nucl. Phys A **723** (2003) 354.

[Ben03a] M. Bender, P.-H. Heenen and P.-G. Reinhard, Rev. Mod. Phys. **75** (2003) 121.

[Boh75] A. Bohr and B.R. Mottelson, Nuclear Structure Volume II: Nuclear Deformations, W.A. Benjamin Inc., New York (1975).

[bricc] Conversion coefficient calculator http://wwwrsphysse.anu.edu.au/ txk103/bricc/.

[But96] P.A. Butler, P.M. Jones, K.J. Cann, J.F.C. Cocks, G.D. Jones, R. Julin and W.H. Trzaska, Nucl. Instr. and Meth. in Phys. Res. A **381** (1996) 433.

[But02] P.A. Butler, R.D. Humphreys, P.T. Greenlees, R.-D. Herzberg, D.G. Jenkins, G.D. Jones, H. Kankaanpää, H. Kettunen, P. Rahkila, C. Scholey, J. Uusitalo, N. Amzal, J.E. Bastin, P.M.T. Brew, K. Eskola, J. Gerl, N.J. Hammond, K. Hauschild, K. Helariutta, F.-P. Hessberger, A. Hürstel, P.M. Jones, R. Julin, S. Juutinen, A. Keenan, T.-L. Khoo, W. Korten, P. Kuusiniemi, Y. Le Coz, M. Leino, A.-P. Leppänen, M. Muikku, P. Nieminen, S.W. Odegard, T. Page, J. Pakarinen, P. Reiter, G. Sletten, Ch. Theisen and H.-J. Wollersheim, Phys. Rev. Lett. **89** (2002) 202501.

[But03] P.A. Butler, R.D. Humphreys, P.T. Greenlees, R.-D. Herzberg, D.G. Jenkins, G.D. Jones, H. Kankaanpää, H. Kettunen, P. Rahkila, C. Scholey, J. Uusitalo, N. Amzal, C. Andreoiu, A. Andreyev, D. Appelbe, J.E. Bastin, P.M.T. Brew, K. Eskola, S.J. Freeman, J. Gerl, N.J. Hammond, K. Hauschild, K. Helariutta, F.-P. Hessberger, A. Hürstel, P.J.C. Ikin, P.M. Jones, D.T. Joss, R. Julin, S. Juutinen, A. Keenan, T.-L. Khoo, W. Korten, P. Kuusiniemi, Y. Le Coz, M. Leino, A.-P. Leppänen, M. Muikku, P. Nieminen, S.W. Odegard, R.D. Page, T. Page, J. Pakarinen, P. Reiter, J. Simpson, G. Sletten, Ch. Theisen, B.J. Varley and H.-J. Wollersheim, Acta. Phys. Pol. B **34** (2003) 2107.

[Cas00] R.F. Casten, Nuclear Structure from a Simple Perspective 2nd edition, Oxford University Press (2000).

[Cha06] A. Chatillon *et al.*, submitted to Phys. Rev. Lett..

[Cwi94] S. Ćwiok, S. Hofmann and W. Nazarewicz, Nucl. Phys. A **573** (1994) 356.

[Dav89] C.N. Davids and J.D. Larson, Nucl. Instrum. and Meth. in Phys. Res. **B** 40/41 (1989) 1224.

[Dew03] A. Dewald, R. Peusquens, B. Saha, P. von Brentano, A. Fitzler, T. Klug, I. Wiedenhover, M.P. Carpenter, A. Heinz, R.V.F. Janssens, F.G. Kondev, C.J. Lister, D. Seweryniak, K. Abu Saleem, R. Krucken, J.R. Cooper, C.J. Barton, K. Zyromski, C.W. Beausang, Z. Wang, P. Petkov, A.M. Oros-Peusquens, U. Garg and S. Zhu, Phys. Rev. C **68** (2003) 034314.

[Dug01] T. Duguet, P. Bonche and P.-H. Heenen, Nucl. Phys A **679** (2001) 427.

[Egi00] J.L. Egido and L.M. Robledo, Phys Rev Lett. **85** (2000) 1198.

[Eji89] H. Ejiri and M.J.A de Voight, Gamma-ray and electron spectroscopy in nuclear physics, Oxford science publications (1989).

[Fie73] P.R. Fields, I. Ahmad, R.F. Barnes and R.K. Sjoblom, Nucl. Phys. A **208** (1973) 269.

[Fir96] R.B. Firestone, Table of Isotopes 8th edition, Virginia S. Shirley (1996).

[Fre77] M. S. Freedman, I. Ahmad, F.T. Porter, R.K. Sjoblom, R.F. Barnes, J. Lerner and P.R. Fields, Phys. Rev. C **15** (1977) 760.

[Gag89] H.W. Gäggeler, D.T. Jost, A. Türler, P. Armbruster, W. Brüchle, H. Folger, F.P. Hessberger, S. Hofmann, G. Münzenberg, V. Ninov, W. Reisdorf, M. Schädel, K. Sümmerer, J.V. Kratz, U. Scherer and M.E. Leino, Nucl. Phys. A **502** (1989) 561.

[geant] Geant Detector Simulation Tool, CERN (1993)
http://wwwinfo.cern.ch/asd/geant.

[Ghi58] A. Ghiorso, T. Sikkeland and J.R. Walton, Phys. Rev. Lett. **1** (1958) 18.

[Ghi73] A. Ghiorso, K. Eskola, P. Eskola and M. Nurmia, Phys. Rev. C **7** (1973) 2032.

[Gre03] P.T. Greenlees, A.N. Andreyev, J. Bastin, F. Becker, E. Bouchez, P.A. Butler, J.F.C. Cocks, Y. Le Coz, K. Eskola, J. Gerl, K. Hauschild, K. Helariutta, R.-D. Herzberg, F.P. Hessberger, R.D. Humphreys, A. Hürstel, D.G. Jenkins, G.D. Jones, P. Jones, R. Julin, S. Juutinen, H. Kankaanpää, A. Keenan, H. Kettunen, T.L. Khoo, W. Korten, P. Kuusiniemi, M. Leino, A.-P. Leppänen, M. Muikku, P. Nieminen,

R.D. Page, T. Page, J. Pakarinen, P. Rahkila, P. Reiter, Ch. Schlegel, C. Scholey, Ch. Theisen, J. Uusitalo, K. Van de Vel, R. Wadsworth and H.-J. Wollersheim, Eur. Phys. J. A **20** (2003) 87.

[Hal89] H.L. Hall, K.E. Gregorich, R.A. Henderson, D.M. Lee, D.C. Hoffman, M.E. Bunker, M.M. Fowler, P. Lysaight, J.W. Starner and J.B. Wilhelmy, Phys. Rev. C **39** (1989) 1866.

[Hax49] O. Haxel, J.H.D. Jensen and H.E. Suess, Phys. Rev. **75** (1949) 1766.

[Hee05] P.-H. Heenen, private communication.

[Her02] R.-D. Herzberg, N. Amzal, J.E. Bastin, F. Becker, P.M.T. Brew, P.A. Butler, A.J.C. Chewter, J.F.C. Cocks, O. Dorvaux, K. Eskola, J. Gerl, P.T. Greenlees, N.J. Hammond, K. Hauschild, K. Helariutta, F. Hessberger, M. Houry, A. Hürstel, R.D. Humphreys, G.D. Jones, P.M. Jones, R. Julin, S. Juutinen, H. Kankaanpää, H. Kettunen, T.L. Khoo, W. Korten, P. Kuusiniemi, Y. Le Coz, M. Leino, A.P. Leppänen, C.J. Lister, R. Lucas, M. Muikku, P. Nieminen, R.D. Page, T. Page, P. Rahkila, P. Reiter, Ch. Schlegel, C. Scholey, G. Sletten, O. Stezowski, Ch. Theisen, W.H. Trzaska, J. Uusitalo and H.J. Wollersheim, Eur. Phys. J. A **15** (2002) 205.

[Her02a] R.-D. Herzberg, N. Amzal, F. Becker, P.A. Butler, A.J.C. Chewter, J.F.C. Cocks, O. Dorvaux, K. Eskola, J. Gerl, P.T. Greenlees, N.J. Hammond, K. Hauschild, K. Helariutta, F. Hessberger, M. Houry, G.D. Jones, P.M. Jones, R. Julin, S. Juutinen, H. Kankaanpää, H. Kettunen, T.L. Khoo, W. Korten, P. Kuusiniemi, Y. Le Coz, M. Leino, C.J. Lister, R. Lucas, M. Muikku, P. Nieminen, R.D. Page, P. Rahkila, P. Reiter, Ch. Schlegel, C. Scholey, O. Stezowski, Ch. Theisen, W.H. Trzaska, J. Uusitalo and H.J. Wollersheim, Phys. Rev. C **65** (2001) 014303.

[Her04] R.-D. Herzberg, J. Phys G: Nucl. Part. Phys. **30** (2004) R123.

[Her05] R.-D. Herzberg *et al.*, Physica Scripta, conference proceedings Nilsson 2005, Lund, in print (2005).

[Hes89] F. P. Hessberger, S. Hofmann, G. Münzenberg, K.-H. Schmidt and P. Armbruster, Nucl. Instrum. and Meth. in Phys. Res. **A** 274 (1989) 522.

[Hes97] F.P. Hessberger, S. Hofmann, V. Ninov, P. Armbruster, H. Folger, G. Münzenberg, H.J. Schött, A.G. Popeko, A.V. Yeremin, A.N. Andreyev and S. Saro, Z. Phys. A. **359** (1997) 415.

[Hes04] F.P. Hessberger, S. Hofmann, D. Ackermann, P. Cagarda, R.-D. Herzberg, I. Kojouharov, P. Kuusiniemi, M. Leino and R. Mann, Eur. Phys. J. A **22** (2004) 417.

[Hes06] F.P. Hessberger *et al.*, to be published.

[Hey94] K.L.G. Heyde, The nuclear shell model 2nd edition, Springer-Verlag (1994).

[Hof00] S. Hofmann and G. Münzenberg, Rev. Mod. Phys. **72** (2000) 733.

[Hum04] R.D. Humphreys, P.A. Butler, J.E. Bastin, P.T. Greenlees, N.J. Hammond, R.-D. Herzberg, D.G. Jenkins, G.D. Jones, H. Kankaanpää, A. Keenan, H. Kettunen, T. Page, P. Rahkila, C. Scholey, J. Uusitalo, N. Amzal, P.M.T. Brew, K. Eskola, J. Gerl, K. Hauschild, K. Helariutta, F.-P. Hessberger, A. ürstel, P.M. Jones, R. Julin, S. Juutinen, T.-L. Khoo, W. Korten, P. Kuusiniemi, Y. Le Coz, M. Leino, A.-P. Leppänen, M. Muikku, P. Nieminen, S.W. Odegard, J. Pakarinen, P. Reiter, G. Sletten, Ch. Theisen, and H.-J. Wollersheim, Phys. Rev. C **69** (2004) 064324.

[Jon02] G.D. Jones, Nucl. Instr. and Meth. in Phys. Res. A **488** (2002) 471.

[Kan04] H. Kankaanpää, P.A. Butler, P.T. Greenlees, J.E. Bastin, R.D. Herzberg, R.D. Humphreys, G.D. Jones, P. Jones, R. Julin, A. Keenan, H. Kettunen, M. Leino, L. Miettinen, T. Page, P. Rahkila, C. Scholey and J. Uusitalo, Nucl. Instr. and Meth. in Phys. Res. A **534** (2004) 503.

[Kan95] J. Kantele, Handbook of Nuclear Spectrometry, Academic press (1995).

[Kho06] T.-L. Khoo, private communication.

[Kra88] K.S. Krane, Introductory nuclear physics, John Wiley & Sons (1988).

[Laz89] Yu.A. Lazarev, Yu.V. Lobanov, R.N. Sagaidak, V.K. Utyonkov, M. Hussonnois, Yu.P. Kharitonov, I.V. Shirokovsky, S.P. Tretyakova and Yu.Ts. Oganessian, Phys. Scr. **39** (1989) 422.

[Laz01] I.H. Lazarus, E.E. Appelbe, P.A. Butler, P.J. Coleman-Smith, J.R. Cresswell, S.J. Freeman, R.D. Herzberg, I. Hibbert, D.T. Joss, S.C. Letts, R.D. Page, V.F.E. Pucknell, P.H. Regan, J. Sampson, J. Simpson, J. Thornhill and R. Wadsworth, IEEE Transactions on Nuclear Science **48** (2001) 567.

[Lei95] M. Leino, J. äystö, T. Enqvist, P. Heikkinen, A. Jokinen, M. Nurmia, A. Ostrowski, W.H. Trzaska, J. Uusitalo, K. Eskola, P. Armbruster and V. Ninov, Nucl. Instr. and Meth. in Phys. Res. B **99** (1995) 653.

[Lei99] M. Leino, H. Kankaanpää, R.-D. Herzberg, A.J. Chewter, F.P. Hessberger, Y. Le Coz, F. Becker, P.A. Butler, J.F.C. Cocks, O. Dorvaux, K. Eskola, J. Gerl, P.T. Greenlees, K. Helariutta, M. Houry, G.D. Jones, P. Jones, R. Julin, S. Juutinen, H. Kettunen, T.L. Khoo, A. Kleinböhl, W. Korten, P. Kuusiniemi, R. Lucas, M. Muikku, P. Nieminen, R.D. Page, P. Rahkila,

P. Reiter, A. Savelius, Ch. Schlegel, Ch. Theisen, W.H. Trzaska and H.-J. Wollersheim, Eur. Phys. J. A **6** (1999) 63.

[Liu98] S.X. Liu and J.Y. Zeng, Phys. Rev. C **58** (1998) 3266.

[Lob68] K.E.G. Löbner, Phys. Lett. B **26** (1968) 369.

[May49] M.G. Mayer, Phys. Rev. **75** (1949) 1969.

[Mol94] P. Moller and J.R. Nix, J. Phys. G: Nucl. Part. Phys. **20** (1994) 1681.

[Muk05] G. Mukherjee *et al.*, AIP Conf. Proc. **764** (2005) 243.

[Mul71] L.G. Multhauf, K.G. Tirsell, R.J. Morrow and R.A. Meyer, Phys. Rev. C **3** (1971) 1338.

[Nee70] K. Neergård and P. Vogel, Nucl. Phys. A **149** (1970) 217.

[nndc] Evaluated Nuclear Structure Data Files, http://www.nndc.bnl.gov/ensdf.

[Nol90] P.J. Nolan, Nucl. Phys. A **520** (1990) 657c.

[Pag03] R.D. Page, A.N. Andreyev, D.E. Appelbe, P.A. Butler, S.J. Freeman, P.T. Greenlees, R.-D. Herzberg, D.G. Jenkins, G.D. Jones, P. Jones, D.T. Joss, R. Julin, H. Kettunen, M. Leino, P. Rahkila, P.H. Regan, J. Simpson, J. Uusitalo, S.M. Vincent and R. Wadsworth, Nucl. Instr. and Meth. in Phys. Res. B **204** (2003) 634.

[Pag03a] T. Page, PhD thesis, University of Liverpool (2003).

[Pak05] J. Pakarinen, PhD thesis JYFL No.4/2005 (2005).

[Pau95] E.S. Paul, P.J. Woods, T. Davinson, R.D. Page, P.J. Sellin, C.W. Beausang, R.M. Clark, R.A. Cunningham, S.A. Forbes, D.B. Fossan, A. Gizon, J. Gizon, K. Hauschild, I.M. Hibbert, A.N. James, D.R. LaFosse, I. Lazarus, H. Schnare, J. Simpson, R. Wadsworth and M.P. Waring, Phys. Rev. C **51** (1995) 78.

[Pau99] Fortran based cranking code from http://ns.ph.liv.ac.uk/ esp/nuclear/WS/.

[Pau00] E.S. Paul, postgraduate lecture notes, University of Liverpool (2002).

[Rah06] P. Rahkila, to be published and www.phys.jyu.fi/grain.

[Ras59] J.O. Rasmussen, Phys. Rev. **113** (1959) 1593.

[Rei99] P. Reiter, T.L. Khoo, C.J. Lister, D. Seweryniak, I. Ahmad, M. Alcorta, M.P. Carpenter, J.A. Cizewski, C.N. Davids, G. Gervais, J.P. Greene, W.F. Henning, R.V.F. Janssens, T. Lauritsen, S. Siem, A.A. Sonzogni, D. Sullivan, J. Uusitalo, I. Wiedenhöver, N. Amzal, P.A. Butler, A.J. Chewter, K.Y. Ding, N. Fotiades, J.D. Fox, P.T.Greenlees, R.-D. Herzberg, G.D. Jones, W. Korten, M. Leino and K. Vetter, Phys. Rev. Lett. **82** (1999) 509.

[Rei00] P. Reiter, T.L. Khoo, T. Lauritsen, C.J. Lister, D. Seweryniak, A.A. Sonzogni, I. Ahmad, N. Amzal, P. Bhattacharyya, P.A. Butler, M.P. Carpenter, A.J. Chewter, J.A. Cizewski, C.N. Davids, K.Y. Ding, N. Fotiades, J.P. Greene, P.T. Greenlees, A. Heinz, W.F. Henning, R.-D. Herzberg, R.V.F. Janssens, G.D. Jones, F.G. Kondev, W. Korten, M. Leino, S. Siem, J. Uusitalo, K. Vetter and I. Wiedenhöver, Phys. Rev. Lett. **84** (2000) 3542.

[Rei05] P. Reiter, T.L. Khoo, I. Ahmad, A.V. Afanasjev, A. Heinz, T. Lauritsen, C.J. Lister, D. Seweryniak, P. Bhattacharyya, P.A. Butler, M.P. Carpenter, A.J. Chewter, J.A. Cizewski, C.N. Davids, J.P. Greene, P.T. Greenlees, K. Helariutta, R.-D. Herzberg, R.V.F. Janssens, G.D. Jones, R. Julin, H. Kankaanpää, H. Kettunen, F.G. Kondev, P. Kuusiniemi, M. Leino, S. Siem, A.A. Sonzogni, J. Uusitalo and I. Wiedenhöver, Phys. Rev. Lett. **95** (2005) 032501.

[Rin04] P. Ring and P. Schuck, The nuclear many-body problem, Springer-Verlag (2004).

[Rus61] L.I. Rusinov, Sov. Phys. Usp. **4** (1961) 282.

[ship] SHIPTRAP: www.gsi.de/forschung/ap/projects/shiptrap/index_e.html.

[Sim86] R.S. Simon, K.-H. Schmidt, F.P. Hessberger, S. Hlavac, M. Honusek, G. Münzenberg, H.-G. Clerc, U. Gollerthan and W. Schwab, Z. Phys. A **325** (1986) 197.

[Smo95] R. Smolanczuk, J. Skalski and A. Sobiczewski, Phys. Rev. C **52** (1995) 1871.

[Sol91] V.G. Soloviev, , Sov. J. Nucl. Phys. **54** (1991) 748.

[Str67] V.M. Strutinsky, Nucl. Phys. A **95** (1967) 420.

[Uus96] J. Uusitalo, Ph.D thesis, University of Jyväskylä (1996).

[Uus06] J. Uusitalo, private communication.

[Wu92] C.S. Wu, J.Y. Zeng, Z. Xing, X.Q. Chen and J. Meng, Phys. Rev. C **45** (1992) 261.

[Zag01] V.I. Zagrebaev, Y. Aritomo, M.G. Itkis and Yu.Ts. Oganessian, Phys. Rev. C **65** (2002) 014607.